
UNIVERSITÀ DEGLI STUDI DI MILANO BICOCCA

Dipartimento di Fisica G. Occhialini
Corso di Dottorato di Ricerca in Fisica e Astronomia
Ciclo XXVIII

# Characterization of a supersonic plasma source for nanostructured thin films deposition

Ph.D. Thesis of:
**Stefano Caldirola**

Tutor
Prof. **Claudia Riccardi**
Università degli studi di Milano Bicocca
Coordinatore
Prof. **Giuseppe Chirico**
Università degli studi di Milano Bicocca

2014-2015

# CONTENTS

# ABSTRACT

The controlled growth of nanostructured thin films represents a challenging field of research which is related to many different applications of great scientific relevance. The properties of many materials can be greatly enhanced by optimizing the nanoscale assembly processes: by modeling the nanoparticles which create and assemble a film it is possible to achieve very promising results, although it requires a bottom-up approach capable of tailoring the properties with a high level of control or a complex set-up. Plasma-based synthesis processes have been widely developed and applied for an increasing number of technologies leading to important achievements and many industrial-scale applications, in particular in the field of nanoscience. Plasma Assisted Supersonic Jet Deposition offers a novel approach for nanostructured thin films deposition by combining a reactive plasma with a supersonic jet. An argon-oxygen inductively coupled plasma offers a reactive environment where a metalorganic precursor (titanium isopropoxide for $TiO_2$ depositions) is dissociated and oxidized. The gas is then left to expand from a small orifice into a lower pressure vacuum vessel forming a supersonic jet, where the $TiO_2$ nanoparticles are formed and accelerated onto a substrate by the gas carrier mixture. This deposition technique has proven useful for the deposition of nanostructured thin films having a desired morphology at competitive deposition rates. In order to achieve an effective improvement of the synthesis process, an accurate knowledge of the expanding plasma jet chemistry and physics is of fundamental importance. In this PhD project a deep characterization of the supersonic plasma jet was performed using different diagnostics. The plasma discharge in the reactor was monitored by optical emission spectroscopy, Langmuir probes and the measurement of voltage and current values across the antenna of the ICP source. The supersonic plasma jet was characterized using a quadrupole mass spectrometer to sample the gas from the jet at different

positions along its axis of symmetry. The detection of neutral species, radicals, ion fluxes and their energy distribution functions led to an understanding of the expanding plasma properties, its composition and its influence on thin films deposition. In addition to this, based on experimental observations, a MATLAB code was developed to reproduce the ion energy distribution functions numerically from first principle calculations. During this project plasma assisted supersonic jet deposition was also operated for the deposition of nanostructured $TiO_2$ samples whose chemical, physical and morphological properties were analyzed by FTIR, profilometry, AFM, SEM and TEM.

CHAPTER

# 1

# INTRODUCTION

## 1.1 Motivation of this study

Thin-film science and technology play a crucial role in the high-tech industries. While the major exploitation of thin films has been in microelectronics, there are numerous and growing applications in communications, optical electronics, coatings of all kinds, and in energy generation and conservation strategies.
In particular nanotechnology has become one of the most important and growing fields of Physics, Chemistry, Biology and Engineering. Material built from particles smaller than 100 nm exhibit new properties and behavior. This is mainly due to the fact that particles which are smaller than the characteristic length associated to a specific phenomenon show size-dependent properties. Mechanical properties, melting temperature, reactivity, electrical conductivity and optical properties have all been observed to change when the particles building a material become smaller than a certain critical size. This allows us to tailor the properties of a material. In particular thin films having a particular nanostructure were developed and applied for the production of micro-electronic devices, efficient sensor units, optic filters, photocatalysis and photovoltaics applications. It was demonstrated that the film morphology and structure can effectively enhance the efficiency of these devices. The growth of thin and ultra-thin films may be achieved using a large variety of techniques such as chemical vapour deposition (CVD), RF sputtering, pulsed laser deposition (PLD) or plasma enhanced CVD (PECVD). The growth process used determines the structure, so that different techniques can be adopted, depending on which properties are to enhance in the film [1, 2, 3, 4]. Modelling the nanoparticles

which create and assemble the film it is possible to achieve very promising results, although it requires a bottom-up approach capable of tailoring the properties with a high level of control or a complex set-up [5].
While on a small scale there are a large number of production techniques, industrially there is not yet today a flexible and economic process, capable of depositing nanostructured film over large areas. There are however very few examples of processes capable of depositing nanostructured film with controlled chemistry, morphology and porosity. There is no deposition procedure which can easily achieve an accurate control on both the chemical composition and the nanostructure of a thin film and that can be considered truly versatile or up-scalable.
This Ph.D. project aims to study and fully characterize a novel reactor for the production of nanostructured thin films. This reactor was developed to create an efficient and easily controllable process of deposition and growth of nanostructured thin films putting together the strengths of existing, and industrially employed, techniques. The main goal is to gain an accurate control of the nanoscale assembling of the materials produced developing a new deposition techniques named Plasma Assisted Supersonic Jet Deposition (PA-SJD) [6]. The novelty of the proposed approach is the segmentation of the gas phase material synthesis in two separate steps: chemistry control in a reactive cold plasma environment; nucleation and assembling control by means of a supersonic seeded jet over a substrate. High throughput and fast deposition rates could be achieved using high density plasma, which are not feasible, for instance with plasma-laser deposition or conventional sputtering techniques. A cheap, vaporizable and stable monomer could be employed as the source of the oxides, the semiconductors or even the metals. The extraction of a supersonic plasma jet allows to focus the precursor flow on the substrate and to control the growth and the sizes of clusters. By changing the conditions it is possible to obtain hierarchical structures and graded films. The overall structure at the nanoscale is controlled too by the extraction parameters. A supersonic beam allows to obtain clusters of nanoparticles, with a small dispersion of sizes.
The main elements of novelty and innovation of PA-SJD with respect to existing processes are:

- The plasma source, which can be tuned to meet different requirements for the production of the building blocks for the nanostructured deposition. Different reactive environments can be easily created varying the plasma parameters and chemical composition.

- The supersonic seeded jet, which allows an efficient and demonstrated control on the nanoparticles aggregation and on the films growth, controlling their structure and morphology.

- The capability to deposit different kind of oxides, semiconductors and metals.

PA-SJD was employed for the deposition of $TiO_2$, ZnO and Ni nanoparticles, demonstrating a great versatility.

This technique was firstly employed for the production of thin films made of titanium dioxide. $TiO_2$ was chosen because it has been widely used for different applications in a great number of research areas: it is biologically and chemically inert, it combines a high dielectric constant with high refractive index and exhibits a wide-bandgap. These properties make it well suited for microelectronic and semiconductors applications, for sensors, ultraviolet filters and antireflection coating, photocatalysts and photovoltaic [7, 8, 9, 10].
PA-SJD has led to different technological applications, for instance the production of nanostructured $TiO_2$ photoanodes in dye sensitized Graetzel solar cells [11]. Yet many promising applications are still to be explored, such as the deposition of photoanodes for the generation modern solid state DSSC (ultra-thin ZnO or $TiO_2$ films), sensors or optical filters (think nanostructured $TiO_2$ films), metal Ni nanoparticles as powerful catalysts, Si and Ge quantum dots.
To obtain an improvement of the current applications and to develop new interesting ones, it is fundamental to characterize and fully understand this deposition technique, from the generation of nanoparticles inside the plasma, to their assembly in the jet and deposition on the substrate. During this Ph.D. the entire deposition process was deeply characterized and the physics related to the thin films depositions was studied in order to undercover the parameters which can be varied to model the film nanostructure and stoichiometry. This study allowed to gain a insight on the different improvement possibilities, as well as to understand the phenomenology and the physics which are related to the different features of PA-SJD.

## 1.2 Thin films deposition technology

Thin films and nanoparticles made of oxides, semiconductors or metals have many applications in material science. The possibility to change their morphology at the nanoscale makes them even more interesting for applications like catalysis and photocatalysis, energy conversion or storage, rather than more conventional uses as barrier or protective coatings. Despite their wide range of application, few innovative techniques exists for the controlled deposition of nanoscale assembled materials.
Physical vapor deposition (PVD) and chemical vapor deposition (CVD), together with all of their variant and hybrid processes, are the basic film deposition methods [12, 13]. Some factors that distinguish PVD from CVD are:
1. Reliance on solid or molten sources.
2. Physical mechanisms (evaporation or collisional impact) by which source atoms enter the gas phase.
3. Reduced pressure environment through which the gaseous species are transported.

4 . General absence of chemical reactions in the gas phase and at the substrate surface (reactive PVD processes are exceptions).

Evaporation and sputtering are two of the most important methods for depositing thin films by PVD. The objective of these deposition processes is to controllably transfer atoms from a source to a substrate where film formation and growth proceed atomistically. In evaporation, atoms are removed from the source by thermal means, whereas in sputtering they are dislodged from solid target (source) surfaces through impact of gaseous ions.

Chemical vapor deposition (CVD) is the process of chemically reacting a volatile compound of a material to be deposited, with other gases, to produce a nonvolatile solid that deposits atomistically on a suitably placed substrate. High-temperature CVD processes for producing thin films and coatings have found increasing applications in such diverse technologies as the fabrication of solid-state electronic devices, the manufacture of ball bearings and cutting tools, and the production of rocket engine and nuclear reactor components. Among the reasons for the growing adoption of CVD methods is the ability to produce a large variety of films and coatings of metals, semiconductors, and compounds in either a crystalline or vitreous form, possessing high purity and desirable properties. Furthermore, the capability of controllably creating films of widely varying stoichiometry makes CVD unique among deposition techniques. Other advantages include relatively low cost of the equipment and operating expenses, suitability for both batch and semicontinuous operation, and compatibility with other processing steps. Hence, many variants of CVD processing have been researched and developed in recent years, including low-pressure (LPCVD), plasma-enhanced (PECVD), and laser-enhanced (LECVD) chemical vapor deposition.

Titanium oxide and zinc oxide are usually synthesized by sol–gel synthesis of nanoparticles followed by sintering has been employed, generally yielding disordered films either with moderate porosity [14, 15], or in the form of an aerogel [16]. Ordered structures, with an engineered pore architecture, have been obtained by using templating agents. Besides the complexity of these approaches, the necessary removal of the templating agent may cause severe dimensional changes and surface area reduction [17]. Recently, there have been reports on the template-free fabrication and photocatalytic activity of hierarchically organized nanostructured $TiO_2$ [18, 19, 20]. Although the employed techniques are very powerful in producing powders composed of highly engineered particles, characterized by a complex nanostructure, no reports have been issued on the growth of hierarchical $TiO_2$ thin films on surfaces for the functionalization of large scale areas.

Typical thin film deposition techniques, such as CVD, sputtering and pulsed laser deposition (PLD), have also been tried with some excellent results in the doping issue but limited success in regards to surface area, since they tend to form essen-

tially 2D films with limited surface area [21, 22]. A few authors obtained columnar or sculptured thin films by sputtering [23] or flame aerosol synthesis, with porosity determined by column diameter and spacing. In particular, Suzuki and Yang obtained high surface area $TiO_2$ and ZnO films, showing enhanced activity, by typical thin film techniques such as glancing angle deposition (GLAD) and MOCVD, respectively [24, 25]. Suzuki demonstrated an enhanced surface reaction efficiency of obliquely deposited $TiO_2$ thin films with variously shaped columns (e.g. zigzag, cylinder, and helix). He clearly showed that columnar thickness and spacing play an important role in the enhancement of the effective surface area. Notable examples of 3D film structure were demonstrated by Goossens et al, who obtained a fractal 'forest like' titanium oxide deposit by CVD [26]. In general, the active surface area of these films is limited to the sum of the exposed areas of individual columns or needles. Furthermore, inter-columnar spacing is hardly controllable to a large extent. Other techniques like SCBD [27, 28] achieved interesting results in the deposition of nanostructured materials, even though with uncertain up-scalability. A novel one-step, template-free production, by reactive PLD, was also suggested for producing hierarchically organized nanostructured $TiO_2$ [29] and tungsten oxide [30]. Even though PLD is a versatile technique for the production of nanostructured-materials, still has limited chances in large area applications like those in energy and environment. Furthermore, high power – high repetition rate lasers ($> 200$ Hz) are extremely expensive. Both these issues preclude to PLD inexpensive mass fabrication of thin films. For the deposition of Si and Ge quantum dots the most innovative technique is the one disclosed by U. Korthagen and coworkers [31]. In this novel fabrication process a silane gas is injected in a flowing Ar plasma and crystalline silicon form in the gas phase. No examples of nano-assembled functional films have been demonstrated so far.

## 1.3 Plasma assisted supersonic-jet deposition

PA-SJD was developed for the purpose of going beyond current limitations of nanoscale fabrication techniques segmenting the gas phase material synthesis in two separate steps: chemistry control in a reactive cold plasma environment; nucleation and assembling control by means of a supersonic inseminated jet impacting over a substrate. Thanks to this two steps-continuous process it is anticipated an overall enhanced control and versatility of the deposition technique, like in PLD, but over large area and with high deposition rates, like in PECVD and flame synthesis. Over conventional gas phase processes the proposed technique allows control of the kinetic energy of clusters, whence control on their assembly pattern on the substrate.
High throughput and fast deposition rates could be achieved using high density plasma. Volatile and stable monomers could be employed as precursors for producing oxides, semiconductors or metals. Dividing the deposition process in two

different steps (the plasma and the supersonic jet) represents a strategy to achieve a better control on the deposition process, acting separately on different features and parameters of the deposition device. PA-SJD offer the advantages of plasma based deposition processes, which can be summarized in low energy cost, low temperature employed and the presence of a very reactive environment. Low-temperature plasma have been applied to materials synthesis, structuring and processing for decades. However, learning how to use such plasma to allow these processes to occur at nanoscale dimension has only become critical since the rapid growth of nanoscience and nanotechnology in last two decades, and it is still an important issue. The use of a supersonic jet expansion allows the formation of a oriented jet capable of accelerating the nanoparticles to a common velocity. Although this technology has been widely used for the production of molecular beams in many experiments and applications, few about it is known in the presence of a plasma or in the low density regime in which PA-SJD operates.

The deposition system includes a vacuum chamber, referred as plasma chamber, separated through a converging nozzle from a different vacuum chamber, the deposition chamber. A pressure difference is established among the two chambers, in order to create the conditions for the supersonic expanding jet formation. In the first chamber a plasma is created through an inductively coupled argon-oxygen plasma source and a gaseous precursor of the substance to be deposited is injected. The dissociated precursor then flows in the deposition chamber with the expanding jet: the light gas carrier mixture accelerates different nanoparticles up to 0.1-0.5 eV. As the gas expands, pressure, temperature and density decrease creating an energetic and low-collisional flow. In this way it is possible to control the production of the $TiO_x$ seeds and their acceleration and assembly on a substrate. In particular, when deposition of molecular clusters is performed under condition of supersonic jet, several advantages can be envisaged including the better collimation, stability and the control on crystalline structure.

In this Ph.D. thesis a great part of the experimental work is based on the characterization of the plasma parameters and of the supersonic jet by using different diagnostics.

## 1.4 Experimental characterization of the supersonic plasma jet

A movable quadrupole mass spectrometer (QMS) was used to sample the expanding plasma at different position along the axis of symmetry of the expanding jet. The sampling orifice of the instrument is placed in the middle of a 50 mm diameter flat hat on the movable cylinder. In this way it was possible to obtain a measurement of the gas parameters in experimental conditions highly comparable to those involved

in thin film deposition. In the experimental chapters the QMS was widely used to characterize the supersonic jet in the absence of plasma (Chapter 3), investigating the gas expansion theory for argon, oxygen and argon-oxygen mixture, in the presence of an argon-oxygen plasma (Chapter 4) and then injecting the metalorganic precursor (Chapter 6). Quadrupole mass spectrometry allowed us to obtain quantitative measurements of the gas density (observing also $TiO_x$ seeds with masses up to 320 amu), radical species and ion fluxes at different energies. These results were used to describe and characterize a theoretical model for the gas expansion also in the presence of nanoparticles. These measurements were acquired simultaneously to other analysis of the plasma into the first chamber by optical emission spectroscopy, Langmuir probe and electrical measurements. The radiation emitted from excited molecules and atoms in the plasma was detected directly observing the plasma in the first chamber through a quart window with different optical fibers. The emitted lights was mainly used to identify the different species inside the plasma. In the presence of the metalorganic precursor oxidation reactions were observed and the precursor flux could be monitored and controlled. Additionally studying the different peak ratio of the argon-oxygen plasma the electronic temperature was estimated. Langmuir probes were inserted in the plasma chamber and allowed a direct measurement of the current-voltage characteristic which was used to determine the plasma density and temperature in the border regions of the plasma chamber. The RF current and voltage across the inductive antenna were observed using a high resolution oscilloscope. These values were used to evaluate the power transmission to the plasma and the effective coupling between the antenna and the plasma.
A particular analysis of the ion energy distribution functions was then conducted in an argon plasma. Generally we found two-peak ion energy distributions, which stressed the presence of interesting collisional phenomena. To understand the dynamics of ions and its effect on the thin film deposition we developed a simulation model (described in Chapter 5). Starting from the experimental data of the ion energy along the jet, a Matlab code, based on first principle calculation, was developed to simulate the dynamics of different ions moving in the jet. The entire trajectories of ions along the supersonic jet were simulated, modeling the interaction with neutrals with a 12-4 Lennard Jones potential. Integrating the equation of motion at very short time steps (of the order of tens ps) it was possible to obtain exact results of the energy distribution of the ions which were detected from the mass spectrometer. The energy distribution functions simulated were compared with the experimental data and the frequency and the effects of $Ar^+$-Ar collisions were examined. From this analysis the energy transferred from the ions to the neutral species was evaluated, alongside the ion mean free path and cross section in a supersonic jet. This study also helped defining the plasma potential distribution along the expanding jet.

## 1.5 Thin films growth by PA-SJD

Another experimental part of this thesis was dedicated to the deposition of $TiO_2$ thin films and to their characterization (Chapter 7). Thin films were deposited at different positions along the jet and different precursor injection rates, on two different kind of substrates (flat silicon and a FTO-glass with a blocking layer). By contact profilometry the deposition rate and the shape of the films were characterized and related to the supersonic jet theory. The stoichiometry and crystalline structure of the films were studied by FTIR analysis and Raman spectroscopy. Also the morphological structure and the surface properties of the films were studied by SEM imaging and atomic force microscopy, revealing the nanostructure of the thin films and its relation to the experimental conditions The results of these analyses are used also to define how different deposition parameters can influence the morphology and structure of the nanostructured thin films obtained by PA-SJD and were used to set a model for simulating the film growth process.

CHAPTER

# 2

# PA-SJD: TECHNICAL DETAILS AND DIAGNOSTICS

## 2.1 PA-SJD device

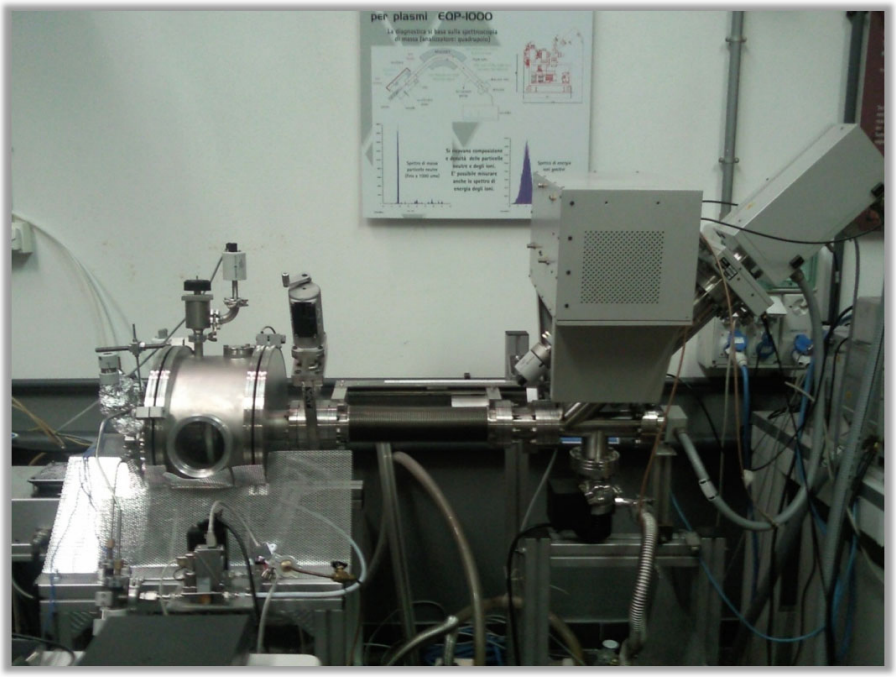


Figure 2.1: Photography of the PA-SJD device shot in the laboratory. The quadrupole mass spectrometer Hiden-EQP 1000 used for the measurements is located on the right and can be moved inside of the vacuum chamber on the left.

### 2.1.1 The vacuum vessel

The main vacuum vessel is a stainless-steel cylinder (200 mm height, 160 mm inner radius) divided in two chambers: the plasma chamber and the deposition chamber, which are connected through a converging nozzle as illustrated in Fig. 3.1. The left lid of the main vessel is in direct contact with the plasma chamber, which is cylindrical (95 mm height, 62.5 mm inner radius).

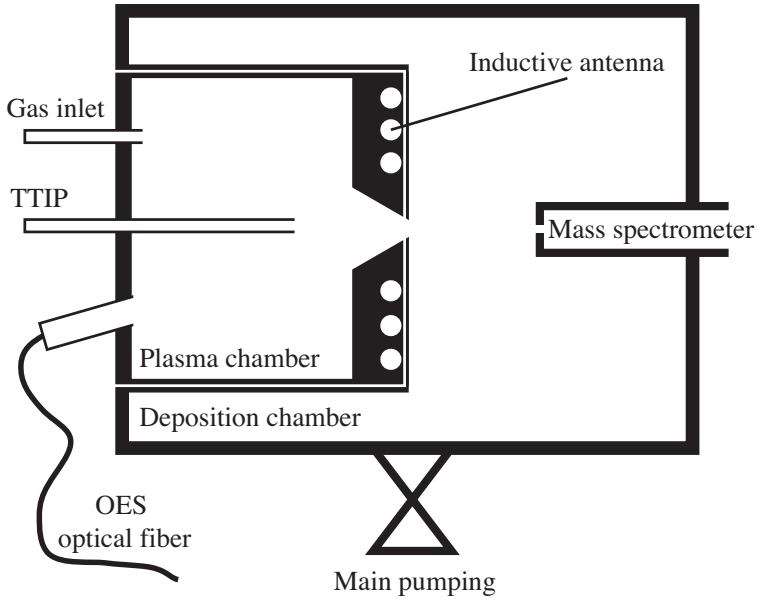


Figure 2.2: Schematic view of the experimental setup. The mass spectrometer sampling orifice can be moved horizontally inside the deposition chamber.

On the bottom of the deposition chamber a circular conductance (100 mm diameter size, variable by closing a gate valve) connects our vacuum vessel to the pumping system, which is made of a turbo molecular pump and a rotary pump. The position of main pumping system was chosen to ensure lowest perturbation on the fluid dynamics of the jet. The effective pumping speed is about 130 l/s at the experimental conditions used in this work (8 Pa in the plasma chamber, 0.03 Pa inside the deposition chamber) and, when no gas is injected, the limit pressure inside the deposition chamber is close to $10^{-5}$ Pa. On the right side of the deposition chamber there is another vacuum flange which allows the insertion and the movement of a quadrupole mass spectrometer. The QMS can collect the gas (and ions) from a small conductance (a 0.1 mm diameter circular orifice) and it is maintained below $10^{-4}$ Pa by another pumping system (a turbo molecular pump and a rotary pump providing 60 l/s pumping speed).
Argon and oxygen are injected directly into the first chamber using two separate mass-flow controllers. The gas mixture inside the plasma chamber can be considered well-mixed since the diffusion speed (calculated at the experimental condition commonly used in this thesis) exceeds the flow velocity (respectively 1.26 and 0.04

m/s) [32, 33, 34]. The converging nozzle has the shape of a rounded rectangle (ending with an aperture 22×30 mm) closed by a 1 mm thick thin foil having a centered circular orifice (6.9 mm of diameter). A converging nozzle favors the formation of the supersonic jet by accelerating the gas particles to a sonic speed and has the practical advantage of allowing the use of different kind of orifices or slits, which can be easily replaced changing the thin foil. Rectangular slits were previously used for depositions [6], however we chose a circular orifice for this characterization to obtain an axis-symmetric jet. During the measurements the pressure in the chambers is monitored using two capacitance pressure gauges. Their pressure reading precision is quite good in the pressure ranges where we operate, which are between 8-10 Pa in the plasma chamber, and 0.01-8 Pa in the deposition chamber. To monitor the pressure over a wider range of pressures (from $10^{-6}$ Pa to atmospheric pressure) two full range gauges (which couple a pirani and a cold cathode system) are also present inside the deposition chamber and the mass spectrometer. The pressures inside the plasma and the deposition chambers are named respectively $P_0$ and $P_d$, the latter is controlled by the gas flow rate and the conductances of the orifice at the end of the nozzle and the gate valve over the main pumping group. $P_0$ can be easily accurately varied changing the flow rate of the gas. The small conductance associated with the circular orifice connecting the two chambers (about 4.8 l/s, measured experimentally at the working pressure values and slightly dependent from the pressure) allows us to change the pressure inside the deposition chamber $P_d$ (with negligible variations to $P_0$) by partially closing the gate valve which connects the main pumping group, thus reducing the effective pumping speed. The pressure ratio between the two chambers is defined as: $R = P_0/P_d$ and it can be varied from 40 to 1 to model the supersonic jet geometry and energy.

### 2.1.2 The plasma source

An inductively coupled plasma (ICP) source can provide high and uniform plasma charge densities and low, controllable ion energies [35, 36, 37]. This kind of plasma source also ensures low contamination by sputtered products from the reactor walls, because the electrodes are not in direct contact with the plasma. A reactive plasma is generated inside the plasma chamber by a 13.56 MHz radiofrequency power generator (Huttinger PFG 1600 RF). The generator is connected through a tunable matching box (L-type) to a two and three quarters loop planar antenna made of copper wire located on the right side of the plasma chamber (see Fig. 3.1), inside a teflon scaffold covered by an alumina disc to reduce teflon sputtering. The entire vacuum vessel, both the plasma and the deposition chamber, is grounded. By feeding the antenna with 450 W RF power at 8 Pa a stable inductive plasma discharge can be sustained with moderate heating (deionized water is circulated inside the copper wire, to keep the antenna cooled). Previous experiments reported electron

temperatures of about 1 eV [6, 38].

### 2.1.3 TTIP precursor

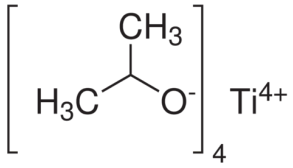


Figure 2.3: Chemical formula of the Titanium Isopropoxide, the metalorganic precursor used for $TiO_2$ depositions.

A metalorganic precursor can be injected inside the first chamber when the plasma discharge is sustained at a sufficiently high power level. $TiO_2$ films can be obtained from different organic precursors, titanium alkoxide are preferable such as $Ti(OPr^i)_4$, which already display the $TiO_4$ tetrahedral motif of titanium dioxide lattice in their chemical structure [39]. In this work we chose titanium (IV) Tetraisopropoxide $Ti(OCH(CH_3)_2)_4$ or TTIP (see Fig. 2.3), which is liquid at 20°C and it is heated with a power transformer to reach the vapour phase. The temperature can be monitored with a thermocouple over the precursor tank and varied to obtain different precursor flows (from 0.25 to 0.75 grams per hour). Operating at temperatures between 40 and 47°C the vapour pressure of TTIP is sufficiently high to create a stable flow inside the plasma chamber.

## 2.2 Hiden Analytical Quadrupole Mass Spectrometer

### 2.2.1 Hiden EQP-1000 Analyzer

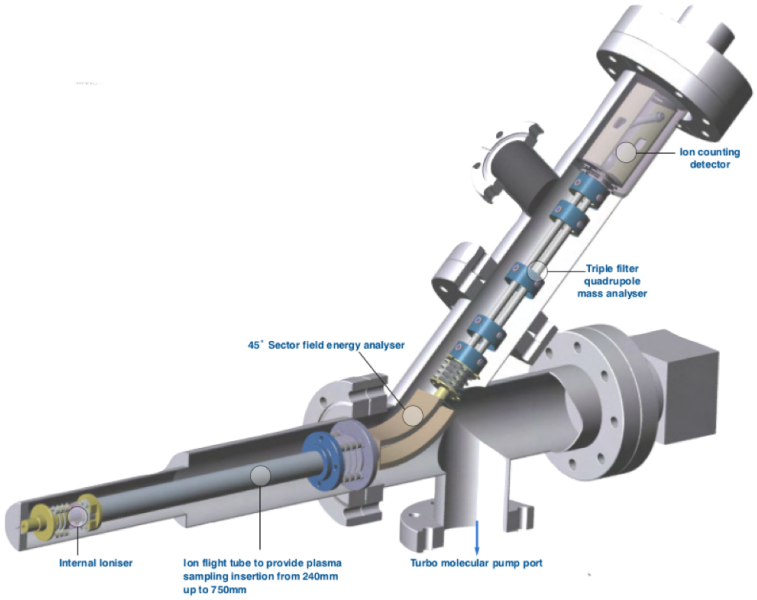


Figure 2.4: Design and structure of the Hiden EQP-1000 Analyzer.

We employed a QMS (Hiden EQP-1000 Analyzer [40, 41, 42, 43]), movable across a vacuum flange, to acquire spectra along the axis of symmetry of the main vacuum vessel (300 mm scan from outside the right lid to the nozzle connecting the two chambers). Measurements were performed at different positions of the z axis with the accuracy of 1 mm. The gas sampling orifice is located in the center of a flat circular cap (25 mm radius). We are interested in the analysis of the deposition conditions on a flat substrate having dimensions comparable with our spectrometer, so any perturbation introduced by the QMS sampling is somewhat analogous to what happens during thin film growth. The EQP-1000 Analyzer is a quadrupole mass spectrometer equipped with a high-transmission 45° sector field ion energy analyzer. Mass spectra from 0.4 up to 1000 amu/q can be acquired both for neutral and ion species with a resolution of 0.02 amu. Trends for a short list of relevant masses (up to 100) may also be measured and plotted against time (with a time resolution of 100 ms for each mass) providing a truly real time and quick diagnostic tool. Ion energy spectra may be acquired for a fixed mass from -150 to +150 eV at high resolution (0.05 eV). The gas ionization is obtained by electron-impact: an oxide coated iridium filament emits thermal electrons which are accelerated toward a grid at a determined energy. In the ion source we used an electron current of 10 $\mu$A and 70 eV electron energy which is common and corresponds to a high value for the first-ionization cross section for both argon and molecular oxygen. Moreover at this electron energy there is a small production of double charged ions and fragments

(under few percent values). Successively a focusing system drives the ions into the quadrupole mass filter, where the RF-voltage applied to the quadrupole unit allows only ions of a certain mass-to-charge ratio to reach the detector. The detector is a secondary electron multiplier pulse-counting detector which can provide mass spectra in counts per second from 1 up to $10^7$ counts/s. Since the particles detection is very dependent from the ion trajectories, the instrument requires an internal low pressure (less than $10^{-4}$ Pa) to ensure almost no collisions inside.

### 2.2.2 Quadrupole Mass spectrometry of reactive plasma

Quadruple mass spectrometers represent an in situ, real time sensing diagnostic used to perform residual gas analysis of gas and reactive plasmas [44]. The measured signal for each neutral gas species is directly proportional to the sampled gas density, the electron impact ionization cross section and the instrument mass dependent transmission function for secondary ions. An absolute density value of a neutral particle can be obtained if the instrument transmission function for that specific mass is known. Since the measured signal is linearly dependent from the gas density, the latter can be also calculated using a simple conversion factor obtained from a calibration performed in a region where the density of gas species is well known. The spectrometer can sample also positive and negative ions detecting their flux at different masses (at a fixed energy) or energies (for a fixed mass). In both cases no electron impact ionization is needed. Contrary to the detection of neutral species, the QMS signal detected for the ions is proportional to their flux and to the instrument mass and energy dependent transmission function. This makes the acquired signal for charged species to be highly dependent also on their energy. The focusing system has first to be tuned in order to collect ions from the sampling orifice and to deliver them to the quadrupole. In addition to that, it is possible to reduce the energy dependence of the measured signal, by using a proper setting for the ion focusing lenses. Aberrations known for optical lenses also apply for the electrostatic lenses of the focusing system. Due to chromatic aberration the focal length of an electrostatic lens can vary at different ion energies [45]. In order to ensure a proper tuning of the ion focusing and the reduction of chromatic aberrations, the voltage settings for the electrostatic lenses were obtained, with particular care, from tuning procedures recommended by the manufacturer. It has to be taken into account also the ion acceptance angle [46] which is a function of the ion energy and it depends on the electric field just inside the orifice and hence on the settings of the first electrostatic lens. The simulations of ion trajectories into similar mass spectrometers [46, 45] have shown that the larger the extractor voltage in the first lens, the larger the acceptance angle. In this work we have used a very small value for the extractor voltage (-2 V) to reduce the acceptance angle. The sampling orifice is drilled on a grounded cap at the same reference potential of the vacuum vessel. Thus ion coming from

plasma region at positive potential will be accelerated from the potential difference before being collected. For the measurement of mass scan for ion fluxes we have used an energy filter, which was set to transmit ion at 8 eV. This was optimal to perform ion mass scan under our plasma conditions as most of the masses were found at this energy. The measurement of the ion distribution functions for each single mass was performed having the quadrupole mass filter on the weighted average mass determined by the mass spectra.

## 2.3 Optical Emission Spectroscopy

### 2.3.1 Optical spectrometers

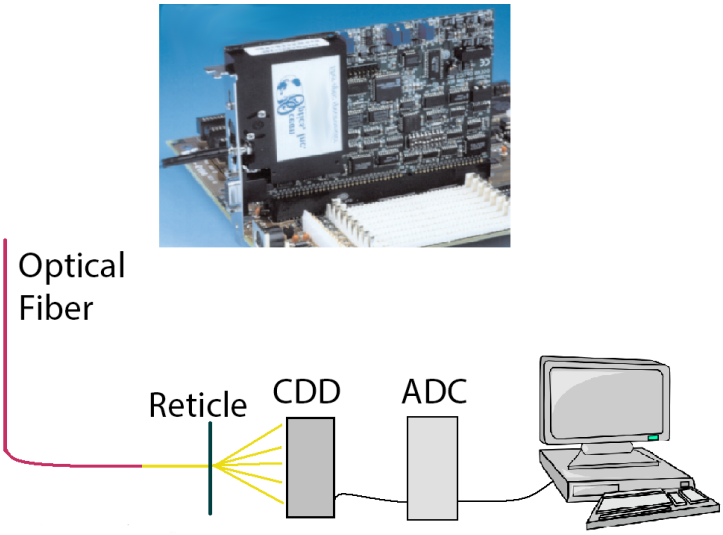


Figure 2.5: Detecting plasma radiation with a optical spectrometer: radiation is transmitted through a optical fiber to a diffraction reticle. The incoming photons are then detected by a CCD (charged coupled device) and converted into a signal by a ADC (analog to digital converter) which is measured by a computer.

Optical emission spectroscopy (OES) is a well know non-intrusive diagnostics which can be easily applied in almost every kind of plasma discharge [47, 48]. Revealing the light emitted from atoms, molecules and ions which are excited from free electrons in the discharge, it is possible to understand the main reaction processes in the plasma. The intensity of emission lines can identify chemical species and allow to gain insight about their abundances. From the quartz window (16° to the perpendicular of the left lid) facing the plasma chamber optical emission spectra (OES) were acquired using two different low resolution spectrometers, as already described in our previous works [6, 48]. The first is a wide band, low resolution spectrometer (AvaSpec-2048 by Avantes) equipped with a 10 $\mu$m slit, a holographic grating (300 lines/mm, blazed at 300 nm), a coated quartz lens to increase sensitivity in UV and a 2048 pixels CCD. The spectrometer has a resolution of about 0.8 nm and a spectral band extending

from 180 nm to 1150 nm and was used in connection with a IR enhanced optical fibre. The second instrument used is a lower resolution spectrometer (PS2000, Ocean Optics) which was acquiring spectra through a UV enhanced optical fiber. This device was equipped with a 10 $\mu$m slit and a holographic grating (600 lines/mm, blazed at 400 nm) having a resolution of 1.02 nm and a spectral band extending from 200 to 850 nm.

### 2.3.2 OES data analysis and interpretation

Exited atoms and molecules from a plasma commonly emit a bright radiation. Emission lines near the visible part of the spectrum (100-1000 nm) can be easily detected using an optical fiber connected to a spectrometer. Narrow lines are related to electronic transitions (de-excitation) between levels of the atomic system and can be used, at first, to identify different species inside the plasma discharge. The analysis of the line emission area can be directly related to the number of photons at the energy corresponding to the considered wavelength (after the spectra has been dark substracted and corrected by the fiber-instrument transmission function).
This number can be used to estimate the density of a particular radical inside the plasma discharge by actinometry. The intensity of an emission line, measured in counts per second, is proportional to the number of atoms undergoing that particular de-excitation process. In a simple collisional-radiative model (which describes fairy well low temperature plasma) the excitation of an atom or molecule is due to electron-impact excitation, thus depending on the electron density and temperature. Considering the populations of excited atoms and molecules in the plasma as a system in a stationary state, the intensity of a particular line is proportional to the number density of that species inside the plasma, the electron density and a excitation-rate term which is a function of the electron temperature. If an inert gas is present inside the plasma with a known density (such as argon in our case), this can be used to evaluate the trend of species density inside that plasma discharge, by evaluating their ratio.
Optical emission spectroscopy can also be employed for a more detailed analysis of the plasma. It is possible to evaluate the electron temperature and the density of ground state and metastable species (excited neutrals maintaining their energy for times longer than other states, of the order of milliseconds). This calculation requires the study of the whole spectrum of a particular species: if the excitation rates (as a function of electronic temperature) and de-excitation rates (which are constants determined by the Einstein coefficients) are known and a sufficiently high number of lines can be measured, it is possible to set a linear system where the unknown quantities are electron temperature and the ground state or metastable states density. A numerical solution of this system can give the most probable electron temperature.

## 2.4 Electric diagnostics

### 2.4.1 Current-Voltage characteristics

During each plasma discharge, the electrical parameters were observed measuring times series of voltage and current at the two different side of the planar antenna. The voltage directly exiting the matching box was measured using a high-voltage probe (Tektronix P6015A), while the current flowing in the antenna was acquired with a Rogowski probe positioned at the grounded side of the coil. Both signals were simultaneously acquired using a digital oscilloscope at 4 GHz sampling frequency to obtain a detailed electrical characterization.

Figure 2.6: HIgh voltage Tektronix P6015A probe, used to measure the voltage across the coil.

Figure 2.7: Rogowski coil located on the grounded side of the antenna directly measuring the current flowing inside the wire.

The rms values for voltage and current were obtained from the time series, with also their phase shift. Knowing these quantities it is also possible to determine the load resistance and reactance, which define whether the discharge is operating in a capacitive or inductive regime.

### 2.4.2 Langmiur probes

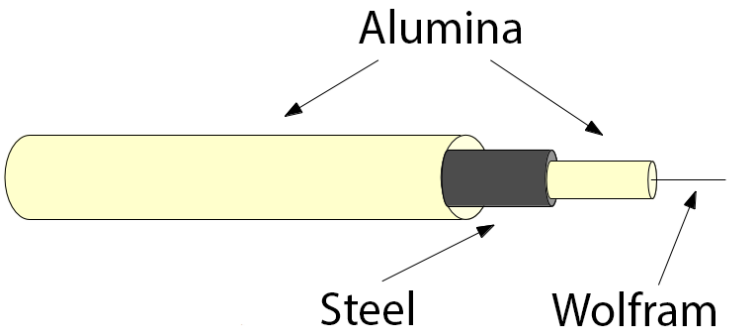


Figure 2.8: A Langmuir probe basically consists in a conductive wire (Wolfram commonly, due to the high thermal resistance), shielded by dielectrics (for example alumina) and steel (to reduce signal interferences). Only the final tip of the wire is left exposed to the plasma, which should be normally longer than the larmor radius of the charged particles inside the plasma. Acquiring the signal measured by the wire with an oscilloscope it is possible to measured many plasma parameters.

A Langmuir probe was used to measure plasma parameters inside the plasma chamber alternatively to OES measurements. The probe was moved inside the plasma chamber from the quartz window facing the plasma chamber, also used for optical spectroscopy measurements. For the theories and techniques concerning the most common solutions used for parameter investigation in simple magnetized plasma there is a wide literature available. However when operating in RF plasma, the analysis of the Langmuir current-voltage characteristic curve can be very different due to the plasma potential fluctuations. An example of the effect of an oscillating RF field on the characteristic curve can observed in Fig. 2.9, where the black line represent the real electric current (total current subtracted ion current) at different voltages ($V_p$ being the voltage applied to the probe, $V_s$ the voltage of the plasma region) and the green the averaged effects of an oscillating field.

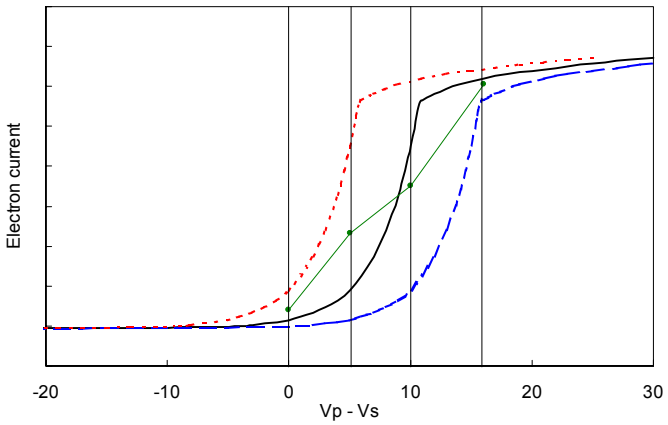


Figure 2.9: The center curve is the real $I-V$ curve. The dashed ones are displaced by $\pm 5$ V, representing changes in $V_s$. At the vertical lines, the average $I_e$ between the displaced curves is shown by the dot. The line through the dots is the time-averaged $I-V$ curve that would be observed, differing greatly from the correct curve.

Several methods for reducing radiofrequency perturbation effects can be adopted [49, 50, 51, 52, 53]. In order to obtain the real current-voltage characteristic in a high RF environment, we used a Langmuir probe with a compensating circuit. The probe has an exposed tungsten tip, 5 mm length and 1 mm diameter. The probe tip connection is insulated and shielded in a probe holder, 15 cm long, made of two coaxial alumina tubes. RF compensation was achieved using the method proposed long ago by Godyak et al. [54] and Chen [55]. A miniature RF choke (made of a ferrite core, Q $\simeq$ 200 with a impedence of about 85 k$\Omega$) was embedded near the probe tip. A floating electrode (a copper foil, 10 mm wide, 3 mm diameter, glued on the probe alumina tube 3 mm before the tip) exposed to the plasma was coupled through a large capacitor to the probe tip (100 pF) to ensure an almost constant impedance load during the probe voltage scan to record the Langmuir characteristics [55].

Probe was calibrated at workbench by fine tuning the choke capacitance and thus the frequency to match the 13.56 MHz RF supply. The probe was already employed in other plasma discharges and checked against traditional Langmuir probes [48]. In general a fixed voltage ramp was applied in a 100 ms time scan [56] and the probe current was measured with an equivalent resistance of 100 $\Omega$ by an Agilent scope with a 100 kHz sampling rate. The Langmuir characteristics was obtained by averaging about 20 voltage ramps. Analysis of the curve was performed using a dedicated software, in order to extract the plasma density and potential, as well as the electron temperature [56].

Unfortunately radiofrequency disturbance from the plasma was very strong at high power input, thus the analysis of the whole probe parameters for the H-mode discharge region (RF power input above 200 W) was greatly affected for the electron capture region. However during H-mode discharge it was possible to evaluate the

charge density following the methods suggested by Chen [50, 51].

## 2.5 Thin film analysis diagnostics

### 2.5.1 Profilometry

In profilometer analysis, a diamond stylus is moved vertically in contact with a sample and then moved laterally across the sample for a specified distance and specified contact force. A profilometer can measure small surface variations in vertical stylus displacement as a function of position. A typical profilometer can measure small vertical variations ranging in height from 10 nanometres to 1 millimeter. The height position of the diamond stylus generates an analog signal which is measured and stored. The radius of diamond stylus ranges from 20 nanometres to 50 micrometers, and the horizontal resolution is controlled by the scan speed and data signal sampling rate. The stylus tracking force can range from less than 1 to 50 milligrams. For thickness analyses of thin films deposited by PA-SJD we used a Dektak 8 Stylus Profilometer from Veeco. Applied stylus tracking force was 15 mg, its vertical resolution was 1 Å.

### 2.5.2 FT-IR Spectrometer

Infrared spectroscopy is a widely used technique which represents an important tool for investigating chemical processes and structure. Fourier transform infrared - attenuated total reflectance (FTIR-ATR) spectroscopy uses a property of total internal reflection resulting in an evanescent wave.

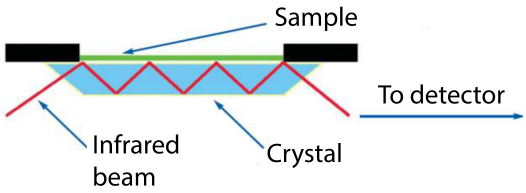


Figure 2.10: Schematics of the infrared laser reflecting inside the crystal during a FT-IR ATR measurement.

Surface chemical composition of the samples was investigated by means of a Fourier Transform Infrared (FT-IR) spectrometer (Nicolet iS10, Thermo Scientific) equipped with a ATR sampling accessory (Smart iTR). For each spectrum 64 scans, with a spectral resolution of 2 $cm^{-1}$ were recorded. A basic IR spectrum is essentially a graph of infrared light absorbance or transmittance versus the wavenumber. The infrared spectrum of a sample is recorded by passing a beam of infrared light through the sample. When the frequency of the IR is the same as the vibrational frequency of a bond, absorption occurs. Examination of the transmitted light reveals how

much energy is absorbed at each frequency. Infrared light is guided through an interferometer and then through the sample (or vice versa). A moving mirror inside the apparatus alters the distribution of infrared light that passes through the interferometer (see Fig. 2.10). The signal directly recorded, called an interferogram, represents light output as a function of mirror position. A data-processing technique called Fourier transform turns this raw data into the sample spectrum. ATR uses a property of total internal reflection resulting in an evanescent wave. A beam of infrared light is passed through the ATR crystal in such a way that it reflects at least once off the internal surface in contact with the sample. This reflection forms the evanescent wave which extends into the sample. The penetration depth into the sample is typically between 0.5 and 2 $\mu$m, with the exact value being determined by the wavelength of light, the angle of incidence and the indices of refraction for the ATR crystal and the medium being probed. The number of reflections may be varied by varying the angle of incidence. The beam is then collected by a detector as it exits the crystal. The signal-to-noise ratio obtained depends on the number of reflections but also on the total length of the optical light path which dampens the intensity. Therefore, a general claim that more reflections give better sensitivity cannot be made.

### 2.5.3 Atomic force microscopy

AFM measurements are carried out using a Solver P47-PRO (NT-MDT), in semi-contact (tapping) mode on dry samples using HA-NC (High Accuracy Non Contact) silicon tips (NT-MDT) of typical spring constant 3.5 N/m. The AFM consists of a cantilever with a sharp tip at its end that is used to scan the specimen surface. The cantilever is typically silicon or silicon nitride with a tip radius of curvature on the order of nanometers. When the tip is brought into proximity of a sample surface, forces between the tip and the sample lead to a deflection of the cantilever according to Hooke's law. Typically, the deflection is measured using a laser spot reflected from the top surface of the cantilever into an array of photodiodes. If the tip is scanned at a constant height, a risk would exist that the tip collides with the surface, causing damage. Hence, in most cases a feedback mechanism is employed to adjust the tip-to-sample distance to maintain a constant force between the tip and the sample. Traditionally the tip or sample is mounted on a piezoelectric tube, responsible for scanning in the x,y and z directions. A topographic image of the sample is obtained by plotting the deflection of the cantilever versus its position on the sample. Image contrast arises because the force between the tip and sample is a function of both tip–sample separation and the material properties of tip and sample. Image contrast is obtained from the very short range repulsion, which occurs when the electron orbitals of tip and sample overlap. However, further interactions between tip and sample can be used to investigate properties of the sample, the tip,

or the medium in between.
Despite the ability to reach high spatial resolution, the acquired surface topography image can sometimes not correspond to the real surface features due to the effect of the instrument tip dimension on the object resulting in the artifacts appearance. These artifacts, as a rule, can be easily taken into consideration while qualitatively interpreting the AFM results; however, some special problems can require quantitative estimation and reconstruction of sample true geometry. During scanning, two major AFM artifacts can appear: a profile broadening effect due to the tip-sample convolution and a height lowering effect due to the elastic deformation of studied objects. If the tip radius R is much less than the feature curvature radius r, the object lateral width $r_c$ is:

$$r_c = r(cos\theta + sqrtcos^2\theta + (1 + sin\theta)(-1 + tan\theta/cos\theta) + tan^2\theta)$$

where $\theta$ is the cone half angle shown in Fig.2.11. The corresponding surface profile in the contact mode under given conditions is shown in Fig.2.11 a). In this case, the object is broadened by $2(r_c$ - r), while its height remained equal to 2r.

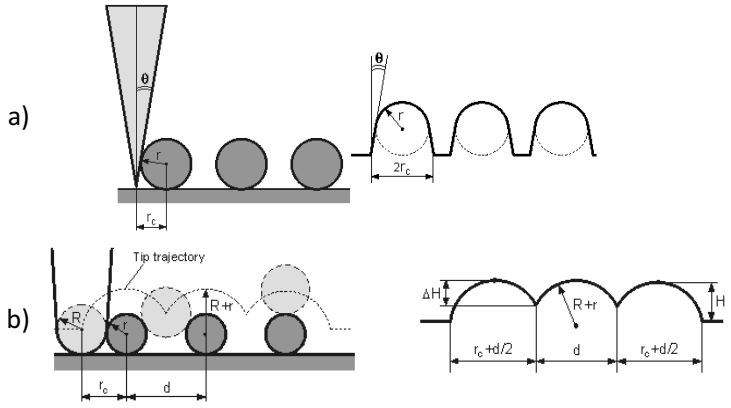


Figure 2.11: Different interpretation of AFM measurements: a) when the tip radius R is much less than the curvature radius r, b) when the tip radius R is comparable with the curvature radius r.

If the tip radius is approximately equal to the feature curvature radius, the tip moving across the object surface can be approximated by the sphere of radius R moving along the sphere of radius r surface, thus describing an arc of radius R + r. In this case for the object lateral dimension $r_c$ (Fig.2.11 b) ) we have:

$$r_c = 2\sqrt{Rr}$$

Since the probe tip has a circular shape with a 10 nm radius $R$, this equation is the most suited for estimating the dimension of the grain for our nanostructured depositions. From the two dimensional imaging of the film surface it is possible to calculate, besides the typical grain dimension, the surface roughness with great

accuracy. In particular the root mean square of the height distribution function is commonly used as a parameter describing thin film roughness.

CHAPTER

# 3

# THE SUPERSONIC JET

## 3.1 Introduction

The free expansion of a gas exiting from a sonic nozzle into a partially evacuated vacuum chamber is a process which leads to the formation of a supersonic jet with a very narrow velocity distribution [57]. The under-expanded supersonic jet emitted from the exit section of a convergent nozzle has been extensively utilized by many molecular beam users. The expanding gas particles are quickly accelerated to the flow speed, so this rather simple device allows obtaining high Mach numbers and a substantial cooling of the gas. The particles form a very intense and nearly mono-energetic jet [58, 59] and the addition of a small mole fraction of a different species to the gas in the reservoir can generate a seeded molecular beam. In the latter, the behavior of the supersonic expansion remains similar to the pure gas model and the light gas carrier accelerates also the heavier molecular species.
This process has been studied and used as an effective tool for the production of cluster jet and molecular beams in the last decades leading to different applications [60, 61]. The free jet expansion has proven being useful both in simplifying the analysis of molecular spectra thanks to the freezing of translational and rotational degrees of freedom for advanced optical spectroscopy studies [62] and for the investigation nanoparticles in a unperturbed environment [63]. This technology is also widely employed for the production of molecular beams for cluster assembling, scattering experiments mass spectrometry applications. In a supersonic jet particles can be separated radially by their mass, allowing the aerodynamic separation of heavy molecules and isotopes [64].

All these applications are the results of many years of studies and researches. Otto Stern first realized and demonstrated the importance of molecular beams in his experiments, which granted him a Nobel prize in 1943 for the so called Stern-Gerlach experiment. Many impressive results were obtained from experiments involving molecular beams, which were produced from effusive sources. However these devices had many limitation resulting in low intense beams. A great improvement to molecular beams arrived from Kantrowitz and Grey in 1951, who proposed an apparatus for the production of a very intense molecular beam using the free-gas supersonic expansion from a high pressure reservoir into a low pressure vacuum chamber through a converging-diverging nozzle [58]. The authors used a converging-diverging nozzle in order to obtain gas streamlines parallel to the centerline, thereby increasing the intensity of the beams reducing the cost of the required vacuum pumps. However, boundary layer effects, due to viscous flow interaction with the nozzle walls in the diverging section were observed to have a negative impact on the beam intensity. Successively another improvement arrived from the removal of the diverging section of the nozzle, allowing higher beam intensities (Becker and Bier) [65]. The removal of the diverging section eliminated much of the viscous gas-surface interaction, so that most of the gas could expand isentropically except for interaction with the background gas. Therefore, nozzles without diverging section (capillaries or purely converging nozzles) have been predominantly used in molecular beam formation. They are also easier to design and fabricate.

In this work the free expansion of a plasma is used to produce a supersonic jet of neutrals and ions capable of creating thin films having specific nanostructures. The supersonic jet is generated by the pressure difference between two vacuum chambers connected through a converging nozzle. An accurate knowledge of the supersonic jet expansion is of great practical interest for PA-SJD. The neutral gas density along the jet can give a useful insight on how to effectively control the nanoparticles which are assembled in the deposited film by tailoring their size and speed. In addition to this, there is still a lack of accurate experimental data especially for the gas and at the low pressure regimes (below few Pa), where the continuum-regime assumption is often inaccurate [66] and the supersonic expansion of gas and plasma has not been fully explored experimentally. In this chapter we characterize and study the free jet expansion of an argon-oxygen gas mixture across a converging nozzle from a reservoir pressure held at constant pressure (8 Pa), to a lower pressure vacuum chamber, where the pressure can be varied (from 0.03 up to 8 Pa). Here we aim to characterize the density profiles of the neutral gas along the supersonic jet expansion, where thin film depositions have been formerly performed (placing a flat substrate normal to the jet) [6, 11], without generating the inductive plasma. We are able to study the behavior of the supersonic jet at very low pressures using a quadrupole mass spectrometer (QMS) to obtain separate measurements for different neutral species. The pressure in the higher pressure chamber was set at a constant value

to reproduce the experimental conditions optimized for thin films deposition [11]. We obtained a direct measurement of the density of gas neutral species employing a movable QMS. Experiments were performed in the absence of the plasma state to investigate the structure of the supersonic jet at different pressure ratios between the two vacuum chambers. After the description of the fluid theory which applies to our working conditions and we discuss the experimental results.

## 3.2 Experimental setup and diagnostics

The characterization of the gas expansion was performed reproducing the flow conditions already used for PA-SJD depositions, described in section of the previous chapter and shown in Fig. 3.1.

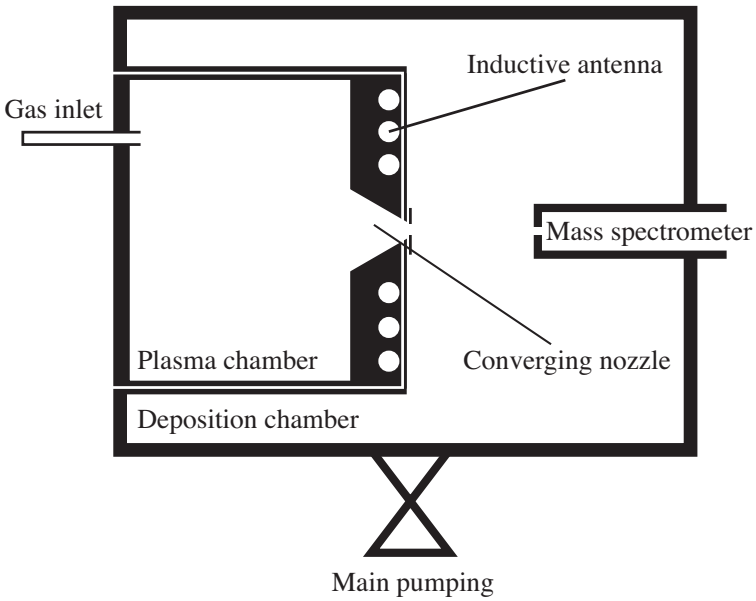


Figure 3.1: Schematic view of the experimental setup. The mass spectrometer sampling orifice can be moved horizontally inside the deposition chamber.

Argon and oxygen are injected directly into the first chamber using two separate mass-flow controllers. The gas mixture inside the plasma chamber can be considered well-mixed since the diffusion speed calculated at the experimental condition exceeds the flow velocity (respectively 1.26 and 0.04 m/s) [32, 33, 34]. The converging nozzle has the shape of a rounded rectangle (ending with an aperture 22×30 mm) closed by a 1 mm thick thin foil having a centered circular orifice (6.9 mm of diameter). A converging nozzle favors the formation of the supersonic jet by accelerating the gas particles to a sonic speed and has the practical advantage of allowing the use of different kind of orifices or slits, which can be easily replaced changing the thin foil. Rectangular slits were previously used for depositions [6], however we chose a circular orifice for this characterization to obtain an axis-symmetric jet. During

the measurements the pressure in the chambers is monitored using two capacitance pressure gauges. Their pressure reading precision is quite good in the pressure ranges where we operate, which are between 8-10 Pa in the plasma chamber, and 0.01-8 Pa in the deposition chamber. To monitor the pressure over a wider range of pressures (from $10^{-6}$ Pa to atmospheric pressure) two full range gauges (which couple a pirani and a cold cathode system) are also present inside the deposition chamber and the mass spectrometer. The pressures inside the plasma and the deposition chambers, in Fig. 3.1 named respectively $P_0$ and $P_d$, is controlled by the flow rate and the conductances of the orifice at the end of the nozzle and the gate valve over the main pumping group. $P_0$ can be easily accurately varied changing the flow rate of the gas. The small conductance associated with the circular orifice connecting the two chambers (about 4.8 l/s, measured experimentally at the working pressure values and slightly dependent from the pressure) allows us to change the pressure inside the deposition chamber $P_d$ (with negligible variations to $P_0$) by partially closing the gate valve which connects the main pumping group, thus reducing the effective pumping speed. The pressure ratio between the two chambers is defined as: $R = P_0/P_d$ and it can be varied from 40 to 1 to model the supersonic jet geometry and energy. As a diagnostic we used the Hiden QMS which was moved along the centerline of the supersonic jet, sampling the gas at different positions. This allowed the residual gas analysis of the supersonic jet at different positions of its expansion.

## 3.3 Supersonic free expansion theory

### 3.3.1 Formation and schematics

When a gas is left to expand into a vacuum chamber, a free expansion process takes place. If specific requirements are met, the expansion process can be isentropic (i.e. adiabatic and reversible) and a supersonic jet is formed. When the gas expands from a reservoir (at constant temperature and pressure) through an orifice into a partially-evacuated vacuum vessel, the gas undergoes a supersonic free jet expansion when there is a sufficiently large pressure drop across the nozzle. During this process the molecules are isentropically accelerated forming a two-dimensional jet structure [67, 68]. The gas thermal energy is quickly converted into fluid flow while the temperature decreases. Inside the jet, density and pressure quickly decrease with increasing distance from the nozzle while the Mach number M, defined as the ratio between the gas speed and the local speed of sound, increases. A fundamental parameter to characterize the free jet expansion is the pressure ratio R which corresponds to the ratio between the pressure upstream the nozzle (inside the plasma chamber) and downstream (the background pressure inside the deposition chamber). In order to achieve a supersonic regime a pressure difference across the nozzle is required. From the gas dynamics theory of a supersonic free jet [66], it can be

demonstrated that a value of R greater than:

$$R = \left(\frac{\gamma+1}{2}\right)^{\gamma/(\gamma-1)} \tag{3.1}$$

is sufficient to produce a slightly supersonic gas jet, where $\gamma$ is the gas specific heat ratio. This critical value for R is rather small: for almost every $\gamma$ it is enough to have (which corresponds to the case of a mono-atomic gas where ). In the converging section of the nozzle, if the pressure ratio is over its critical value, a sonic condition (where M is equal to 1) is established at the exit. Thus the gas is moving at the sound speed , where R is the ideal gas constant, T is the gas temperature and m its molar mass. Nozzles designed with both a converging and a diverging section can provide higher exiting supersonic speeds and nearly parallel streamlines, however we chose to use a converging section to eliminate gas-surface interactions inside the nozzle which affect the expansion and the deposition process. After the nozzle, the gas flows from the orifice with an initial sonic velocity into the deposition chamber, whose walls are far from the jet (many nozzle diameter units away), forming an under-expanded free jet. Along the jet the gas pressure is initially greater than the background pressure and the gas expands radially and axially. The radial velocity is very small if compared with the flow speed, while axially the gas particles are quickly accelerated up to a limit value forming a narrow speed distribution. From the energy conservation equation can be derived [66]

$$v_{limit} = \sqrt{\frac{2\gamma R T_0}{(\gamma-1)m}} \tag{3.2}$$

where $T_0$ is the gas temperature inside the plasma chamber. For argon and oxygen gas at room temperature this limit velocity is respectively 550 and 730 m/s. The geometry and the thermodynamical parameters of a supersonic jet can not be determined analytically. The section of the expanding jet is sketched in Fig. 3.2.

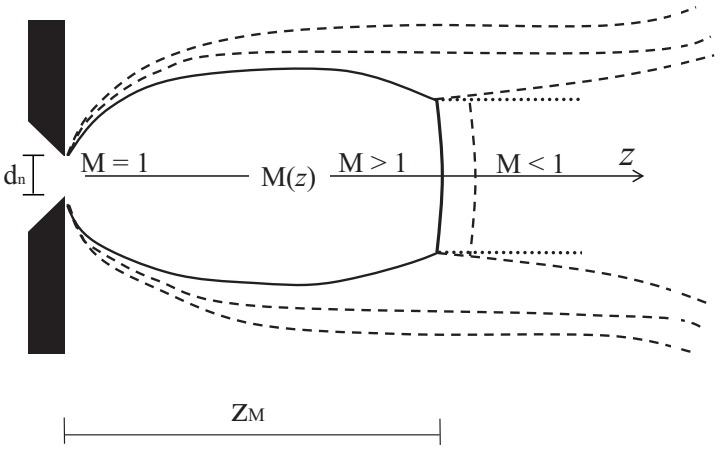


Figure 3.2: Schematic representation of the jet expansion across the nozzle. Full lines delimit the supersonic regions and dashed lines give an idea of the gas streamlines. The Mach number (M) variations and the Mach disk position $z_M$ are shown. $D_M$ represents the Mach disk diameter while $d_n$ the nozzle ending circular diameter.

The supersonic region, named zone of silence, is where the flow is supersonic and the Mach number is greater than 1. This region is delimited by oblique shocks and by a normal shock, the so called Mach disk represented as full lines in Fig. 3.2. The gas density and speed are maximized over the axis of symmetry (the $z$ axis in Fig. 3.2) and decay along the radial dimension upon reaching the oblique shocks where the gas becomes subsonic. The geometry of the expansion is scaling with the pressure ratio R. An increase of the pressure ratio produces longer jets, whose length scale with the square root of R. To obtain the expected Mach disk position $z_M$ and its approximate diameter $D_M$ it is possible to use some empirical equations given in [68] and [69]:

$$\mathrm{z_M} = 0.67 \cdot \mathrm{d_n}\sqrt{\mathrm{R}} \tag{3.3}$$

$$D_M = d_n(0.36R^{0.6} - 0.59) \tag{3.4}$$

where $d_n$ is the circular orifice diameter. Both these relations are independent from $\gamma$ and in particular this equation has been verified in a wide range of pressure ratios [66] which are close to those analyzed in this work.

### 3.3.2 Calculation of density

We are interested in the calculation of the gas density along the expansion because it is the main quantity which is measured by the quadrupole mass spectrometer. Across the Mach disk there is a transition which leads the gas from supersonic jet to a subsonic regime. In high pressure systems, where the pressure before the

Mach disk is lower than the background value, this transition can be an abrupt gas recompression in which the background values for temperature, pressure and density are restored. For low pressure conditions the transition becomes smoother. If the gas parameters upstream of the nozzle are known, it is possible to estimate their values along the centerline of the expansion. Accurate fitting equations for the Mach number and the pressure along the centerline of the expansion can be found in literature [68] based on the assumption of an inviscid isentropic flow inside the jet and valid for $z > d_n$. According to [68], we have:

$$M(z) = A\left(\frac{z-z_1}{D_n}\right)^{\gamma-1} - \frac{1}{2}\left(\frac{\gamma+1}{\gamma-1}\right) \Big/ \left(A\left(\frac{z-z_1}{D_n}\right)^{\gamma-1}\right) + C\left(\frac{z-z_1}{D_n}\right)^{-3(\gamma-1)}$$

and

$$\frac{P(z)}{P_{plasma}} = A^{\frac{-2}{(\gamma-1)}}\left(\frac{\gamma+1}{\gamma-1}\right)^{\frac{\gamma}{(\gamma-1)}}\left(\frac{\gamma+1}{2\gamma}\right)^{\frac{1}{(\gamma-1)}}\left(\frac{z-z_2}{D_n}\right)^{-2}$$

Where for a monoatomic gas $\gamma = 1.667$, $A = 3.26$, $z_1 = 0.075D_n$, $z_2 = 0.04D_n$ and $C = 0.31$; for a diatomic gas $\gamma = 1.4$, $A = 3.65$, $z_1 = 0.4D_n$, $z_2 = 0.13D_n$ and $C = 0.2$. These equations are evaluated numerically and plotted in the following figures:

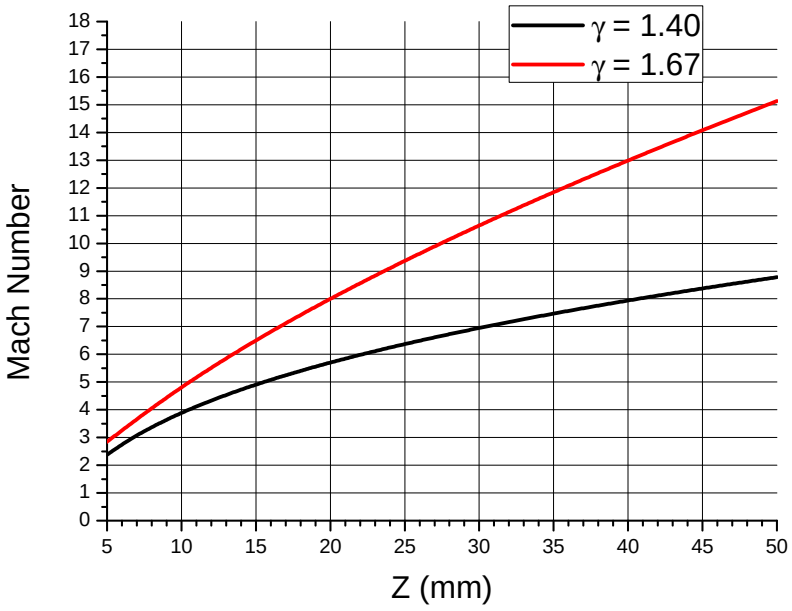


Figure 3.3: Numerical calculation of M along the axis of and ideal continuum expansion expansion; z=0 corresponds to the position of the orifice.

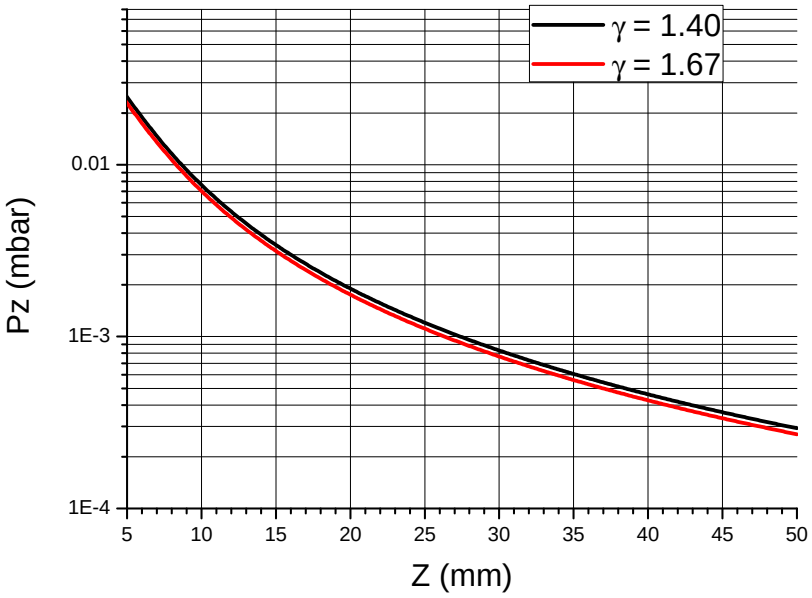


Figure 3.4: Numerical calculation of P along the axis of and ideal continuum expansion expansion; z=0 corresponds to the position of the orifice, background pressure upstream the aperture was set to 8 $\cdot 10^{-2}$.

We calculate for our set-up Mach numbers up to 8 just before the shock region. The pressure along the centerline of the expansion can be estimated if the upstream value is known. A relation between the pressure on a flat plate and its distance from the orifice z is determined from numerical calculation in [70]. This equation is valid for a supersonic jet and accurate for $z > 0.5d_n$. Assuming a rapid and inviscid expansion of the gas, it is possible to derive a relation between the density along the centerline and the axial position $z$. From the adiabatic relation between density and pressure we can define:

$$n = \frac{n_0}{\left(a\left(z/\mathrm{d_n}\right)^2 - b\left(z/\mathrm{d_n}\right) + c\right)^{1/\gamma}} \tag{3.5}$$

where $n_0$ is the gas density in the plasma chamber and $a$,$b$, $c$ are numerical constants given in [70] respectively equal to 1.44, 0.65 and 0.87. It is important to note that this law derived from [70] is well comparable with the more known equation, relating pressure to the centerline coordinate $z$, given in [68] for $z > d_n$. The equations above apply well to a continuum regime, where the gas can be described by means of fluid equations. At very low pressure there is almost no interaction between the gas particles especially along the jet while the shock regions become smoother and may vanish [68, 71]. The parameter used to evaluate the flow regime is the Knudsen number $K_n$, defined as the ratio between the gas mean free path and the typical length scale of the system. For values of $K_n$ lower than 0.1 the flow regime can be

considered continuum, while for values of $K_n$ greater than 1, the flow is molecular. The intermediate region is a transitional regime. Inside the plasma chamber the characteristic length is the vacuum vessel height (100 mm). By calculating the gas mean free path in the plasma chamber it is possible to evaluate a value for $K_n$ about 0.009. Inside the zone of silence, $K_n$ can be calculated by estimating the gas mean free path from the collisional frequency for a supersonic jet [72] and using as the typical length of the system the Mach disk diameter $D_M$ or the Mach disk distance from the orifice $z_M$. In both cases along the $z$ axis $K_n$ increases from about 0.1 up to 1 for the different gas pressured used experimentally, leading to a transitional regime. When the mean free path of the gas is long, the Mach disk thickens. After the supersonic jet the typical system length is of the order of the vacuum vessel radius (160 mm) and the regime is still transitional as the Knudsen number is ranging between 0.2 and 0.03 depending on the pressure in the deposition chamber.At low Knudsen numbers, when a flat obstacle is placed normal to the jet, a bow shock-wave is formed, detached from the obstacle [73]. When comparing our measurements to any model, it is important to remember that the QMS can alter the jet structure; however at transitional regime the gas mean free path of the jet is between 2 and 20 mm, thus the perturbations are limited. When the spectrometer is moved very close to the nozzle ($z < 0.5d_n$), a small increase in the plasma chamber pressure $P_0$ can be spotted during the measurements, anyway this increase is less than 4% of its initial value for $z = 0.25d_n$.
After the Mach disk in this transitional regime, if the gas is not fully expanded, we can expect that pressure and density reach their background values after few mean free path lengths following a quadratic trend as the particles are free to expand in every direction subsonically. The density along the $z$ axis can be fitted with:

$$n(z) = n_d + \frac{A}{z^2} \tag{3.6}$$

where $n_d$ is the background density inside the deposition chamber and $A$ is a fit parameter which scales with the mean free path.

### 3.3.3 Separation factor

When operating with a mixture of gas having comparable molecular fractions, it is possible to describe the total fluid derived using average values for the gas mass and specific heat ratio if the gas is well-mixed. For a gas mixture of argon and oxygen respectively having 0.4 and 0.6 molar fractions it is possible to estimate $\gamma \simeq 1.5$ . Working with gas mixtures, other phenomena have to be taken into account. A strong radial pressure gradient is present along the jet expansion: the different gas components can drift perpendicularly to the jet axis due to pressure diffusion [74, 75, 76]. The diffusion speed is proportional to the inverse square root of their mass, so that heavier species are retained along the centerline. This effect

is negligible for high pressure jets [66], while for low pressure expansions it can generate a separation of the gas species. The gas separation of a binary mixture can be described by introducing a separation factor [77]:

$$\alpha = \frac{n_H/n_L}{(n_H/n_L)_0} \tag{3.7}$$

where the subscripts $H$ and $L$ refer to the heavier and the lighter species in the gas, while 0 denotes to the conditions inside the plasma chamber.

## 3.4 Experimental results: The neutral gas expansion

### 3.4.1 Data collection and analysis

Mass spectra for neutral species inside the deposition chamber were measured at the limit pressure conditions (i.e. $P_d \simeq 10^{-6}$ mbar and $P_{spectrometer} \simeq 10^{-7}$ mbar). These spectra were used to ensure the reliability of the vacuum system checking for leakages and to observe which impurities were already present inside the chamber, before injecting gas or generating the plasma.

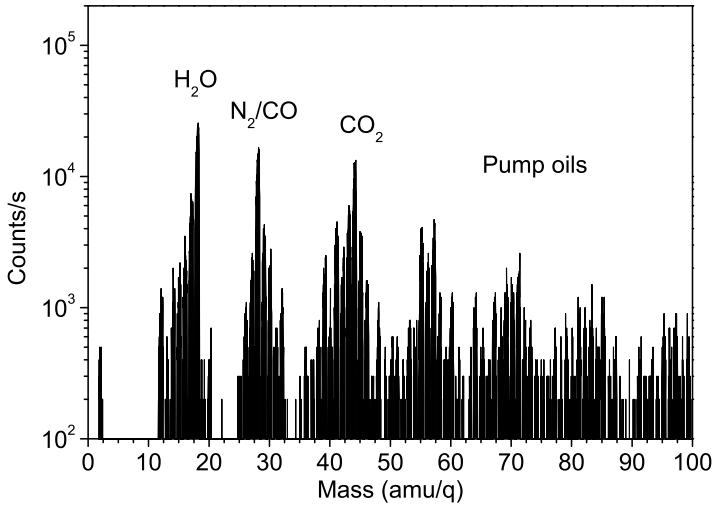


Figure 3.5: Neutral mass spectrum measured inside the deposition chamber, without injecting any gas. Several peaks are well distinguishable and extend up to masses over 100 amu. The mass detected can be mainly related to the pump oil generated by the rotative pumps, to retained inside the vacuum vessel and to air due to small leakages.

In Fig. 3.5 a neutral mass scan measured inside the deposition chamber at 99 mm of distance from the nozzle is shown. This spectrum was acquired at the limit pressure $P_d \simeq 10^{-6}$. Many peaks are well distinguishable, most significant are water (M=18,17 amu/q), air (M=28,32,16 amu/q), carbon oxides (M=28,44 amu/q) and pump oils hydrocarbons, listed in the figure.

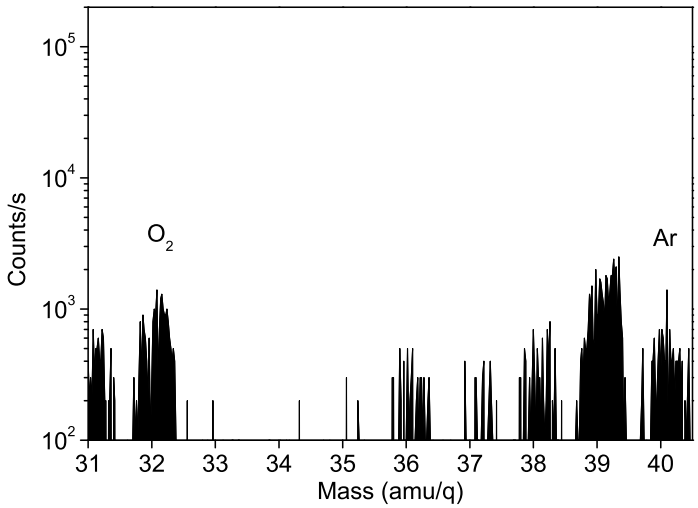


Figure 3.6: Particular of the mass spectra previously shown. Here it is possible to observe with more resolution the region of the spectra between the peaks of molecular oxygen and argon (32 and 40 amu). These two peaks are slightly observable, their count values are limited and due to trace impurities.

Fig. 3.6 shows a particular of the spectrum already plotted in Fig. 3.5, in the range between M=31-40.5. Here it is possible to observe with higher resolution the region where the peaks of argon and molecular oxygen are located. The signal measured for these two species is very low ($< 10^3$), and then negligible if compared to the signal measured in the following spectra (about $10^6$).

To investigate the properties of the jet we have acquired several mass spectra with the QMS using the same experimental conditions in the first chamber (an argon-oxygen mixture respectively 0.4-0.6 molar fractions, at a total gas pressure of 8 Pa) and modifying the pressure in the second vacuum chamber for different experiments. QMS signal data are expressed as counts per seconds obtained over different masses scanned. We refer to the background pressure in order to convert the mass spectrometer counts per seconds into Ar and $O_2$ density values. For each position, the mass peaks relative to $O_2$ (32 amu) and Ar (40 amu) were acquired, their area was calculated and renormalized following a previous calibration to evaluate the density of the two gases.

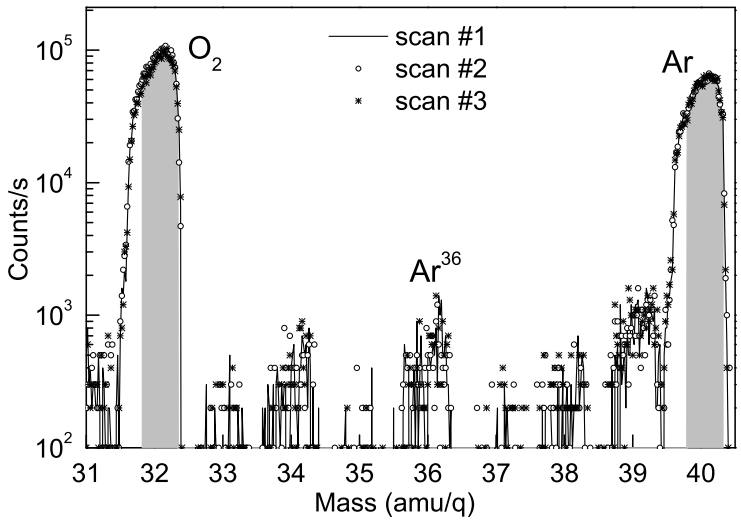


Figure 3.7: Particular of a typical neutral mass spectrum measured in Ar-$O_2$ gas mixture (0.4 to 0.6 molar fractions). The pressure inside the plasma chamber was 8 Pa, the pressure inside the deposition chamber was set to have a pressure ratio $R = 28$. The area used to evaluate the species density is shown in grey.

Figure 3.7 shows a mass scan where the peaks corresponding to argon and oxygen are clearly visible. The measurements show an excellent stability and reproducibility as it can be seen from the comparison between three successively acquisitions of the same spectra in Fig. 3.7. Statistical errors associated with averaging different scans are smaller than 1%.

### 3.4.2 Typical profile

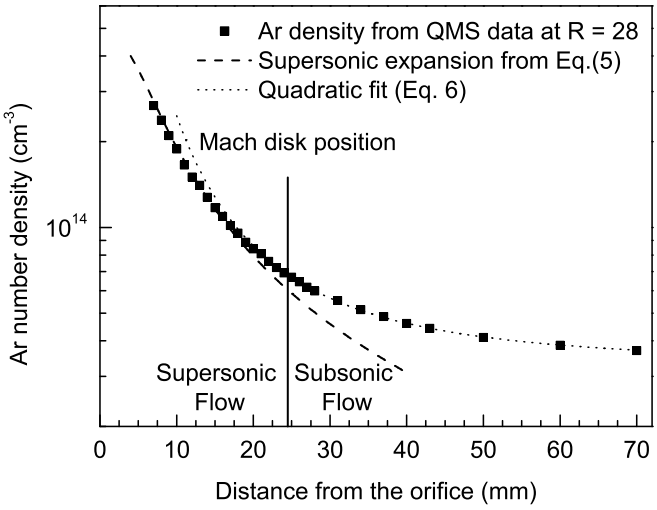


Figure 3.8: Neutral gas profile for argon-oxygen mixture, without the plasma, showing the Ar number density measured with the mass spectrometer. The pressure inside the plasma chamber was 8 Pa, the pressure inside the deposition chamber was set to have a pressure ratio $R = 28$ . QMS data are reported as black squares together with the isentropic expansion law derived in the previous chapter (dashed line) and with a quadratic fit (dotted line). The Mach disk location is indicated by a vertical bar over its position (24 mm from the orifice). Across the Mach disk there is a transition between the supersonic flow (dashed line) and the subsonic flow (dotted line).

Figure 3.8 shows a single experiment at high pressure ratio ($R = 28$). The black squares represent the argon density measured by the QMS. In the supersonic region the gas expands quickly and the profile is in good agreement with the dashed line in Fig. 3.8 which represents the expected density trend defined by Eq. (3.5). Over the expected Mach disk position predicted by Eq. (3.3) the transition from the supersonic flow into the subsonic regime can be spotted as a detachment from the isentropic flow. This is in agreement with the vanishing Mach disk behavior suggested for the transitional regime [68].
The absence of a strong shock region, commonly observed in high pressure jets [66], is an interesting feature for thin films deposition applications, since it is possible to avoid reflected shocks on a sample placed inside the gas expansion [73]. After the Mach disk location the gas expands slightly following the quadratic fit (Eq. 3.6), as shown by the dotted line in Fig. 3.8.

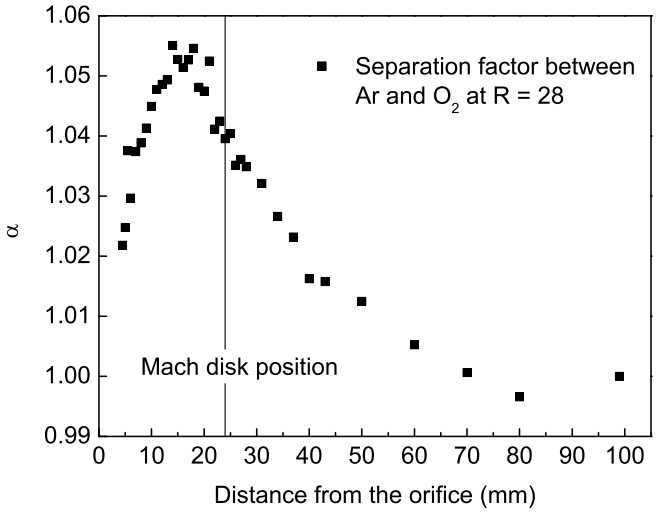


Figure 3.9: Separation factor defined in Eq. (3.7) and calculated from the experimental Ar and $O_2$ density profiles. The pressure inside the plasma chamber was 8 Pa, the pressure inside the deposition chamber was set in order to have a pressure ratio $R = 28$. The Mach disk location is indicated by a vertical bar over its position (24 mm from the orifice).

The transition from the supersonic jet to the subsonic regime is clearer by looking at the variation of the gas concentration as shown in Fig. 3.9. In a supersonic jet occurs an enrichment of heavier masses along the centerline, due to their higher inertia. A variation of gas concentration takes place during the expansion: heavier masses (Ar) are less diffusive and are retained along the central position (which is the one sampled by the QMS), lighter masses ($O_2$) can slip away from the centerline. This increase in the Ar concentration was calculated by the QMS data and expressed as the separation factor $\alpha$ defined in Eq. (3.7) which is shown in Fig. 3.9. The Ar enrichment increases up to few millimeters just before the Mach disk position then begin to decrease. These kinds of profiles for the separation factor $\alpha$ are similar to those reported in literature for higher pressure regimes [74, 75, 76].

### 3.4.3 Gas expansion at different pressure ratios

In Fig. 3.10 and 3.11, QMS data for Ar and $O_2$ at different pressure ratios R are shown. For each different experiment the pressure in the deposition chamber was raised by closing the gate valve which connects the main pumping group. The gas pressure inside the plasma chamber was almost unaffected by the variation of the pumping speed.

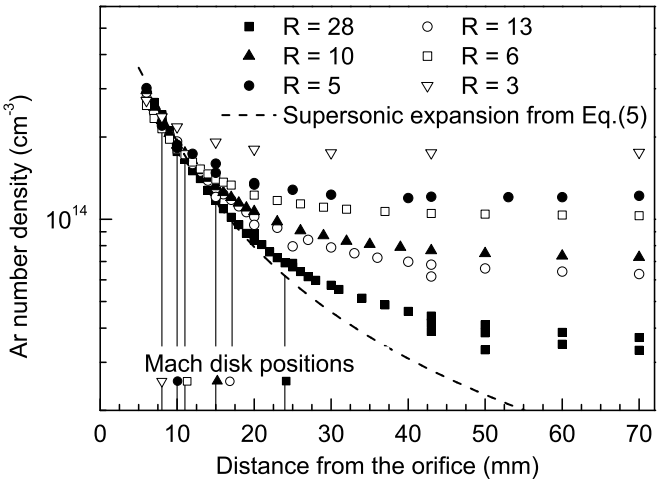


Figure 3.10: Neutral gas profile for argon-oxygen mixture, without the plasma, showing the Ar number density measured with the mass spectrometer at different pressure ratios. The pressure inside the plasma chamber was 8 Pa, the pressure inside the deposition chamber was varied to have a pressure ratio ranging from 28 to 3. Different values for R imply different positions for the Mach disc $z_M$ (defined in Eq. 3.3) which determines the end of the supersonic jet. The locations of the Mach disk for different series of data are shown in the graph with a vertical bar over the corresponding symbol.

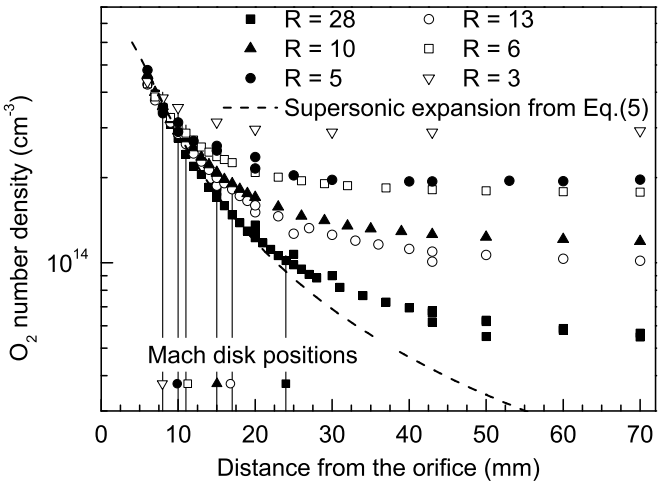


Figure 3.11: Neutral gas profile for argon-oxygen mixture, without the plasma, showing the number density measured with the mass spectrometer at different pressure ratios. The pressure inside the plasma chamber was 8 Pa, the pressure inside the deposition chamber was varied to have a pressure ratio ranging from 28 to 3. Different values for R imply different positions for the Mach disc $z_M$ (defined in Eq. 3.3) which determines the end of the supersonic jet. The locations of the Mach disk for different series of data are shown in the graph with a vertical bar over the corresponding symbol.

When R decreases, the Mach disk position is shifted closer to the orifice. The

gas expands following the expected supersonic expansion equation (dashed in the graphs) until the Mach disk position (vertical bars in Fig. 3.10 and 3.11) where the transition to the subsonic flow takes place as previously described. At lower pressure ratios, there is a higher background pressure and a shorter mean free path. The latter can range from about 5 mm when the pressure ratio is equal to 3, up to 25 for the highest value of R. Then, as it could be expected, inside the subsonic region the density reaches earlier the background values for higher background pressure. After about 3 mean free path lengths from the Mach disk, the density over the expansion axis is nearly constant at the background value for all the experiments shown in Fig. 3.10 and 3.11.

## 3.5 Summary and conclusions

Using a QMS to measure the neutral gas and ion densities we characterized the profile of a low pressure supersonic jet used for thin film depositions. The supersonic expansion was studied for the neutral gas case in a binary mixture of argon and oxygen. The flow regime in these experiments is mainly transitional. The results for the neutral gas case are in good agreement with the viscous isentropic model. However no shock compression can be spotted over the Mach disk, as it is commonly observed in higher pressure jets; instead we observed a smooth transition to a subsonic regime, in which the background density values are reached within about 3 gas mean free path lengths from the Mach disk location. The transition is denoted by the detachment from the predicted isentropic expansion equation and its location was in fair agreement with the predicted position of the Mach disk in an extended range of pressure ratios. This smooth transition observed for the neutral species is highly desirable for thin film deposition applications since it can prevent the sudden stop of nanoparticles over the Mach disk and reflected shocks over the sample which can affect the film growth. Gas separation phenomena have been observed along the jet. With the QMS it was possible to measure the Ar enrichment over the supersonic jet axis. A maximum excess of about 5% was obtained for argon respect to oxygen. In the case of the plasma we observed a supersonic jet containing both neutral and positively charged particles.

CHAPTER

# 4

# PLASMA CHARACTERIZATION

## 4.1 Introduction

Low-temperature plasma have been applied to materials synthesis, structuring and processing for decades. However, learning how to use such plasma to allow these processes to occur at nanoscale dimensions has only become critical since the rapid growth of nanoscience and nanotechnology in last two decades. In particular by the mid-1990s to early 2000s, several striking advantages of plasma applications at the nanoscale had been demonstrated. Successful applications of ionized gases in nanoscale synthesis and processing were reported for:

- a larger and larger number of nanoscale objects, structures, architectures, arrays and patterns, with a continuously increasing structural complexity and improving functionality;
- both basic nanotechnology approaches, namely top-down and bottom-up nanofabrication;
- a rapidly expanding variety of materials systems, which started from simple carbon- and silicon-based systems and expanded into a very large number of organic and inorganic materials, including complex multi-element systems, polymers and even biological cells and tissues;
- a multitude of ionized gas systems which currently range in size from the weakly ionized plasmas of stellar envelopes with astrophysical dimensions down to the micrometre dimensions of microplasmas. These systems use precursors

in all three basic states of matter (solid, liquid, gas) and produce ionized gases with vastly different properties such as densities, temperatures, lifetimes, reactivity and thermal non-equilibriums;

- a very broad range of applications ranging from more traditional microelectronics (which to a very large extent is based on plasma-assisted processes) to health care, medicine, nutrition, agriculture, energy conversion and storage, environmental monitoring and remediation, national security, space missions, to mention just a few.

Indeed, further progress of the field required a deep understanding of the underlying physical and chemical mechanisms that led to the many and various newly discovered plasma-related phenomena that in turn resulted in new and fascinating nanoscale structures and assemblies. For PA-SJD a detailed understanding of the plasma in the first chamber and of the plasma expansion is fundamental in order of being able to control the growth and the morphology for nanostructured depositions which are closely related to the nanoparticles energy and diameter.
In this chapter we characterize and study the free jet expansion of an argon-oxygen plasma across a converging nozzle from a reservoir pressure held at constant pressure, to a lower pressure vacuum chamber, where the pressure can be varied providing different pressure ratios. Our aim is to characterize the density profiles of the neutral gas and the ions along the supersonic jet expansion, where thin film depositions are performed (placing a flat substrate normal to the jet) [6, 11].
In addition to this, we want to study the behavior of the supersonic jet at very low pressures using a quadrupole mass spectrometer (QMS) to obtain separate measurements for different neutral and ionic species. The pressure in the higher pressure chamber was set at a constant value to reproduce the experimental conditions optimized for thin films deposition [11]. We obtained a direct measurement of the density of gas neutral species, the positive ion fluxes and their energy along the expansion employing a movable QMS. Experiments were conducted creating a reactive plasma into the first vacuum vessel observing the spatial distribution of both neutral and positively charged particles along the expansion.
Plasma properties were simultaneously measured by optical emission spectroscopy (OES) observing the emission spectra from atoms, molecules and ions present in the plasma chamber and electrical diagnostic, acquiring time series of voltage and current flowing through the radiofrequency antenna of the ICP. Langmuir probes were also used to evaluate the main plasma parameters inside the plasma chamber.

## 4.2 Plasma theory

### 4.2.1 Inductively coupled plasma source

Inductive plasma sources allow the generation of a high density plasma by using radio-frequency electric fields [78]. Compared to capacitive discharges, where the discharge is maintained by the electric field which arises from the potential difference between and electrode and a counter-electrode, inductive sources allow the production of higher density plasma at low potential. Applying RF signal to a non-resonant inductive coil (planar or cylindrical), the power is transferred to the plasma by the coupling between the coil current and the induced plasma current, similarly to the working principle of a transformer. In this way it is possible to reach a very high power transfer efficiency, without exposing any electrode or similar part directly to the plasma which could result in the production sputtering products (which are highly avoidable especially for thin films deposition applications).
Commonly an inductive source exhibits two different operating regimes: a dim low power regime named E-mode, where the discharge is mainly driven by a capacitive effect between the coil and the chamber walls, and a bright high power regime named H-mode, where the discharge is fully inductive. The transition between these operating regimes is well distinguishable and takes place after a certain power value which depends on the geometry of the source and on the plasma chemical composition and pressure. It is important to ensure that H-mode conditions are established when choosing a RF-power value for a plasma treatment. During the H-mode it is also commonly observed a net increase of the charge density of the plasma.
Electron energies in this kind of sources generally do not exceed values of about 5 eV and are uniformly distributed over the plasma. Usually they are responsible for the excitation, ionization and dissociation of the different species. Because they have a small mass they play a dominant role in maintaining the electrical field within a plasma.
Two main ionization mechanisms are dominant in low pressure inductive discharges: ionization by electron impact and charge transfer ionization. The first is due to electrons which are accelerated by the RF-field, the second is related to a very frequent process in cold plasma in which the charge is transferred from an ion to another during a collision. The cross section of the charge exchange is nearly constant in energy and dependent from the mass. The process becomes resonant (no energy losses) when the reacting atoms or molecules are identical. Information on the processes between charged ions and neutral atoms can be found in literature [79]:

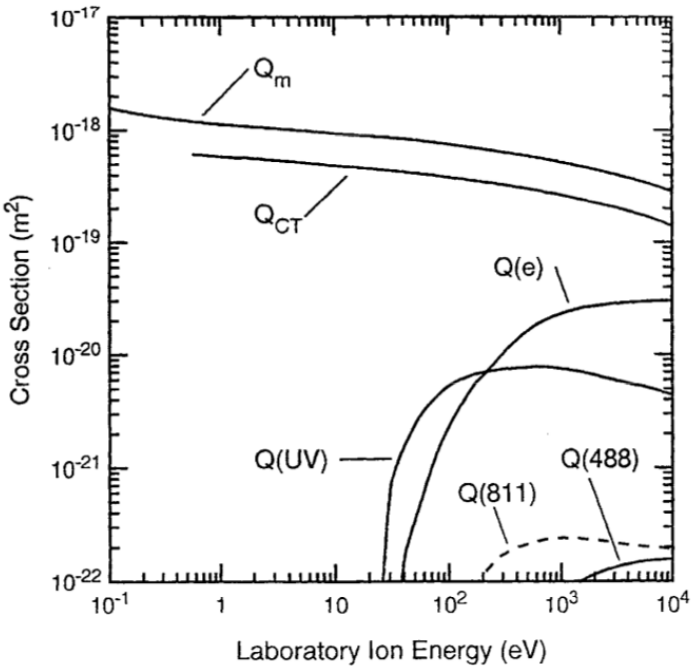


Figure 4.1: Cross section for $Ar^+$ - Ar collision versus laboratory energy. The processes shown are: charge transfer $Q_{CT}$, momentum transfer $Q_m$, electron production Q(e) and then some emission lines Q(488), Q(811), Q(UV).

Charge transfer becomes important when it takes place out of the plasma region, while ions cross sheath region (such as the supersonic jet), anyway this phenomenon will be further studied in the following chapter. Inside the plasma chamber, the ion initial energy distribution can be assumed to be a Maxwellian function peaked over approximately their thermal energies [37]. As the ions enter the supersonic jet, their trajectories are influenced both by the gas expansion and by electron friction and electric fields [80]. In particular a potential drop is expected between the main chamber and the supersonic expansion region, which can be considered a pre-sheath [40]. This results in a shift of the ion energy distribution functions to an energy comparable with the potential drop [81]. Ions colliding while crossing this sheath will have less total energy providing low-energy tails in the distribution functions [82].

### 4.2.2 Supersonic plasma jet

Expanding plasma are interesting from a fundamental as well as from a technological point of view. Nowadays expanding plasma are very used in plasma processing. A particular feature of an expanding plasma is the different behavior of the electrons and heavy particles during expansion, due to their large mass difference. As a consequence, if the expansion is strong, charge separation can occur, which leads to the generation of an electromagnetic field [80, 83]. This electromagnetic field influences the behavior of the charged particles in the expanding plasma. An-

other interesting phenomenon in free expanding plasma is the coupling between the ionization-recombination phenomena and the flow properties as electron temperature and electron density.

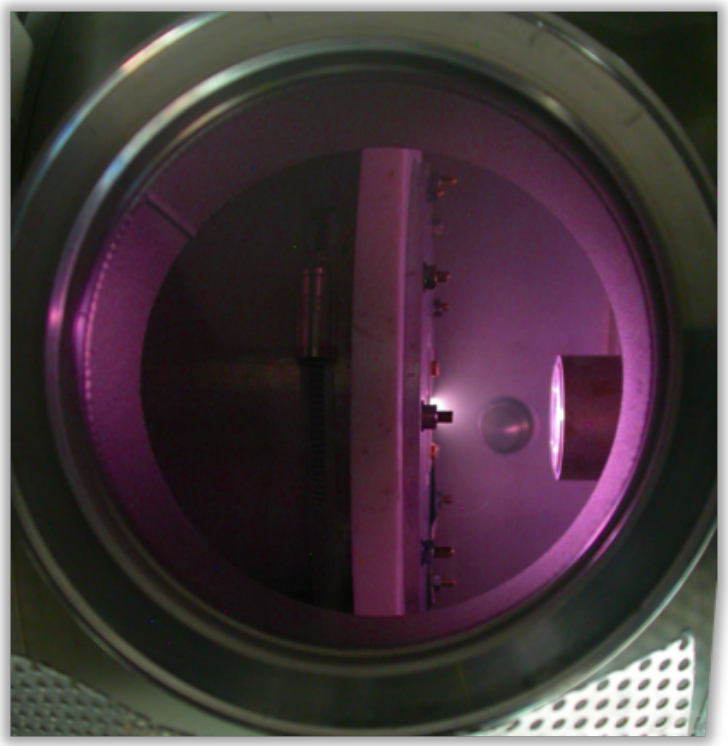

Figure 4.2: Photography of the supersonic jet exiting from the plasma source taken from the main quartz window facing the center of the deposition chamber. The QMS head is visible on the right, sampling the plasma jet.

The expansion of a rarefied plasma is different by the expansion of a simple gas since it is influenced also by the energy of the charged particles, by charge recombination and by electric fields. However it was demonstrated that the behavior of the electron and neutral-particle density in the expansion of a freely expanding plasma jet in argon can be described by the model of Ashkenas and Sherman [68]. The neutral heavy particles do not seem to be influenced by the presence of the plasma. For ions this can be different, especially in the shock region. Ion mean free path is smaller than the one calculated for neutral species, but it is still comparable with the expansion length. The neutral gas can be considered partially independent from the charged particles because of the low collision rate. The ion trajectories are influenced both by the gas expansion and by electron friction and electric fields. The density profiles for neutral and ion species over the centerline of the supersonic jet can be very similar even if their residence times in the jet are different. Ions times of flight along the jet are typically between 1 or 3 $\mu$s [40], one order of magnitude shorter than those for the neutral gas previously calculated.
As long as the expansion process can be considered adiabatic and collision-less, the

isentropic flow model derived from [70] in Chapter 3 can be used to describe both the neutral gas and the ion expansion. If recombination effects can be neglected, ions expand with an axial profile [83], at least in the absence of electric field inside the jet region. Conversely the ions and the neutral particles behave independently in the shock front. In fact electrons with their larger mobility leak out of the shock front, creating an excess of negative charge. Ions are pulled outside of the shock front by the created electric field.

## 4.3 Experimental setup and diagnostics

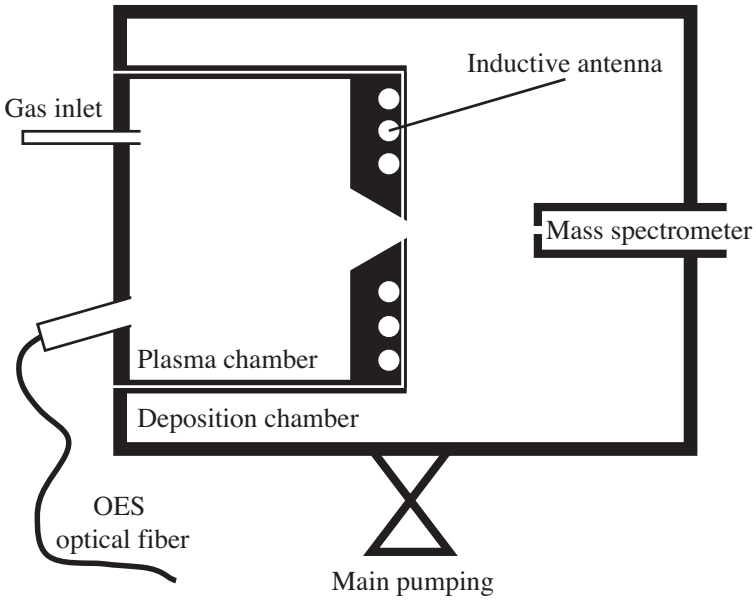


Figure 4.3: Schematic view of the experimental setup. The mass spectrometer sampling orifice can be moved horizontally inside the deposition chamber. OES were acquired from the oblique window (16° to the perpendicular) facing the plasma chamber alternatively to Langmuir probe measurements.

Figure 4.3 shows the experimental setup which was used for the plasma measurements, which is very similar to what was already described in the previous chapter. The inductive coil, located on the right side of the plasma chamber, was fed by a RF generator, connected through a L-type matching box whose parameters were manually modified in order to keep the proper tuning (no reflected power).
For each operation, the gas fluxes in the plasma chamber were first set in order to reach a pressure of about 8 Pa with a 2:3 mixture of Ar and $O_2$. A high concentration of oxygen is fundamental inside the plasma chamber to properly dissociate the precursor, anyway argon gas is also important to create a stable plasma without the requirements of an excessively high power input, as we will demonstrate later on. The pressure in the deposition chamber can be adjusted to set a desired pressure ratio R. A ICP plasma is generated increasing the power flowing into the planar coil

and regulating at each step the L-type matching network to ensure the maximum power transfer. For power values below 175 W the plasma appears in a dim and low density state where the coupling between the antenna and the plasma is just partial, the so called E-mode. As the power increases, a clear transition happens upon reaching the H-mode in which the coupling is fully inductive and the main ionization mechanism which sustains the plasma is the power transfer between the current flowing inside the coil and the plasma itself. At 450 W the plasma is stable and the discharge is purely inductive.
The electrical scheme is shown in the following figure:

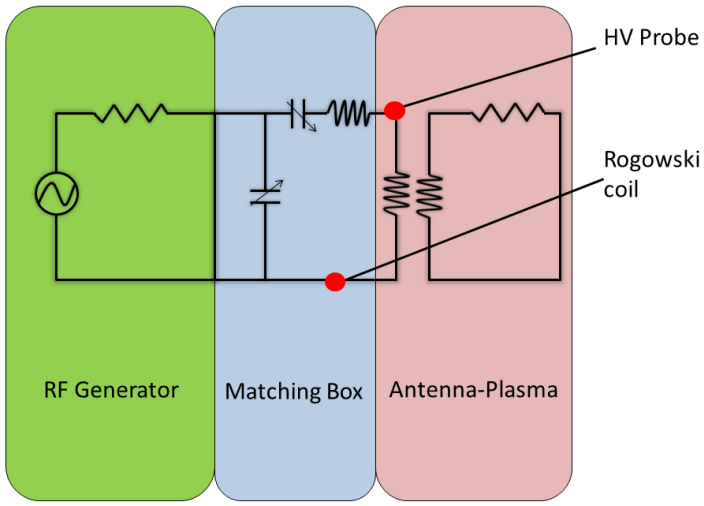


Figure 4.4: Schematic of the RF circuit and coupling. The red dots show where the electrical probes were located.

In Fig. 4.4 two red dots highlight the positions of the high-voltage probe and the Rogowski probe, for measuring respectively the voltage drop across the coil and the current flowing inside. During each plasma discharge, the electrical parameters were observed measuring times series of voltage and current at the two different side of the planar antenna. The voltage directly exiting the matching box was measured using a high-voltage probe (Tektronix P6015A), while the current flowing in the antenna was acquired with a Rogowski probe positioned at the grounded side of the coil. Both signals were simultaneously acquired using a digital oscilloscope (Agilent infinium MSO8104A) at 4 GHz sampling frequency to obtain a detailed electrical characterization.
Optical emission spectroscopy (OES) is a well know non-intrusive diagnostics which has already been applied in many plasma discharges [84, 48]. Revealing the light emitted from atoms, molecules and ions which are excited from free electrons in the discharge, it is possible to understand the main reaction processes in the plasma. The intensity of emission lines can identify chemical species allowing to gain insight

about their abundances. From the quartz window facing the plasma chamber optical emission spectra (OES) were acquired using two different low resolution spectrometers, as already described in Chapter 2.
Alternatively to optical measurements, a RF-compensated Langmuir probe was inserted in the plasma chamber removing the quartz window. In order to obtain the real current-voltage characteristic in a high RF environment, we used a Langmuir probe with a compensating circuit, again, described in Chapter 2.
The QMS was the main diagnostic used to collect data and it was employed to characterize the formation of the supersonic jet seeded with nanoparticles reproducing the experimental conditions already optimized and adopted for thin film depositions [6].
Measurements were performed inside the plasma chamber and along the jet using the diagnostics described above for different experimental conditions: at different RF-power values, at different Ar-$O_2$ gas mixtures, observing the netural and ion profile along the jet and observing the ion energy distribution functions. The main results of these measurements are shown and analyzed in the following sections.

## 4.4 Experimental: Plasma characterization

### 4.4.1 Electrical characterization

The generation of the inductive plasma generally increases the measured pressure in the plasma chamber, usually from 8 to 10 Pa for the pressure. This is both due to the radiofrequency effects on the pressure gauges and to an increase in the temperature. Temperatures about 180°C were measured inside the plasma chamber at 450 W in previous experiments. During each plasma discharge time, series of voltage and current across the antenna were acquired with a digital oscilloscope. These two values were analyzed observing the signal amplitude and relative phase shift, which were then converted into real voltage, current and phases after a calibration at 13.56 MHz of the probes. The rms voltage across the coil and the rms current flowing inside are shown in Fig. 4.5 for different RF-power value.

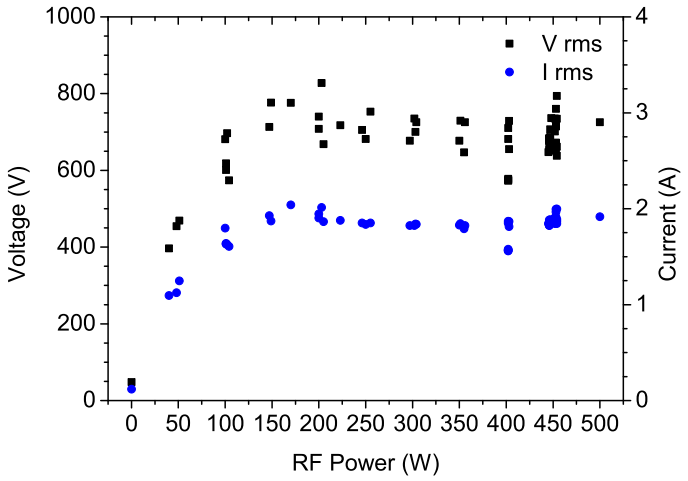


Figure 4.5: Electrical discharge data show a clear transition increasing the power input. The rms voltage and current are displayed on different Y-axes. As power is raised, the voltage and current seems to increase with the squared value of the power. When the fully inductive coupling is reached (H-mode) the displayed parameters rise slightly.

Power, voltage and current are related by the following equations:

$$P(t) = V(t) \cdot I(t) \tag{4.1}$$

$$< P(t) >= V_{rms} I_{rms} cos(\phi) \tag{4.2}$$

where the term in brackets is the average power and $\phi$ the phase shift between voltage and current. At low power input, there is a linear rise in both voltage and current, underlining small phase variations. In particular the steep rise at low power is due to the E-mode, where the voltage is proportional to the square root of the power. Increasing the power output from the generator a sharp transition between the E and the H-mode takes place about 175 W. Over this transition the phase between current and voltage has a wide variation until the H-mode is fully established. After the H-mode is fully established, the voltage starts rising linearly with the power level, at least in the limited range considered. It is possible, referring to the electric circuit shown in Fig. 4.4, to evaluate the impedance of the antenna-plasma load (if the coupling is ideal, the impedance of the coil should be equal to the plasma impedance), defined as:

$$Z_{resistance} = \frac{V}{I} cos(\phi) \tag{4.3}$$

$$Z_{reactance} = \frac{V}{I} sin(\phi) \tag{4.4}$$

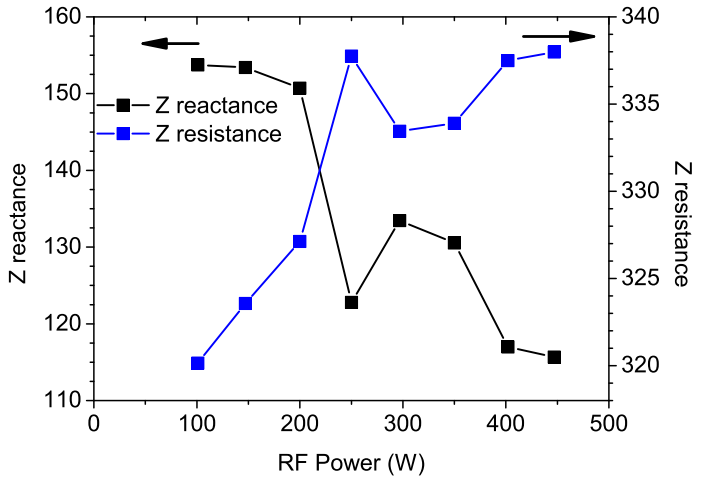


Figure 4.6: Resistance and reactance of the total load $Z$ of the coil antenna. Across the E-H mode transition (at 175 W) the discharge becomes inductively coupled, as it can be observed from the steep increase of the load resistance and the decrease of the load reactance.

Load resistance represents the real part of the total load, which is dominated by the plasma contribution, and starts to increase as the transition happens, and to stabilize in the H-mode. Load reactance, the imaginary part of the total load, is initially dominated by the antenna inductance and decreases as the plasma coupling becomes inductive, as expected from the simplified ICP model as a transformer [6].

### 4.4.2 OES analysis

Emission spectra were measured using different spectrometers and optical fibers (described in the experimental set-up section) directly in the first chamber during each plasma discharge. The line emission from the atoms in the plasma, dark subtracted and corrected by the sensitivity of the instruments, can be used to retrieve information on the species concentration or on the plasma parameters (electron temperature and density).

An insight on the main reactive species in the plasma chamber can be gained from Fig. 4.7 where a typical spectra is plotted. The most intense lines in the Ar-$O_2$ plasma spectra are generated from de-excitations of the argon states $3p^5 4p \rightarrow 3p^5 4s$ (wavelength from 415 to 433 nm) and $3p^5 5p \rightarrow 3p^5 4s$ (wavelength from 697 up to 812 nm). Also atomic oxygen lines at 777 and 845 nm are well distinguishable, corresponding to the following de-excitation: $2p^3 3p \rightarrow 2p^3 3s$. Assuming that the electron temperature variations are low at different powers, the light emission of the plasma is mostly dependant on the plasma charge density and the initial concentration of emitting atoms.

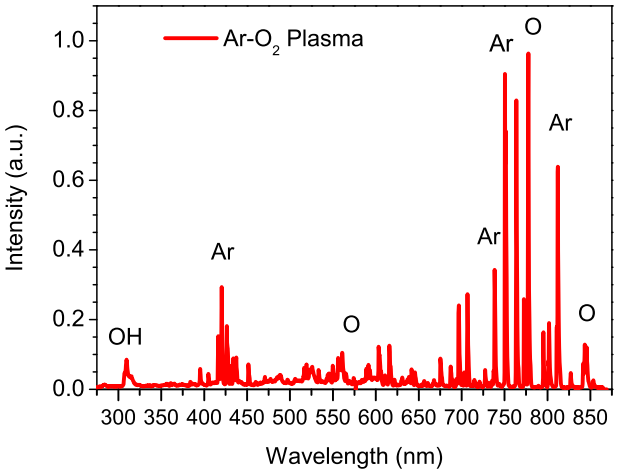


Figure 4.7: Typical OES spectrum measured in the Ar-$O_2$ plasma at 450 W of RF input power.

The E-H mode transition is clearly visible from the observation of emission spectra. When the H-mode is fully established, a steep rise of all emission lines is measured. This is mainly due to the increase of charge density, which is expected to be linear with the power increase [78].

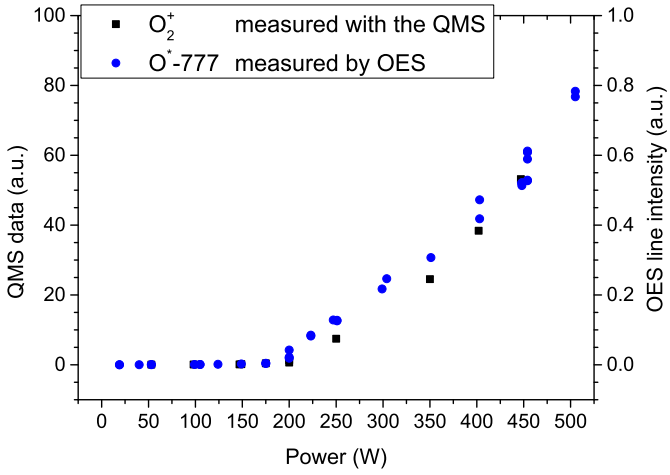


Figure 4.8: When the fully inductive coupling is reached (H-mode) there is a net increases in plasma density, which was measured both with the QMS and by OES.

Figure 4.8 shows on a separated graph the variation of $O_2$ ion flux, measured with the QMS far from the jet at 100 mm, and of radical oxygen line 777 obtained simultaneously from the OES data and proportional to the number of electrons. The increase is similar for both the diagnostics and linear with the power after the transition at 175 W.

This characterization was repeated, monitoring the most intense lines for Ar and O, at different gas concentrations, exploring higher flux regimes (different from those already studied) [6]. The results for two specific lines for argon and oxygen are displayed in the following figures:

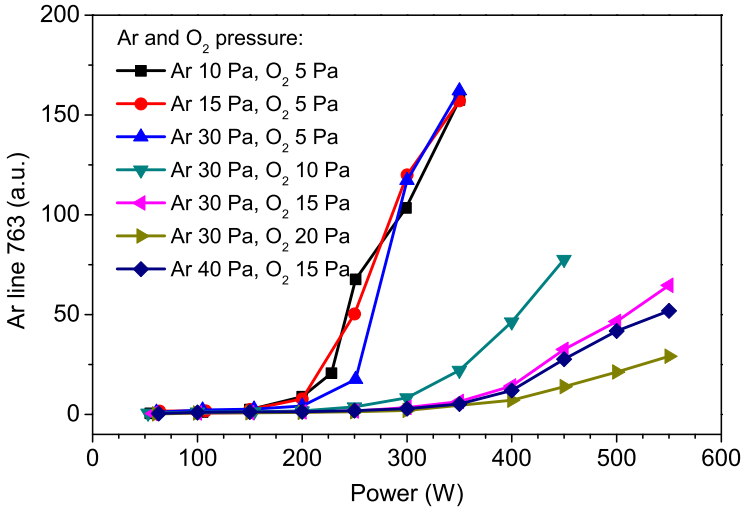


Figure 4.9: Line intensity for the argon line at 763 nm. The signal in counts/sec was dark subtracted and corrected by the optical fiber and instrument wavelength-dependent transmission function and divided by the Ar pressure inside the plasma chamber. In this way the signal is directly related to the charge density and the electron energy. Different experiments are shown with different colors, corresponding to different pressure of argon and oxygen inside the plasma device.

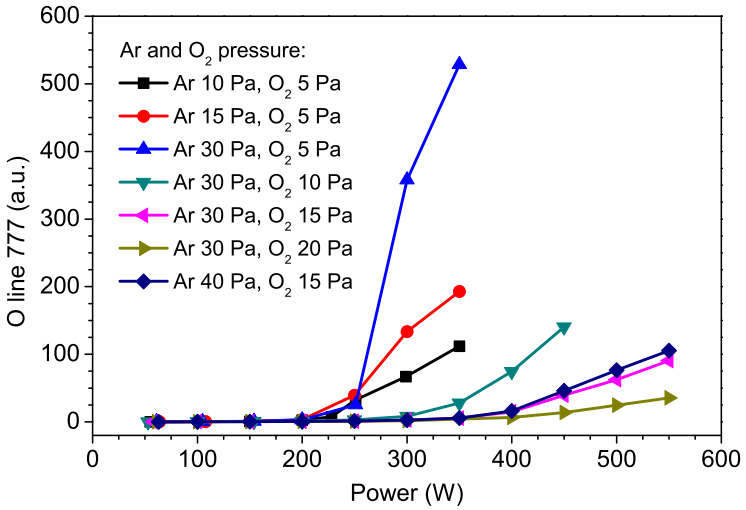


Figure 4.10: Line intensity for the oxygen line at 777 nm. The signal in counts/sec was dark subtracted and corrected by the optical fiber and instrument wavelength-dependent transmission function and divided by the $O_2$ pressure inside the plasma chamber. In this way the signal is directly related to the charge density and the electron energy. Different experiments are shown with different colors, corresponding to different pressure of argon and oxygen inside the plasma device.

The first three experiments listed in Fig.s 4.9 and 4.10, show the trend for Ar and O lines respectively 763 (emitted from the $2p_6$ level, mainly populated from the ground state argon by electron impact), and 777 nm at increasing argon pressure: 10, 15 and 30 Pa of argon, at fixed oxygen pressure of 5 Pa. The transition from E to H mode is again located about 175 W RF power. The measured intensities for the Ar line, normalized by the argon gas pressure to underline the electron contribution, are fairly reproducing the same values, independently on the argon pressure. As already described, the main excitation processes in cold plasma are electron impact collisions. For argon it is possible to write:

$$e^- + Ar \rightarrow Ar^* \rightarrow Ar + \gamma$$

These processes imply that the intensity of an emission line is $I \propto n_{atom} n_e k(T_e)$, thus proportional to the number density of the emitting atoms $n_{atom}$, the electron density $n_e$ and the impact-excitation collision rate functions $k(T_e)$. Dividing this value by the pressure, we cancel the dependency on the atom density. Since the dependency from collision rate functions $k(T_e)$ is very weak, the line intensities shown in Fig. 4.9 are a good approximation of the electron density. Thus argon line 763 shown in Fig. 4.9 suggests that the charge density is not varied by the addition of argon to the plasma.

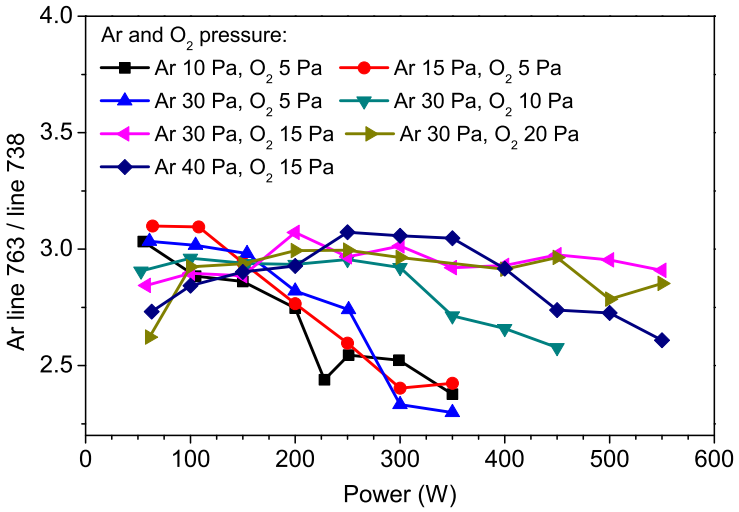


Figure 4.11: Line intensities ratio between argon line 763 and 738 nm. Different experiments are shown with different colors, corresponding to different pressure of argon and oxygen inside the plasma device.

The weak dependency from the collision rate functions $k(T_e)$ is also well justified, as it can be envisaged from Fig. 4.11 where the ratio of two argon lines is shown at the considered experimental conditions. This parameter also cancels the dependency from the charge density $n_e$, thus gives valuable information on the electron impact-excitation collision rate functions $k(T_e)$. The ratio is not undergoing big variations during the different power scans, in particular do not seem to depend on the argon-oxygen pressures, but on the E-H mode of the plasma discharge.
On the contrary the line intensities for O 777 nm shown for the first three experiments listed in Fig. 4.10 (at increasing argon pressure: 10, 15 and 30 Pa of argon, at fixed oxygen pressure of 5 Pa), have an increase, especially for the experiment performed at 30 Pa of argon pressure (blue line). The reaction mechanisms leading to the emission of oxygen atoms are more complicated than those involved in argon emission. Different reactions can be outlined:

- electron impact on molecular oxygen

$$e + O_2 \rightarrow O^* + O \rightarrow O + O + \gamma$$

- electron impact on atomic oxygen

$$e + O \rightarrow O^* \rightarrow O + \gamma$$

- argon impact on molecular oxygen

$$Ar^* + O_2 \rightarrow Ar + O^* + O \rightarrow Ar + O + O + \gamma$$

As we have demonstrated, the considered experimental conditions at the same oxygen pressure values do not exhibit significant differences in the charge density or electron temperature. Thus this variation of the oxygen lines, for increasing argon pressure, is to be ascribed to the different reaction processes leading to the production of radical oxygen. This is a very interesting result, high levels of radical oxygen, required for the dissociation of the precursor, can be achieved increasing the argon pressure. As the molecular oxygen pressure increases, the transition between E-H modes is delayed to higher power levels: 275 W for 10 Pa of $O_2$, 325 W for 15 Pa of $O_2$ and 375 W for 20 Pa. Fully inductive H-mode discharges may require power levels in excess of 500 W, and corresponding voltage levels which continue to rise the larger is oxygen inside the plasma source. This behavior is commonly ascribed to oxygen electronegativity, which favors the formation of negative ions, reducing the electron plasma density. For this reason, it is preferred to maintain high charge densities while reducing the RF power.

These trends are common for almost all the other emission lines of the considered species, however the relative intensities change slightly, as we shown in Fig. 4.11. This reflects shifts in the electron excitation pattern influenced by changes in the electron temperature and the metastable argon abundances. Radiative models have been proposed in order to extract plasma parameters from the relative intensities of the emission line pattern in argon. In particular a simplified model, including only the part of the $2p_x$ system was proposed and modified by us to increase precision. As a results, from the relative intensities of argon emitting lines, it is possible to measure the electron temperature and the concentration of the two kinds of metastable argon atoms. Both measures are valuable in order to characterize the plasma dissociation capability and could also be implemented as a monitor control during the deposition process. The core of the method is to to exploit the different electron energy dependence of the cross section of some of the $2p_x$ excited levels and the large differences in the probability of electron impact excitation of such levels starting from metastable argon atoms. Our proposal was to use the intensities of the whole set of emission lines of the $2p_x$ system to reduce the problem to a Maximum-Likelihood parameter estimation, using the electron impact collision rates available in literature to obtain simultaneously the electron temperature and the population of the argon metastable levels (where the electrons drop de-excitating from the $2p_x$ system).

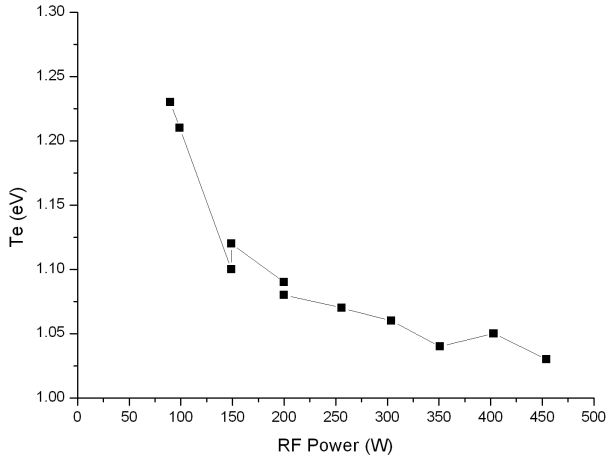


Figure 4.12: Electron temperature estimated by the collisional-radiative model for an Ar-$O_2$ plasma discharge with 3.2 Pa of argon and 4.8 Pa of oxygen. The intensities of the Ar $2p_x$ lines were used to determine these values. As the power increase, the electron temperature decreases.

Figure 4.12 shows the electron temperature estimated by the model, from the measured intensities of the Ar $2p_x$ lines visible in Fig. 4.7. The pressures of the argon and oxygen were respectively 3.2 and 4.8 Pa. The electron temperatures are almost located in the 1 - 1.5 eV range. They are somewhat larger in the E-mode, however never exceeding 2 eV. This temperature is also referred as an excitation temperature, because it relies on the study of the energetic tails of the electron energy distribution (where the electron with energy sufficiently high to excite atoms and molecules can be found).

### 4.4.3 Langmuir probe characterization

A radiofrequency compensated Langmuir probe was inserted in the plasma chamber, from the quartz window (16° to the perpendicular of the left lid) previously used to detect the plasma radiation, in alternative to optical spectroscopy. About 20-50 voltage-current characteristics were averaged and from the final curve common fitting procedure were applied to measure density, electron temperature and plasma potential values of the plasma discharge.
Several limitation were encountered while performing these measurements: first of all the radiofrequency signal at 13.56 MHz was too strong inside the chamber, thus affecting the measured current, especially in the H-mode. The difficulties encountered were mainly in the measurement of the electronic current, so that the ion saturation current was still possible to be measured. From this value a charge density was estimated, using the global electron temperature obtained from OES data in Fig. 4.12. Another issue was that the probe could not be inserted too far inside

the chamber without influencing the plasma inside: performing a voltage scan at 4.8 cm from the left lid (about half of the plasma chamber) results a disruption of the discharge. Most of the measurements were performed at 1.92 cm (corresponding to 2 cm at 16°) from the left lid, at different RF-values for the Ar-$O_2$ discharge.

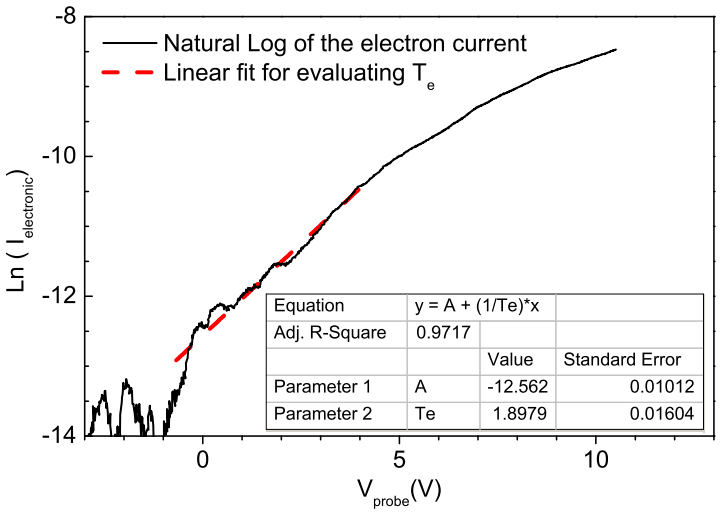


Figure 4.13: Logarithmic Langmuir I-V curve measured inserting the probe by 2 cm at a RF-power of 134 W (E-mode). The ionic current was fitted and subtracted, thus in the graph only the electron current is displayed as a black line. The red line represents a linear fit, whose parameters are shown in the table, used to determine the electron temperature $T_e$.

For reviewing different techniques which can be used to determines plasma parameters from Langmuir probes measurements in RF-plasma, a specific and wide literature can be found [49, 50, 51, 52, 53]. Figure 4.13 shows a detail of a typical Langmuir I-V characteristic curve, subtracted the ion current, thus displaying the electronic contribution to the collected current from which the electron temperature $T_e$ was obtained. Working with a RF-compensated probe, the true $T_e$ is best found from the region where the I - V curve is least affected by radio-frequency; namely, the region on the negative side of floating potential $V_f$ (in most cases $V_f \simeq 5$ V). Hence, it is important to subtract the ion current from the total current accurately. Since k $T_e$ can be obtained from the ion-subtraction region of the electron characteristic, it is not necessary to record the entire I-V curve. This allow to protect the probe from overheating at high electron currents. The electrons can be assumed to have a Maxwellian distribution, especially in then the more collisional, low energy part of their distribution, which corresponds to the part of the curve which was fitted.
Under these assumptions each measured I-V curve was treated as suggested in [64]: first the ionic current was fitted separately, then it was subtracted to determine the temperature and the voltage. The electron temperature was determined as shown in Fig. 4.13, subtracting the ion current and performing a linear fit of the I-V curve

for $V_{probe} < V_f$. From Fig. 4.13 it is possible to observe that the electron saturation part is not straight in log-scale. This is due to the effect of an insufficient RF-compensation which is increasing for increasing probe voltage. The electron temperature obtained in E-mode is slightly consistent with the value of $T_e$ estimated by the OES measurements. In H-mode the probe compensation becomes less effective and the electronic temperature becomes unrealistically high (ranging from 5 to 8 eV). The charge density can then be obtained, knowing the electron temperature and floating potential, by extrapolating the ion saturation current. Due to the problems related to the evaluation of the plasma parameters near the electronic current region (where the RF perturbation is intense), the charge density calculated using the electronic temperature previously obtained by OES model, which are much more reliable, is displayed in Fig. 4.14.

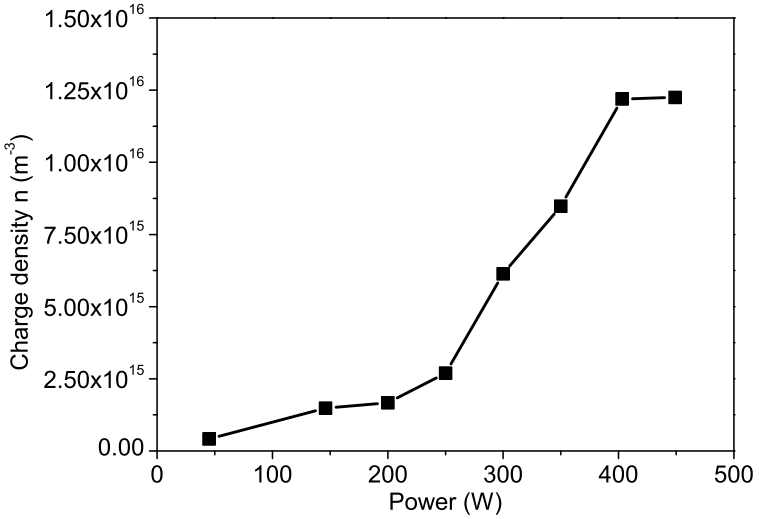


Figure 4.14: Charge density evaluated from the Langmuir probe measurements. As the power increase, the charge density also rise, as already observed during the OES measurements.

The absolute value of this density is indeed underestimating the density inside our plasma discharge. This is due to the use of an excitation temperature obtained from the optical emission spectroscopy model and to the fact that the measurements were taken in a region at about 7 cm from the inductive antenna. However at the considered pressure the plasma is sufficiently well diffused to the location which was scanned with the Langmuir probe. Even if this absolute density is underestimated, its trend plotted against RF-power, shown in Fig. 4.14, is directly related to the ion saturation current correctly measured and to the squared electron temperature, thus weakly dependent from $T_e$. The Debye length can also be evaluated from the first results of the Langmuir curves, generally $\lambda_D \simeq 5 \cdot 10^{-2}$ mm, thus much smaller than the probe radius $r_p = 0.5$ mm. This value was used to estimate a Child-Langmuir sheath thickness of 0.03 mm. Thus the sheath around the probe is very limited.

## 4.5 Experimental: QMS analysis of the supersonic plasma jet

### 4.5.1 Data collection and analysis

The jet characterization performed for neutral gas was repeated for the expanding plasma at similar pressure ratios. As already stated, plasma was generated with a discharge power of 450 W. The QMS was moved along the jet axis of symmetry acquiring ion and neutral mass spectra separately. Also IEDFs were acquired to first study the different ion energy distribution functions. The total area of these distributions can be calculated to obtain an effective total ion flux. However for the measurement of ion mass spectra, a single ion energy was chosen. Ion mass spectra were taken at a fixed energy (8 eV) corresponding to the most energetic ions. Different ion intensities were obtained from the area of the mass peaks, averaged over different mass spectra, as it was done with the neutral gas, giving a signal proportional to the ion flux. The area of the ion peaks shows errors slightly higher than those obtained for the neutral gas. Relative errors are ranging from 1% (along the supersonic jet) to 10% (just after the Mach disk).

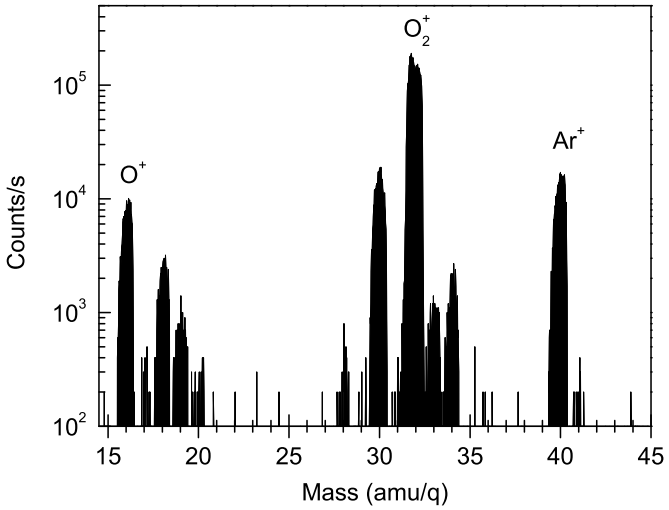


Figure 4.15: Particular of a typical ion mass spectrum measured in Ar-$O_2$ plasma jet before the Mach disk (at the distance of 15 mm from the orifice). The pressure inside the plasma chamber was 8 Pa, the pressure inside the deposition chamber was set to have a pressure ratio before the discharge ignition.

Figure 4.15 shows an example of an ion mass spectrum. It is noteworthy the mass spectra is still dominated by argon and molecular oxygen ions. However the impurities produce minority ions whose signal is not negligible, contrary to neutral spectra. $Ar^+$ and $O_2^+$ signals were measured along the axis for different values of the pressure ratio R. Even if this measurement is highly dependent on the ion species and their energies, some conclusions regarding the ion species in the expanding jet can be

drawn. The molecular oxygen ion flux signal, is more than one order of magnitude greater than the one measured for argon. This high argon reduction is probably related to charge exchange reaction between argon ions and oxygen molecules. It is also possible to observe a rather high ion flux signal for atomic oxygen at M=16 amu/q. Different impurities can also be spotted in the mass spectra. Typical IEDFs of some minor ions found in the jet are who in the Figures below:

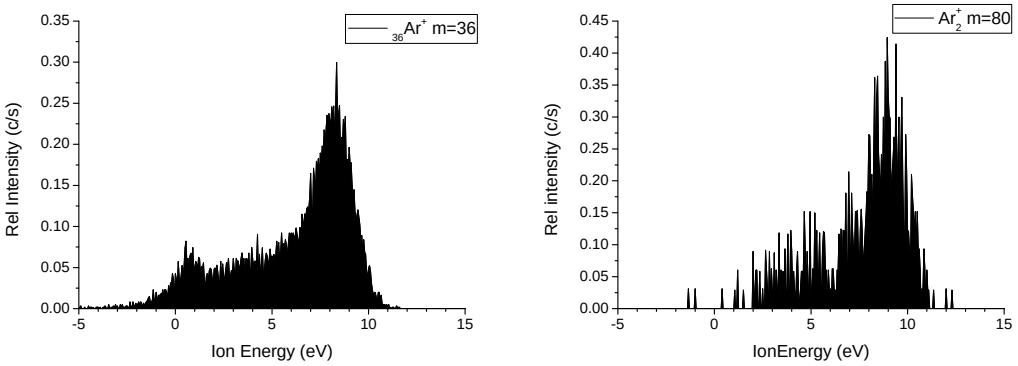


Figure 4.16: $_{36}$Ar ions on the left and $Ar_2^+$ on the right, both distributions have been normalized. These measurements were acquired at a distance from the orifice z=43 mm, during an Ar-$O_2$ plasma discharge at 450 W of RF power at R=28.

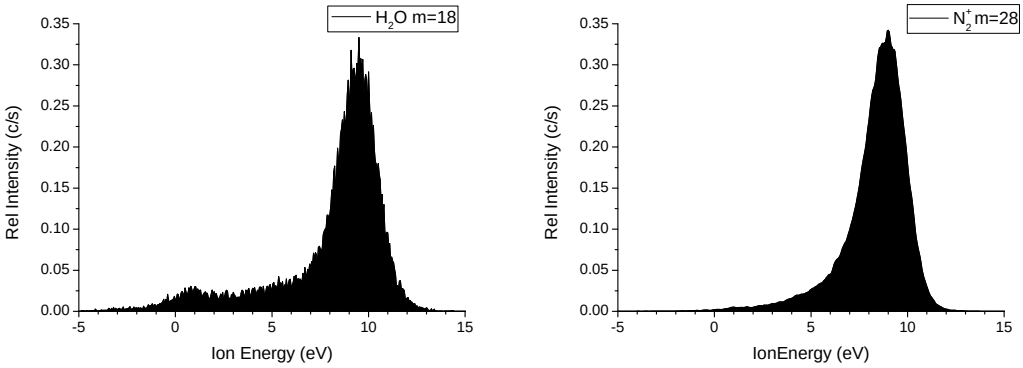


Figure 4.17: $H_2O$ ions on the left and $N_2$ on the right, both distributions have been normalized. These measurements were acquired at a distance from the orifice z=43 mm, during an Ar-$O_2$ plasma discharge at 450 W of RF power at R=28.

The study of these distribution functions gives and useful insight on the reaction inside the plasma chamber, where most of these ions are formed. IEDFs for $Ar^+$ and $O_2^+$ will be shown and discussed later, but their interpretation is somewhat complicated due to the different reactions and collisional processes involved. Ion energy distribution functions measured for minor ion species are less subject to collisional effects. The energy is peaked over the plasma potential and the spread is Maxwellian and related to the ion temperature in the plasma chamber. Collisional processes still slow down some ions creating an energy tail (collisions with neutrals

species are more frequent after the supersonic expansion). These distributions allow us to estimated a plasma potential of about 8 eV, which is the energy used to acquire ion mass spectra. In some of the IEDFs a low energy peak which corresponds to resonant charge exchange is evident. This phenomenon leads to the production of slow argon ions outside the source:

$$X^+_{fast} + Y_{slow} = X_{fast} + Y^+_{slow}$$

This effect is also slightly present in the IEDFs of ${}_{36}Ar^+$ and $ArH^+$.

### 4.5.2 Plasma profiles: mass scans

Figures 4.18 and 4.19 show ion fluxes and neutrals profiles for argon and molecular oxygen (ion mass scans were measured at 8 eV).

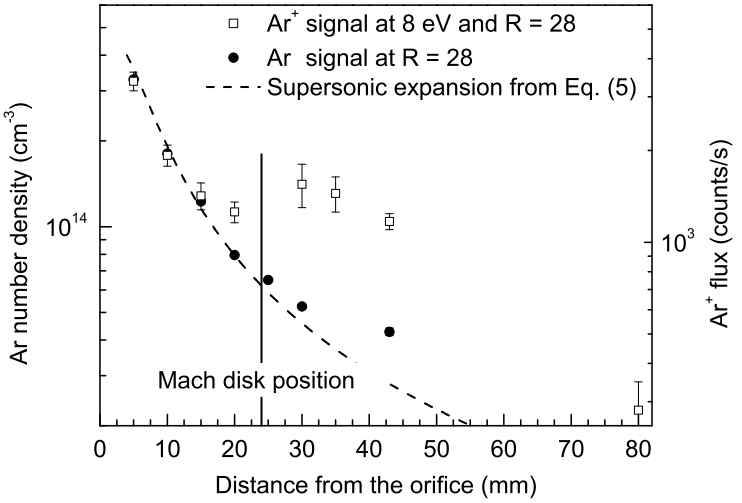


Figure 4.18: Axial profile for argon-oxygen plasma at high pressure ratio. Both ion fluxes (white squares, right axis) and Ar neutral atoms (black circles, left axis) are shown. The pressure inside the plasma chamber was 8 Pa while the pressure inside the deposition chamber was set to have a pressure ratio about 28. RF plasma discharge was inductively coupled and maintained at 450 W. QMS data are reported together with the isentropic expansion law (dashed line). The Mach disk location is indicated by a vertical bar over its position (at about 24 mm from the orifice).

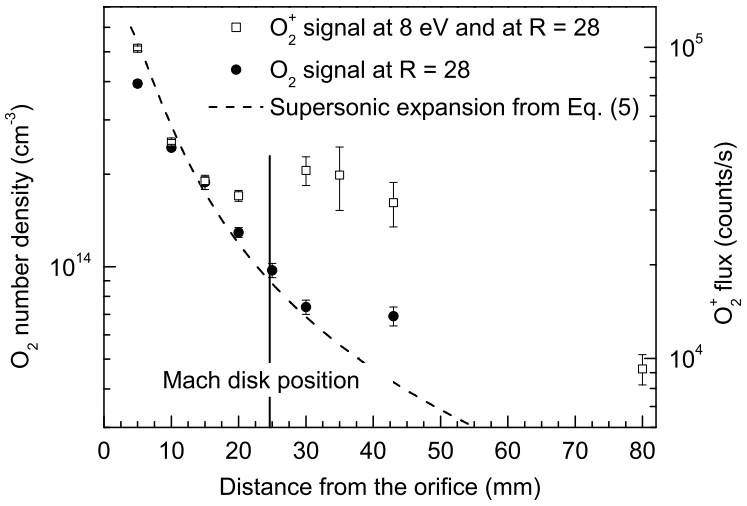


Figure 4.19: Axial profile for argon-oxygen plasma at high pressure ratio. Both ion flux (white squares, right axis) and neutral molecules (black circles, left axis) are shown. The pressure inside the plasma chamber was 8 Pa while the pressure inside the deposition chamber was set to have a pressure ratio about 28. RF plasma discharge was inductively coupled and maintained at 450 W. QMS data are reported together with the isentropic expansion law (dashed line). The Mach disk location is indicated by a vertical bar over its position (at about 24 mm from the orifice).

The neutral gas data is shown as black circles and it is almost unaffected by the plasma: its profile is comparable with those shown in the previous Chapter. Ion flux profiles for 8 eV and denote a decrease comparable with the density inside the gas isentropic expansion (dashed line in Fig. 4.18 and 4.19) inside the supersonic jet with a lesser precision. This is in good agreement with the assumption of an almost adiabatic expansion. Over the Mach disk a significant increase in the ion fluxes can be observed for both and . Here the measurements seem also to fluctuate in subsequent scans giving larger error bars. The increase of the ion flux over the Mach disk can be due to different phenomena, an increase of their density or velocity. Inside the jet electrons are much diffusive than the ion species and can thus leave the supersonic jet in the boundary regions. A significant charge separation could happen in correspondence with the Mach disk forming a positive space charge region and an electric field. It is also to be taken into account that the mass spectrometer can induce an electric perturbation just at the shock front. Far away from the Mach disk, the ion flux decreases due to losses dictated by diffusion and recombination effects. The ratio between the and intensities is constant within the precision of the measurements in the whole profile.

### 4.5.3 Plasma profiles: ion integrated flux

To fully characterize the ions in the jet, also ion energy distribution functions were measured along the jet and inside the enhanced ion flux region. Several scans were

averaged (6 or more, depending on the intensity of the signal) for each different position, generally showing a good reproducibility. The energy spectra can give a better insight on the ion fluxes, especially when collisional phenomena are present, and be integrated to obtain a total ion flux, which takes into account the contribution of ions at different energy. Ion energy distribution functions were measured for and at a fixed mass while reproducing the same experimental condition used for Fig. 4.18 and 4.19.

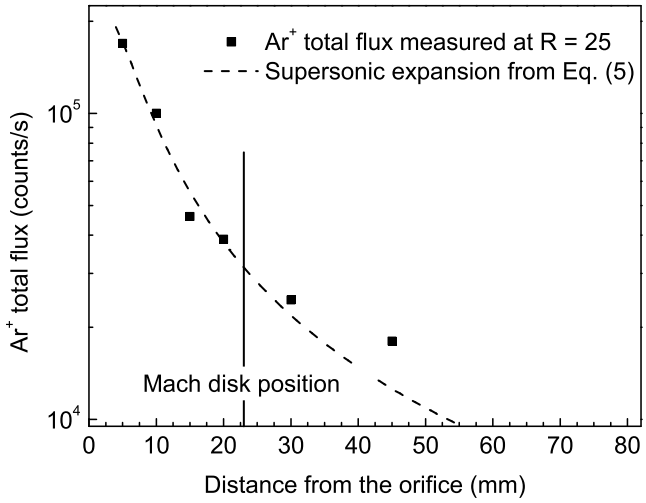


Figure 4.20: Total flux obtained integrating the area of the energy spectra for ions. Measurements were performed at high pressure ratio (R=25, =23 mm). RF plasma discharge was inductively coupled and maintained at 450 W. QMS data are reported together with the isentropic expansion law derived from Eq. (5) (dashed line), here multiplied by a fitting constant. The Mach disk location is indicated by a vertical bar over its position.

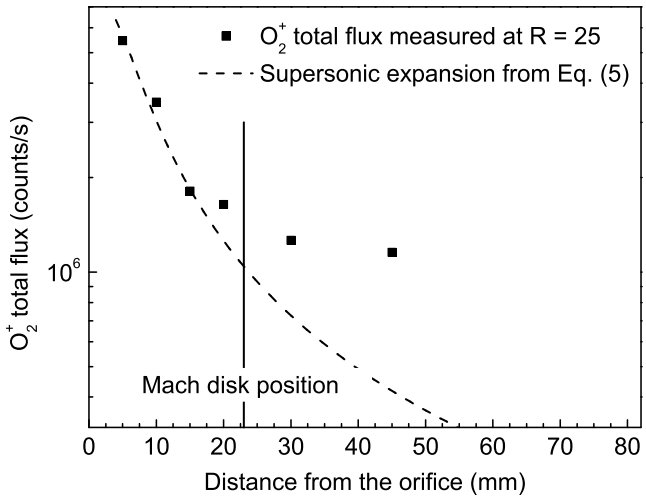


Figure 4.21: Total flux obtained integrating the area of the energy spectra for ions. Measurements were performed at high pressure ratio (R=25, =23 mm). RF plasma discharge was inductively coupled and maintained at 450 W. QMS data are reported together with the isentropic expansion law derived from Eq. (5) (dashed line), here multiplied by a fitting constant. The Mach disk location is indicated by a vertical bar over its position.

The total ion fluxes displayed in Fig. 4.20 and 4.21, respectively for and , were calculated by integrating the whole ion energy spectra. Similarly to the 8 eV flux shown in Fig. 4.18 and 4.19, the total ion flux seems to decrease where the jet is supersonic in fair agreement with the isentropic law (even if we do not expect the flux and the density to correspond each other). The latter is plotted in Fig. 4.20 and 4.21 as a dashed line in order to better compare the spatial behavior of the ions flux with respect to that of the neutral atoms.

### 4.5.4 Plasma profiles: ion energy distribution functions

No local enhancement of the flux could be observed right after the Mach disk location. While the argon ion flux is comparable with the neutral density trend, the molecular oxygen ion fluxes are slightly higher and flatten after the Mach disk instead of getting smaller. The 8 eV flux enhancement over the Mach disk is here covered by the contribution of ions at lower energies, but it can be still observed by directly looking at the energy spectra reported on Fig. 4.22 and 4.23.

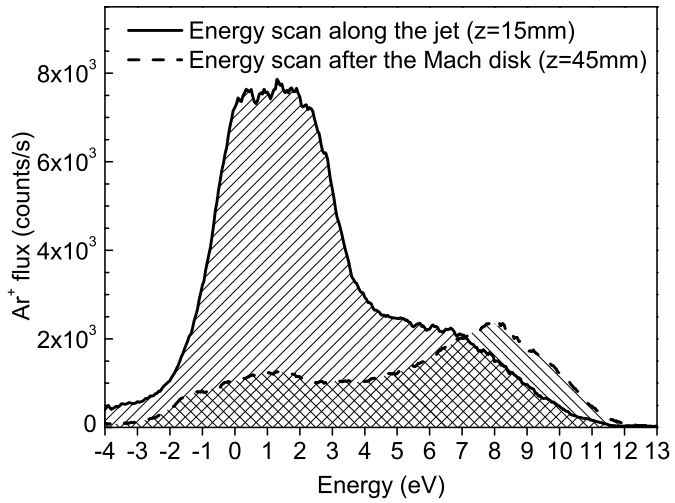


Figure 4.22: Typical energy scans performed for ions at high pressure ratio (R=25, =23 mm) along the expansion. RF plasma discharge was inductively coupled and maintained at 450 W. Two curves are displayed on the same graph, the straight one is located inside the jet (at 15 mm from the orifice) while the dashed curve is located after the Mach disk position (at 45 mm from the orifice).

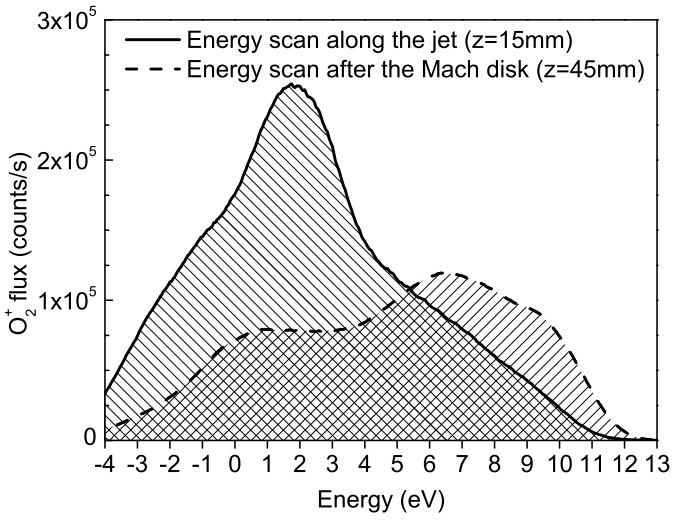


Figure 4.23: Typical energy scans performed for ions at high pressure ratio (R=25, =23 mm) along the expansion. RF plasma discharge was inductively coupled and maintained at 450 W. Two curves are displayed on the same graph, the straight one is located inside the jet (at 15 mm from the orifice) while the dashed curve is located after the Mach disk position (at 45 mm from the orifice).

The interpretation of the ion energy distribution functions is not straightforward. In the presence of a plasma, a sheath always generates between the plasma and the plate. The ions detected by the QMS are accelerated by the sheath electric field whose strength is controlled by the value of the plasma potential in the low-collisional presheath [85, 40]. The energy distribution detected by the mass spectrometer at a

fixed mass represent the energy that ions have while entering the instrument orifice, after being accelerated to a region at grounded potential. Figures 4.22 and 4.23 show two energy scans obtained in the jet and after the Mach disk location. The energy spectra show a wide energy spread for both the two gases in each position studied. In an inductively coupled plasma source the energetic distribution of ions is commonly peaked over a single value. When measuring the distribution of ion species, the latter are accelerated from the plasma toward a grounded detector (the QMS in our case) by a voltage difference equal to the plasma potential. Ions colliding while crossing the sheath will exhibit lower energies. Thus collisional effects can lead to a shift of the ions to the low energetic part of their energy spectrum. These effects are evident in the energy scans shown in Fig.s 4.22 and 4.23, where the energy ranges from 0 up to 12 eV. Some ions at negative energies are also detected, this is a known defect of the instrument due to ions colliding inside the QMS. Ions which collide with neutral gas along the jet by elastic scattering and charge transfer phenomena can fully deplete their kinetic energy. This energy loss is more pronounced for the low energetic ions due to a larger collision cross section [86] and it can be observed in Figures 4.22 and 4.23. The shape of the energy spectra is different for Ar and and it varies with the distance from the orifice. Energy scans performed along the supersonic expansion are dominated by a low energy peak between 1 and 2 eV. After crossing the Mach disk the low energy peak appears flattened and shifting to 0 eV while a high energy peak emerges (as previously observed from the mass scan performed measuring ion fluxes at 8 eV). This suggests that there is a positive potential along the jet which drops to zero after the Mach disk. At the end of the supersonic expansion, the high energy part of the spectra (related to ions arriving directly from the plasma without losing their energy by collisions) could be affected by an electrostatic effect which increases their flux. The low energy part of the spectra (related to ions that have lost most of their energy through collisions) does not seem to be greatly influenced by this effect, due to their lower velocity which makes them collide with a higher probability.

### 4.5.5 IEDFs at different pressure ratios

Varying the pressure in the deposition chamber, the pressure ratio varies changing the position of the Mach disk. The limit to achieve a supersonic expansion is R = 1.89. In the measurements for $Ar^+$ shown in the graphs below, at 43 mm from the nozzle, as R decreases the high energy peak drops while the low energy peak increases. The same phenomenon is visible for $ArH^+$ and $N_2^+$: the number of collision after the shock increases and limit the propagation of ions in the deposition chamber.

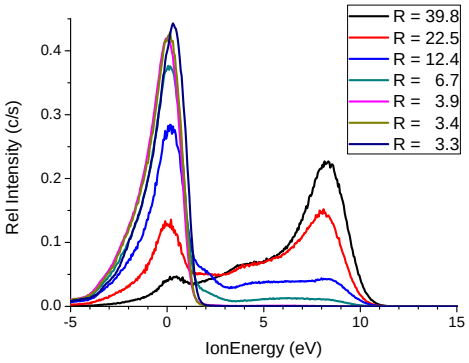


Figure 4.24: Ions scan outside the supersonic region (43 mm from the nozzle).

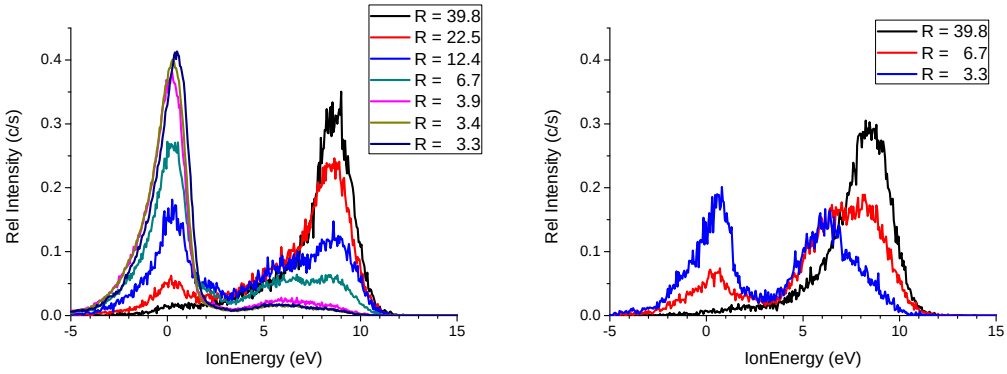


Figure 4.25: Ions scan outside the supersonic region (43 mm from the nozzle) for an argon plasma at 450 W, on the left result for $ArH^+$ on the right $N_2^+$.

The measurements for $O_2^+$ are shown in the graphs below, measured at 25 mm from the nozzle, as R decreases the high energy peak drops while the low energy peak increases. When R is less than the critic value, the jet is not supersonic and the collision leave just a small trace of ions, with a small peak over thermal energy.

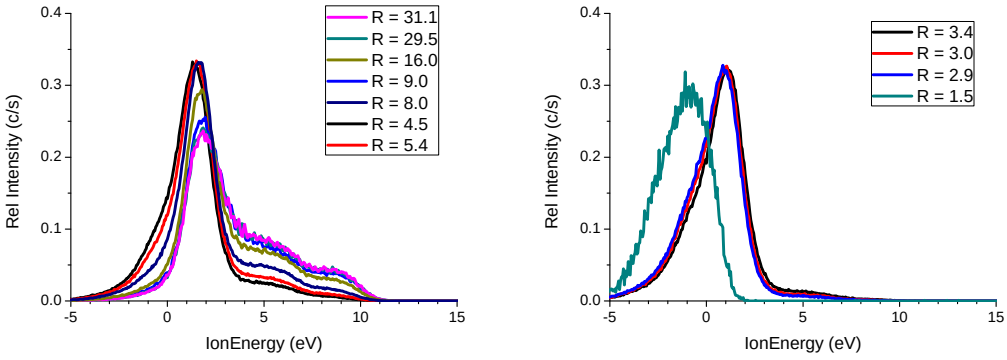


Figure 4.26: $O_2^+$ IED at different pressure ratio.

### 4.5.6 IEDFs at increasing RF-Power

IEDFs were also measured while increasing the RF-Power input, observing the transition from E to H-mode. This analysis was performed fist for pure argon discharge ($P_p$=3.2 Pa, $P_d$=0.11 Pa), then for the Ar-$O_2$ discharge ($P_p$=8 Pa, $P_d$=0.3 Pa). In the first case increasing the RF power supplied to the antenna, the plasma ignite at 20 W in a discharge condition similar to a capacitive plasma source (E-mode), then around 50 W undergoes a transition to a fully inductive discharge (H-mode). The effect on the ion population is mainly on the density which seems to increase linearly with the power until 400 W. In the graph below IED measured for Ar and ArH at Z = 43mm are shown. For $Ar^+$ when the coupling is not fully inductive the energy is mainly quenched and the highest peak is the one at lowest energy. As the power increases the high energy peak (over the plasma potential which seems constant) raises.

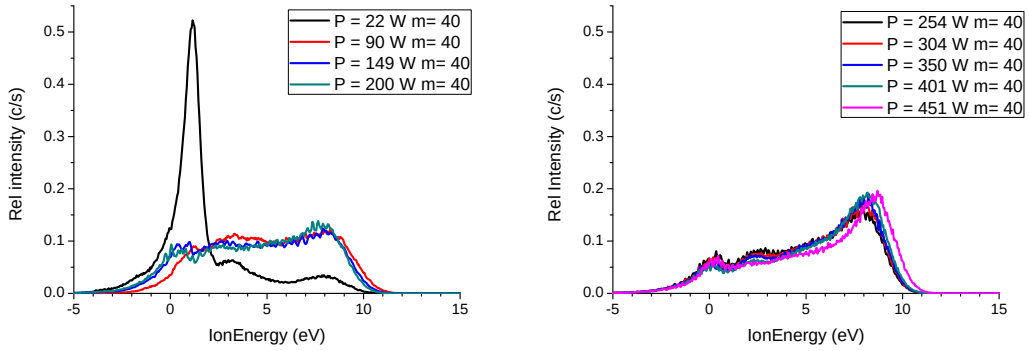


Figure 4.27: Power scan for $Ar^+$ measured at Z = 43 mm.

Looking at the IED measured for $ArH^+$ no particular variation of the shape of the peaks is seen, the high energy peak just slowly raises while increasing the power.

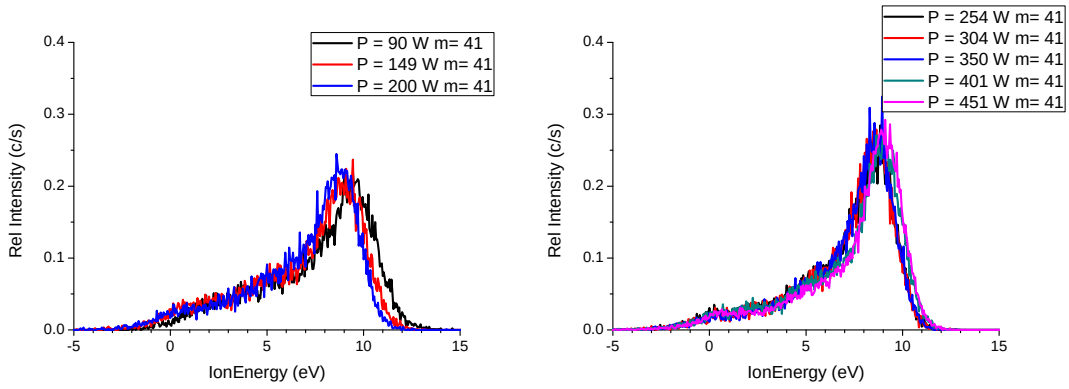


Figure 4.28: Power scan for $ArH^+$ measured at Z = 43 mm.

The following measurements show the IEDFs measured for $O_2^+$ at different power

input, sampled at 25 mm from the nozzle (closer to the nozzle than the data shown before). The transition between the E-mode and the H-mode is about 200 W and as the power increases, three peaks become distinguishable.

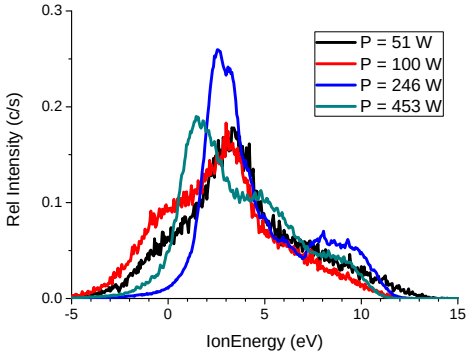


Figure 4.29: Power scan for $O_2^+$ ions measured at 25 mm from the nozzle, about the shock position.

It is very important that the plasma potential (about 8 eV) does not seem to be influenced from the RF-power, at least for the power range considered. However many differences in the shape of the IEDFs can be observed, especially across the

## 4.6 Summary and conclusions

The plasma in the first chamber was directly characterized using different diagnostics. The measurements of time series for voltage and current across the plasma antenna clearly set the E-H mode transition at 175 W and ensure a more efficient power transmission after this power value. Rms voltages of 800 V and currents about 2 A can be observed at 450 W, the RF power level which was chosen for performing PA-SJD deposition.

Optical emission spectroscopy was used to reveal the radiation emitted from the plasma at different pressure values, argon-oxygen concentrations and RF power level. The use of this diagnostic allowed the identification of the main emitting species (Ar and O in this case) from the plasma and denoted a significant increase in charge density after the E-H mode transition. At increasing oxygen in the plasma chamber, this transition is delayed to higher power level, making more complex the establishment of a fully inductive regime. However it was shown that an high production of radical oxygen, required for an effective precursor dissociation, can be achieved also raising the argon pressure in the discharge. A collisional-radiative model for the argon emission lines was successfully employed to estimate the plasma temperature as a function of the RF-power input. The temperature decreases from 1.25 to 1.03 eV as the RF-power is raised from 75 to 450 W in a common argon-oxygen discharge at 8 Pa of total pressure (being oxygen to argon concentrations 3 to 2).

A RF compensated Langmuir probe was introduced inside the plasma chamber to measure the main plasma parameters. Unfortunately the RF-noise on the probe was too high, especially in the H-mode. The measurements of the characteristic Langmuir curve was thus highly perturbed for positive probe potential values. However the ion saturation current could have been extracted from negative part of the Langmuir curve. This value was converted in an approximate density using the electron temperature estimated by OES, giving charge densities increasing from 1 $10^{15}$ to 1 $10^{16}$ $m^{-3}$, as the RF-power was raised from 45 to 450 W.
The QMS was again employed to sample the gas along the jet at different position. During each plasma measurement also ion fluxes and their energy distribution functions were measured. We observed a supersonic jet containing both neutral and positively charged particles. The neutral gas even in the presence of a plasma exhibits a very similar behavior to the gas case. Neutral Ar and $O_2$ expand following the isentropic model without ending shock compression. This proves that the isentropic model is still valid and the expansion is still adiabatic for neutrals even in the presence of a plasma. Supersonic jet ion spectra are dominated by molecular oxygen ions and argon ions. However different peaks can be related to small impurities concentrations. Ion mass and energy spectra gave an insight on the ion fluxes along the jet. Ions along the expansion can be measured with energies ranging from 0 up to 12 eV. The energy spectra of the impurities were observed at a mono-energetic energy distribution peaked about 8 eV. Argon and molecular oxygen ions instead show different energies, due to a more pronounced collisional nature and to charge transfer reactions. Inside the supersonic jet, a very intense low energy peak (about 1 eV for $Ar^+$, 2 eV for $O_2^+$) can be observed in the spectra, along with a moderate high energy section. After the nozzle, inside the supersonic jet, there is an expansion also for the ions, which resemble the isentropic expansion of the neutrals. Across the Mach disk position, the ion energy distribution changes greatly: while the low energy peak reduces itself and shift to 0 eV, the high energetic peak increases. An increase of ion flux could be ascribed to the higher diffusivity of electrons respect to ion species. A positive charge space region could arise in correspondence with the Mach disk. This phenomenon denotes the formation of a space charge region just after the end of the supersonic jet which could originate a potential difference, responsible of enhancing the ion fluxes. This occurs for the highest part of the ion energy spectrum. The presence of high energy fluxes has interesting consequences on ion bombardment processes during the thin film formation and growth. IEDFs were also measured at a fixed position for different pressure ratios, showing the effect of collisions on their energy. The energy distribution functions do not seem to exhibit particular variation in their shape at different RF-powers.

CHAPTER

# 5

# ION DYNAMICS SIMULATIONS

## 5.1 Introduction

The fabrication of thin films having a specific nanostructure represents nowadays a crucial and important research field for its applications such as photovoltaics, photocatalysis and sensor technologies [87, 88]. Different deposition techniques can effectively tailor the properties of a thin film by changing its nanostructure in order to tune the film thickness, porosity, electrical conductivity or optical properties. Among many deposition process, plasma-based techniques are promising due to the low temperatures involved, to the low energy consumption and to the different possibilities offered from their high reactivity [89]. In particular energetic radicals and charged particles are both responsible for etching and for activating surface reactions which can influence the film formation [90, 91]. The study of the collisional processes involved and of the ion energy distribution functions (IEDF) can give precious information to understand their general phenomenology and to control the growth of thin films [37]. Plasma assisted supersonic jet deposition (PA-SJD), is an innovative deposition techniques which combines a reactive plasma with a supersonic jet for the production of nanostructured thin films [6]. An inductively coupled plasma (ICP) source generates a high density argon-oxygen plasma inside a cylindrical vacuum vessel which is connected through a converging nozzle to the deposition chamber, kept at a lower pressure value. As the gas expands in the deposition chamber, a supersonic plasma jet is formed if the pressure ratio upstream and downstream the nozzle is sufficiently high [66]. By adding a metalorganic precursor into the reactive plasma, it is possible to induce dissociation and oxidation reactions which lead to the

formation of metal oxides nanoparticles. The assembled clusters enter the expanding jet where the light gas carrier mixture accelerates different nanoparticles up to the mean fluid speed. Nanoparticles impact on a substrate placed normal to the jet growing a nanostructured thin film. The variation of the plasma properties in the first chamber or of the parameters controlling the supersonic jet can influence both the stoichiometry and structure of the deposition. PA-SJD technique was already employed using an organic precursor of Titanium for $TiO_2$ nanostructured thin film depositions [11].
The presence of a rarefied plasma inside the first chamber and into the jet plays an important role in the deposition process. Energetic ions are formed when they are accelerated by the electric field present in the source and can react forming a population of highly energetic neutral particles. Charged particles are often responsible for the formation of particular nanostructures [92]. Our aim is to characterize the energy of the ions inside the supersonic jet and to understand their collisional effects on the neutral particles. Neglecting the precursor, we studied the Ar plasma itself for its simplicity and focused on the supersonic jet. An experimental analysis was first conducted in an argon plasma using a quadrupole mass spectrometer (QMS) to sample ions an reveal their energy. Starting from these experimental values and the results shown in the previous chapters, we developed a simulation code from first principle studies. Under few assumptions, which are going to be described later on, we simulated the dynamics of ions along the jet to reconstruct their energy distribution functions. The results were compared with the experimental values showing a good agreement and were used to evaluate the ion-neutral collision rate and effects on the global dynamics. This simple case is also ideal for the study of atom-ion collisions inside molecular beams and helped us to calculate $Ar^+$-Ar cross section along the supersonic jet.

## 5.2 Experimental Setup

### 5.2.1 PA-SJD device

The experimental setup is similar to the one shown in the experimental section. An high level of control on the thin films growth can be achieved through the separation the precursor oxidation and the particles acceleration and deposition onto the substrate. It is possible to easily tune the parameters influencing the plasma and the supersonic jet separately by using two different vacuum chambers, connected through a sonic nozzle as shown in Fig. 5.1. In the experimental conditions used in this Chapter the pressures in the plasma and the deposition chambers were set respectively at 3.20 and 0.11 Pa by establishing a constant flow of Ar gas at about 7 sccm.

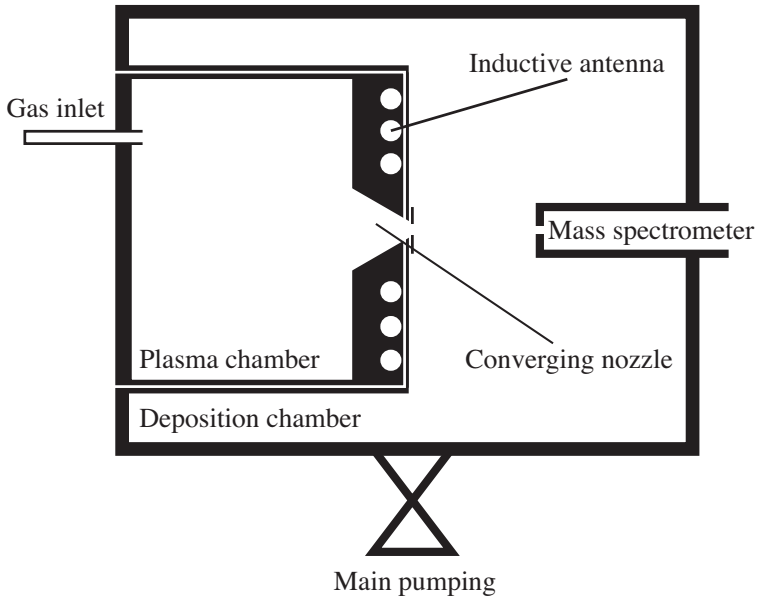


Figure 5.1: Schematic representation of the PA-SJD setup. The plasma chamber and the deposition chamber are shown, connected by the converging nozzle. The mass spectrometer can be moved horizontally inside the deposition chamber.

The plasma is generated in the first chamber using a inductive source [78]. A two and three quarters loop planar antenna (made of copper wire) is placed inside the right side of the first chamber (as shown in Fig. 5.1), shielded by a Teflon scaffold and covered by an alumina disk to reduce sputtering. Feeding the antenna with a 13.56 MHz radiofrequency power generator (Huttinger PFG 1600 RF) at 450 W it is possible to obtain a uniform and stable plasma discharge inside the plasma chamber.

### 5.2.2 Diagnostics

On the right side of the deposition chamber (see Fig. 5.1) there is another vacuum flange which allows the insertion and the movement of a quadrupole mass spectrometer (Hiden EQP-1000 Analyzer [93, 48, 42]). The QMS can collect the gas (and ions) from a small conductance (a 0.1 mm diameter circular orifice placed at the center of a flat circular cap having 50 mm diameter) and it is maintained below $10^{-4}$ Pa by another pumping system (a turbo molecular pump and a rotary pump providing 60 $\ell$/s pumping speed). This instrument was employed in this Chapter mainly for the acquisition of ion fluxes and their energy distribution functions along the supersonic jet [94]. Measurements can be performed at different positions along the main chamber axis with the accuracy of 1 mm. Ions produced outside the instrument enter the 0.1 mm sampling orifice with an initial energy $E_\mathrm{i}$ and they are immediately focused by a lens into the drift space. The instrument is grounded at the chamber reference potential, however an extractor lens can be set to favor the ion acceleration inside the spectrometer. Inside the drift region charged particles are accelerated to an energy equal to $E = E_\mathrm{i} + qV_\mathrm{axis}$, where $V_\mathrm{axis}$ was set to 40 V.

Then a 45° energy filter transmits only ions with a specific desired energy $E$. These ions will then be slowed down to the transit energy required for the mass scan inside the quadrupole and selected by the mass filter. The detector is a secondary electron multiplier pulse-counting detector which can provide mass spectra in counts/sec for mass/charge ratios from 0.4 up to 1000 amu/$q$ (with $q$ in charge units) and energy spectra in counts/sec for energies ranging from -100 to 100 eV. The acquired signal for charged species can be highly dependent on the instrument mass and energy dependent transmission function and the acceptance angle [44, 95]. Anyway the focusing system was carefully tuned in order to reduce energy dependent phenomena such as chromatic aberration or high acceptance angles [46].

## 5.3 Theoretical Background and Model

### 5.3.1 The supersonic jet expansion

Inside the first chamber the gas flow is at continuum flow regime as the mean free path of the gas is much smaller than the typical length scale of the system. The Knudsen number $K_\mathrm{n}$, defined as the ratio between the gas mean free path and the typical system length, can be used to describe the flow regime. High Knudsen numbers ($K_\mathrm{n} \gg 1$), denote a collision-free molecular regime, while for $K_\mathrm{n} \ll 1$ the gas has to be treated using a continuum approximation. There is an intermediate region between the two ($0.1 < K_\mathrm{n} < 1$) where the fluid regime is a transitional. In the experimental conditions used in this Chapter, the pressure is even lower respect to the conditions previously explored. In the first chamber it is possible to evaluate a mean free path of 1.78 mm while the vessel length is of about 100 mm ($K_\mathrm{n} < 0.01$). As the gas flows into the deposition chamber though the sonic nozzle, its fluid regime becomes transitional, as its density decreases (here we evaluate $0.01 < K_\mathrm{n} < 1$).
As gas is left to expand into the lower pressure vessel, a free expansion process takes place [67]. If the pressure difference is high enough, the expansion process can be considered isentropic (i.e. adiabatic and reversible) and a supersonic jet is formed [66]. During this process the gas particles are accelerated to a limit velocity $v_\mathrm{limit}$ forming a low collisional and nearly mono-energetic jet. The gas thermal energy is quickly converted into fluid flow while the temperature decreases. Inside the jet, density and pressure quickly decrease with increasing distance from the nozzle while the Mach number M, defined as the ratio between the gas speed and the local speed of sound, increases. A schematic representation of the geometry of a supersonic jet is sketched in Fig. 5.2. In the continuum regime the expansion ends with a normal shock, called Mach disk, where temperature, pressure and density reach the background values as the gas flow becomes subsonic. In transitional regime the shock becomes much thicker, its length can be assumed comparable with the gas mean free path which in this region is of the order of few centimeters. The properties of this

supersonic beam are mainly determined by the size and shape of the nozzle and by the thermodynamic properties of the gas upstream of the nozzle, in particular they depend on the pressure ratio R [96, 68].

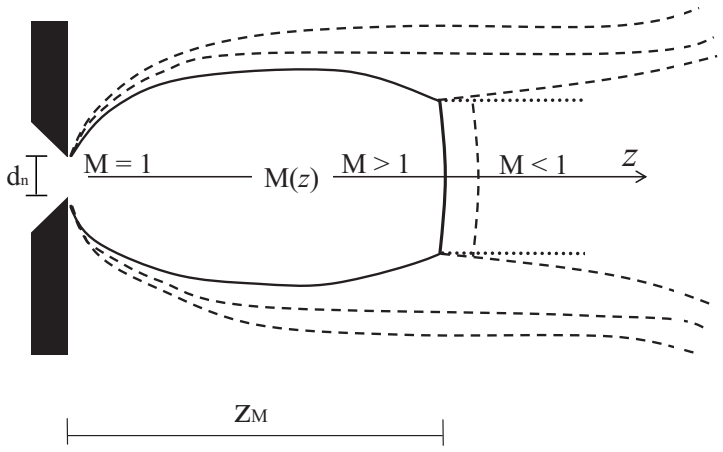


Figure 5.2: Representation of the supersonic expansion geometry formed in the deposition chamber right away from the converging nozzle. The supersonic jet extends up to a distance $z_M$, denoted as the Mach disk, and is limited by the thick lines on the cross section shown. The dashed lines represent non-supersonic streamlines of the gas. The Mach number $M(z)$ depends on the distance $z$ from the nozzle, and becomes $M(z) < 1$ outside the supersonic zone.

The distance of the Mach disk from the nozzle orifice can be calculated using an empirical equation given in [68]:

$$z_M = 0.67 \cdot d_n \sqrt{R} \tag{5.1}$$

where $d_n = 6.9$ mm is the orifice diameter. At this position, dependent from the pressure ratio R, the flow becomes subsonic as the jet ends. The supersonic expansion is widely used as an effective tools for the production of intense molecular beams involved in different applications [27, 97]. In PA-SJD we produce a seeded jet by adding a small mole fraction of titanium oxides nanoparticles to an argon-oxygen supersonic plasma expansion. In this way the properties of the expansion are not much affected by the heavier species added to the jet, while all the particles are accelerated [98]. Thus it is sufficient to study and characterize the light gas carrier component, in order to understand the behavior of a seeded jet. To further simplify the analysis of the system, which employs a binary argon-oxygen mixture for the formation of the jet, in this Chapter we focus on a argon jet to develop a simulation model for the dynamics of ion species. The limit parallel velocity of the gas particles

inside the expansion for a single gas component is given by [66]:

$$v_{\text{limit}} = \sqrt{\frac{2\gamma R T_0}{(\gamma - 1)\text{m}}} \tag{5.2}$$

Where $T_0$ is the temperature inside the plasma chamber, $R$ the perfect gas constant, and $\gamma$ is the gas specific heat ratio. Considering argon at room temperature and at the temperature expected during a plasma discharge we obtain respectively $v_{\text{limit}} = 550$ and 730 m/s. For the gas carrier this limit speed is quickly reached, thus the neutral in the plasma expansion can be roughly assumed to move parallel to the expansion axis at the energy of 0.11 eV. The density along the expansion was measured in our device (see e.g. [41, 42]) showing a good agreement with the relation, obtained thought numerical calculation, for the pressure on a flat plate in a supersonic expansion [70]. Thus the argon density in our expansion can be calculated using:

$$n = \frac{n_0}{\left(a\,(z/\text{d}_\text{n})^2 - b\,(z/\text{d}_\text{n}) + c\right)^{1/\gamma}} \tag{5.3}$$

valid for $z > 0.5 \cdot \text{d}_\text{n}$, where $n_0$ is the density in the plasma chamber, $\gamma = 5/3$, and $a = 1.44$, $b = 0.65$, $c = 0.87$, are numerical constants [70]. In our case, Eq. (5.3) can be used for $z > 3.5$ mm.

### 5.3.2 Ions phenomenology

When an inductive plasma is generated inside the plasma chamber, the properties of the supersonic expansion are affected mainly by the temperature increase. The temperature in the first chamber was evaluated roughly to be approximately 180 °C, constant at 450 W of RF input power [6]. Inside the plasma chamber, ions are produced mainly by electron impact ionization and their initial energy distribution can be assumed to be a Maxwellian function peaked over approximately their thermal energies [37]. As the ions enter the supersonic jet, their trajectories are influenced both by the gas expansion and by electron friction and electric fields [80]. In particular a potential drop is expected between the main chamber and the supersonic expansion region, which can be considered a pre-sheath [40]. This results in a shift of the ion energy distribution functions to an energy comparable with the potential drop [81]. Ions colliding while crossing this sheath will have less total energy providing low-energy tails in the distribution functions [82]. Anyway, as long as the expansion process can be considered adiabatic, the isentropic flow model can be used to describe both the neutral gas and the ion expansion, in the absence of additional electrical phenomena [42, 80]. The neutral gas can be considered partially independent from the charged particles because of the low collision rate and the low charge density in the rarefied plasma. No significant differences could be observed by looking at the neutral density along the supersonic expansion with or without the

plasma [41, 42]. On the contrary ions can interact both with other ions by coulomb scattering and with neutral atoms by elastic scattering or charge transfer reactions. Since the charge density is about two order of magnitude lower than the neutral density, ion-neutral collision are predominant. The interaction between an Ar atom and its singly charged ion form can be described using a potential function similar to a modified 12-4 Lennard-Jones potential [99, 100]. During a scattering process the energy is also influenced by the induced dipole formed on the neutral atom, which can be taken into account by adding a term proportional to $r^{-4}$ [101], where $r$ is the interatomic distance, obtaining:

$$U_{12-4}(r) = \frac{A}{r^{12}} - \frac{B}{r^6} - \frac{C}{r^4} \tag{5.4}$$

where $A$ and $B$ are the Lennard-Jones potential constants for Ar [102, 103] and $C$ is another constant directly related to the atomic dipole polarizability $\alpha$ ($C = \alpha/2$ in atomic units). The term proportional to $r^{-6}$ becomes negligible when induced dipole effect is introduced. Charge transfer reactions are those in which an electron is transferred from one atomic system to another [104]. A collision between a charged species and a neutral one may result in the exchange of an electron, as described by:

$$X^+_{\text{fast}} + Y_{\text{slow}} \rightarrow X_{\text{fast}} + Y^+_{\text{slow}} \tag{5.5}$$

When $X$ and $Y$ are atoms or molecules of the same type, the process is generally elastic and commonly referred to as symmetric resonant [105]. The cross section for resonant charge transfer is large at low collision energies, making it a very common collisional process in low temperature plasma [79, 106].

### 5.3.3 Model

#### Generalities

We aim to simulate IEDFs from first principles by integrating numerically the equations of motion of neutral and charged argon species, Ar and $Ar^+$, respectively, inside the supersonic jet. We use typically an integration step of 0.1 ns. In order to treat the many particle dynamics from the nanoscale to few centimeters of length, we need to resort to some simplifying scheme. We first solve the problem at the nanoscale, thus restricting the calculation to an effective volume within which the interactions take place. This volume has a cylindrical shape where the cross section is sufficiently large as compared to the $Ar^+$-Ar interaction range, but sufficiently small in order to save computing time, i.e. about 10 nm in diameter and 500 $\mu$m in length. The choice of the cylinder length exploits the fact that the ion trajectories remain largely confined around the cylinder axis over long distances as compared to its width. In practical calculations, we neglect the long range ($1/r$) $Ar^+$-$Ar^+$ interactions considering only one $Ar^+$ moving inside the cylinder at a time, which

can be justified due to the rather small density of $Ar^+$ in the jet.
Secondly, we solve the dynamical equations in a frame of reference moving with the mean speed of the neutral species, implying that they are initially at rest and placed at random inside the cylinder. In the latter, the number of neutral Ar is chosen to be consistent with their density in the jet (described by Eq. 5.3), which turns out to be rather small (of about 10 atoms). Upon an interaction with the ion, a neutral atom attains a finite speed, obtained by solving its equation of motion by neglecting the interaction with the remaining neutral atoms. Both energy and momentum are conserved during a scattering process, and we are able to evaluate the ionic kinetic energy at each time-step. In other words, we consider only elastic processes here.
The main axis of the cylinder coincides with the initial direction of the $Ar^+$ velocity (Fig. 5.3a). The ion moves across the cylinder interacting with the neutral species according to the Lennard-Jones type of potential in Eq. (5.4), neglecting the $r^{-6}$ term (Fig. 5.3b). Whenever the ion exits the cylinder, we stop the calculation, attach a new cylinder whose axis is along the exit ion velocity, and restart solving the equations of motion with the new initial conditions (Fig. 5.3c). Each time a new cylinder is considered, new neutral atoms are placed at random positions inside it again at rest.

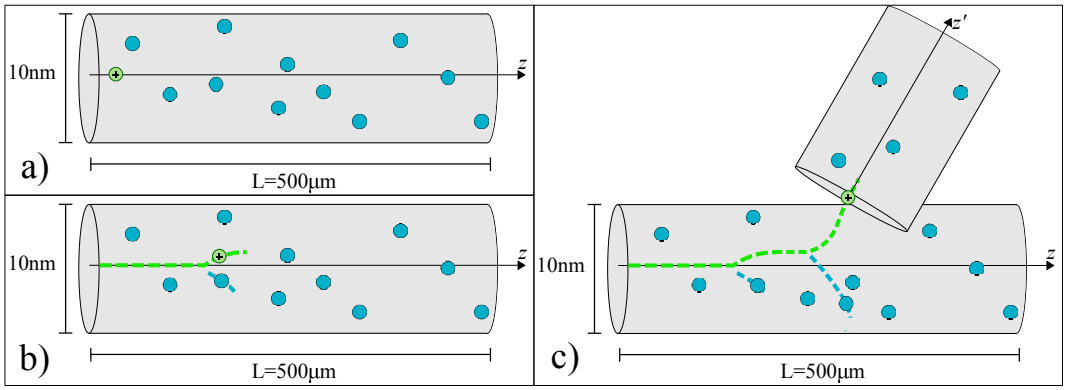


Figure 5.3: Schematic representation of the $Ar^+$ trajectory inside the interaction space (cylinder). The dots represent the neutral Ar atoms, located at random inside the cylinder. (a) Starting cylinder: The ion velocity is assumed to coincide with the $z$-axis (cylinder main axis). (b) Example of the $Ar^+$ ion trajectory inside the cylinder. (c) Example of an $Ar^+$ ion exiting laterally, in which the new orientation axis, $z'$, of the second cylinder coincides with the direction of the exiting ion velocity.

By performing a large number of simulations (generally hundreds) it is possible to obtain final ionic speeds from which we can evaluate the IEDFs for different positions along the supersonic jet axis.
When the ion kinetic energy becomes comparable to that of the neutral species, the simulation is stopped in order to avoid the very time consuming simulations of the whole neutral population. This is consistent with our central assumption that we solve the ions dynamics in the presence of a 'frozen' distribution of neutral atoms in

space. Their contribution to the IEDF at low energies will be treated according to a Gaussian distribution centered at the mean neutral kinetic energy.

### Charge transfer phenomena

The effects of charge transfer phenomena on the IEDFs are relevant when new ions are formed in the sheath or pre-sheath regions of a plasma where ions are more energetic than neutrals. The energy of newly produced ions is equal to the initial energy of the neutral species plus the energy loss by the original ion during the collision. This process results generally in the formation of low energy peaks in the IEDFs [107]. For the plasma considered in this Chapter, this process is reasonably significant, since the cross section for elastic scattering and charge transfer are of the same order of magnitude between 0.1 and 10 eV [79]. Thus we model charge transfer collisions between argon ions and neutral atoms by means of an approximation based on quantum considerations.

The probability of charge transfer, $P_{\mathrm{CT}}$, is a function of distance. Typically, it is possible to establish a cut-off $\mathrm{R_c}$, above which charge transfer does not occur. For distances smaller than $\mathrm{R_c}$, $P_{\mathrm{CT}}$ displays a strong oscillating behavior (see e.g. [104]) varying between zero and one, and described by a sinus square function. The cutoff distance is due to the pure quantum mechanical property of the required overlap of the associated wave-functions of the electronic states, in order to allow for a tunneling process [105]. In a simple scheme, when the ion distance to a neutral atom becomes smaller than $\mathrm{R_c}$, we disregard the oscillations, and assume $P_{\mathrm{CT}}$ to be constant, $P_{\mathrm{CT}} \simeq 1/2$ [101]. From the cross section tabulated in [79], we determine the radius of cutoff for charge transfer, yielding $\mathrm{R_c} = 0.4$ nm. That is, the $P_{\mathrm{CT}}$ probability is just $P = 1/2$ for $r < \mathrm{R_c}$. This can be understood from the fact that the velocity of the ions we are considering is small if compared to the electron velocity. As both species remain closer than $\mathrm{R_c}$, the electron is shared between Ar and $\mathrm{Ar^+}$ and a quasi-molecule is formed. When they get farther apart, the charge transfer cannot occur any more, and the electron is found with the same probability ($P = 1/2$) in either one of them. If the electron remains on the neutral atom, the collision can be considered as a simple elastic scattering event, otherwise it is denoted as a charge transfer event.

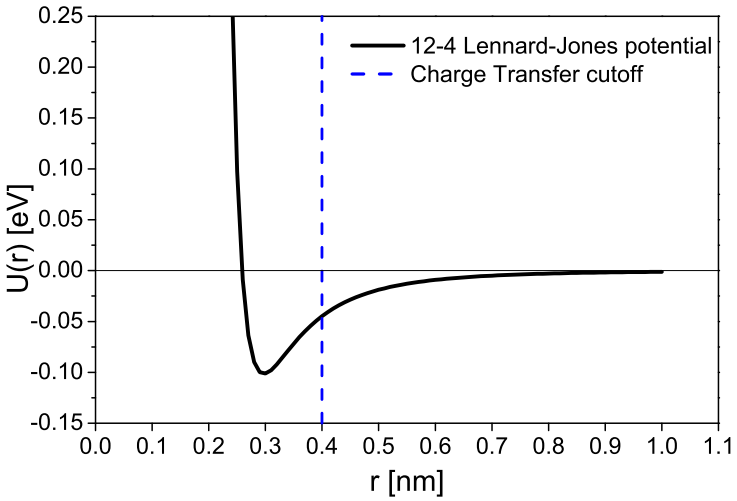


Figure 5.4: The interaction potential $U(r)$ [eV], vs distance $r$ [nm], for $Ar^+$-Ar system used in the simulations. The vertical dashed line indicates the cut-off distance $R_c = 0.4$ nm.

In order to get further insight into the charge transfer process, we report in Fig. 5.4 the interaction potential between the ion and the neutral atom. As on can see, there is a sharp repulsive barrier below $r = 0.25$ nm, suggesting that for such distances the transferred energy from the ion to the atom can be large. In this regime, the charge transfer is expected to take place as described by the simple scheme discussed above. However, for distances close to $R_c$, where the interaction potential is much softer, the energy transfer can be very small and the assumption that the $P_{CT}$ is $P = 1/2$ does not seem accurate. Indeed in our simulations, for distances close to $R_c$, we have found that scattering processes can occur with almost no appreciable energy transfer. To soften the sharp condition at $r = R_c$, we have incorporated a transfer energy dependent factor for the $P_{CT}$. We have assumed that:

$$P_{CT} = \frac{1}{2}\left[1 - \exp\left(-\frac{\Delta E}{E_0}\right)\right], \qquad \text{for } r < R_c \tag{5.6}$$

where $\Delta E$ is the total transfer energy from the ion to the neutral atom in the single scattering process, and $E_0 = 0.1$ eV, corresponding to the minimum $Ar^+$-Ar interaction energy (see Fig. 5.4), and represents a characteristic energy for the process. The PCT in Eq. (5.6) is displayed in Fig. 5.5.

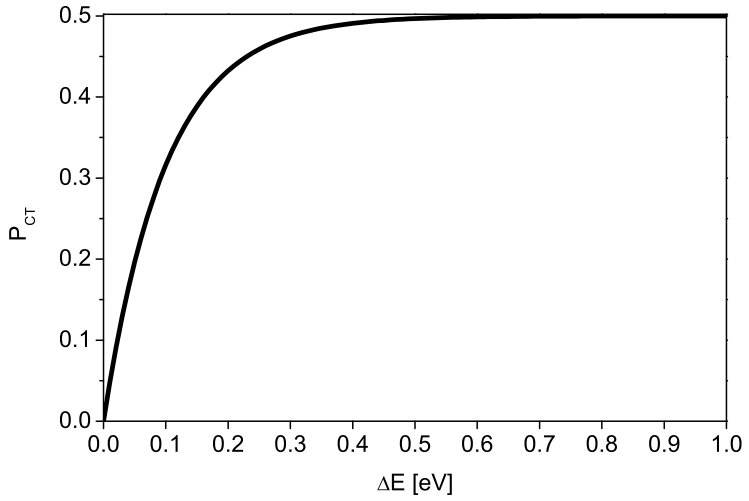


Figure 5.5: Probability $P_{\mathrm{CT}}$ for charge-transfer processes as a function of transfer energy $\Delta E$ [eV] for $Ar^+$-Ar as described by Eq. (5.6).

Notice that this energy-correction factor is important for energies $\Delta E < 0.2$ eV. However, as a result of Eq. (5.6), the number of charge transfer events get reduced, in better agreement with the experimental results as we discuss in the following section.

## 5.4 Experimental Results and Simulations

Experiments were conducted in an argon plasma generated with an inductive coupling. In the presence of the plasma, the pressures in the plasma and deposition chambers were increasing to 4.5 Pa and 0.14 Pa, respectively, obtaining a pressure ratio R = 32 and a corresponding Mach disk distance $z_{\mathrm{M}} = 26$ mm from the nozzle. The RF input power was set at a value of 450 W, corresponding to the working regime for thin film depositions typically used in plasma applications [6, 11]. We then used the QMS to acquire IEDFs at different positions along the jet. In the following, we discuss our results for argon ions.

### 5.4.1 Energy distribution functions: Experiments

In the ICP reactor, where the discharge is purely inductive, ions are produced at a uniform and low plasma potential value (generally below 20 eV) and their energy distribution function exhibits a mono-energetic peak centered below the electron temperature $T_{\mathrm{e}} \sim 1$ eV. Upon crossing a collisionless sheath they gain an energy equal to the potential drop $\Delta V$.
In the following we discuss the results on ion energy distributions in the deposition chamber, both inside and outside the supersonic jet. The measured IEDFs are shown in Figs. 5.6 and 5.7.

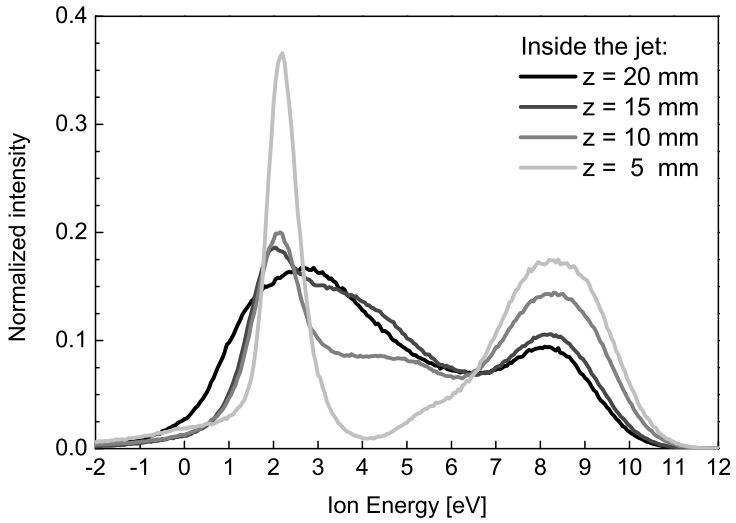


Figure 5.6: Ion energy scans performed with the QMS for $Ar^+$ inside the supersonic jet expansion (at constant pressure ratio: R = 32, corresponding to a Mach disk position: $z_M$ = 26 mm). The RF plasma discharge was inductively coupled and maintained at 450 W. Acquired data have been averaged over few measurements and renormalized to have the same total area equal to 1. The distance from the nozzle $z$ for each curve is shown in the inset.

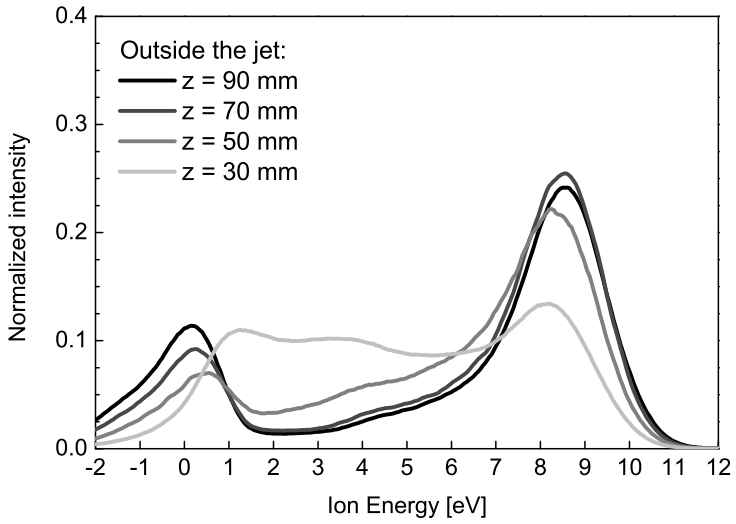


Figure 5.7: Ion energy scans performed with the QMS for $Ar^+$ outside the supersonic jet expansion (at constant pressure ratio: R = 32, corresponding to a Mach disk position: $z_M$ = 26 mm). The RF plasma discharge was inductively coupled and maintained at 450 W. Acquired data have been averaged over few measurements and renormalized to have the same total area equal to 1. The distance from the nozzle $z$ for each curve is shown in the inset.

Two different energy peaks are clearly distinguishable. The higher energy peak, located around 8.3 eV, corresponds to the fast ion population entering the mass spectrometer without undergoing any collisional process and represents the plasma

potential [81]. These ions carry the average maximum energy achievable, and are found at all distances $z$, whose IEDF has a peak height decreasing with increasing $z$. The low energy peak is related to collisional processes, and it is located around 2.2 eV inside the jet and at 0.2 eV outside the Mach disk.

Upon crossing the nozzle, ions enter the low-collisional supersonic expansion and are immediately accelerated by the potential drop between the plasma potential $V_P$ and the potential along the jet, $V_{jet}$ [108]. Inside this region, ions reach the QMS either without colliding, maintaining their total energy, or loose energy due to elastic collisions. Since our QMS is grounded, and its sheath can be considered almost collision-less, the lowest ion energy attainable corresponds to the thermal energy of neutral species, plus the potential energy $V_{jet} \cong 2$ eV. Outside the Mach disk, the low energy peak drops to a lower value, about 0.2 eV, which is comparable to the thermal energy, thus indicating a rapid decrease of the potential in this region, $V_{jet} \cong 0$. The ion collisions with neutral species within the jet yield to a complex redistribution of strength of the IEDFs as a function of energy and position $z$. As one can from the figures, negative energy events are measured which are due to known instrument features [109].

In order to get further insight into the IEDFs, we have performed additional measurements regarding other minor species observed in the ion mass spectra, such as $ArH^+$ [110]. The latter is formed by the reaction of $Ar^+$ with residual water in the plasma chamber. For convenience, we considered the position $z = 43$ mm, far away from the Mach disk. Typical IEDFs measured for $Ar^+$ and $ArH^+$ are compared in Fig. 5.8.

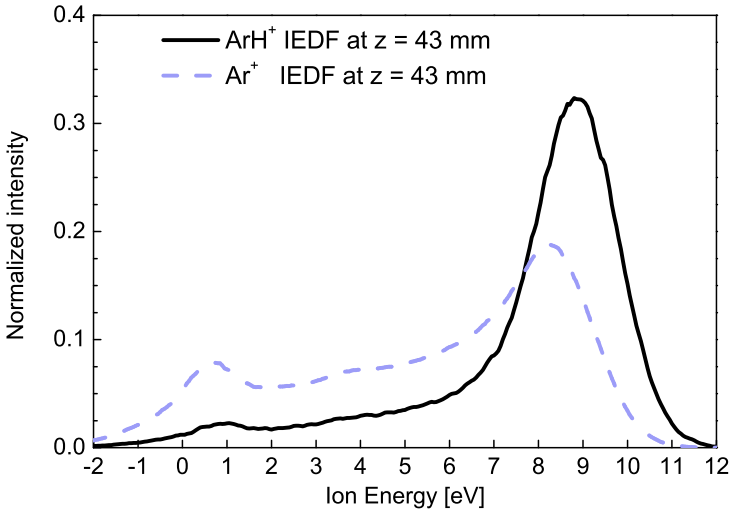


Figure 5.8: Ion energy scans performed with the QMS for $Ar^+$ and $ArH^+$ at $z =$ 43 mm (at constant pressure ratio: R = 32, corresponding to a Mach disk position: $z_M = 26$ mm). The RF plasma discharge was inductively coupled and maintained at 450 W. Acquired data have been averaged over few measurements and renormalized to have the same total area equal to 1.

It can be observed that the low energy peak for $ArH^+$ is much more reduced respect to $Ar^+$. This can be understood by noticing that $ArH^+$ ions do not undergo symmetric resonant charge exchange collisions since their equivalent neutral species do not exist, thus making electron tunneling process very unlikely [111]. According to this picture, we expect that elastic collisions will produce small momentum exchanges, resulting in a reduced energy loss when reaching the spectrometer. This result highlights the importance of charge transfer phenomena for $Ar^+$ in the supersonic plasma jet.

### 5.4.2 Energy distributions: Simulations

Ideally, it is possible to consider as the initial condition for $Ar^+$ at $z = 0$ the kinetic energy $E_{\text{initial}} = E_{\text{peak}} - qV_{\text{jet}}$, with $E_{\text{peak}} \simeq 8$ eV, for ions entering into the deposition chamber [108]. However, the ions undergo scattering processes inside the nozzle, modifying the initial energy $E_{\text{initial}}$. In addition to this complication, we need to know the density of neutral species rather accurately in order to use it in our simulations, which can be estimated using Eq. (5.3), valid for $z \gtrsim 3.5$ mm. Thus, in order to avoid these problems we choose as the initial condition for the energy of $Ar^+$ the corresponding energy distribution measured experimentally at $z = 5$ mm, which is shown in Fig. 5.9a. The latter shows essentially two peaks, one centered around 8 eV, representing those ions which have not undergone large momentum transfer collisions, and a second one around 2 eV, describing low energy 'thermal' ions traveling at speeds comparable to those of the neutral species. To be noted is the lack of existence of ions at intermediate energies.

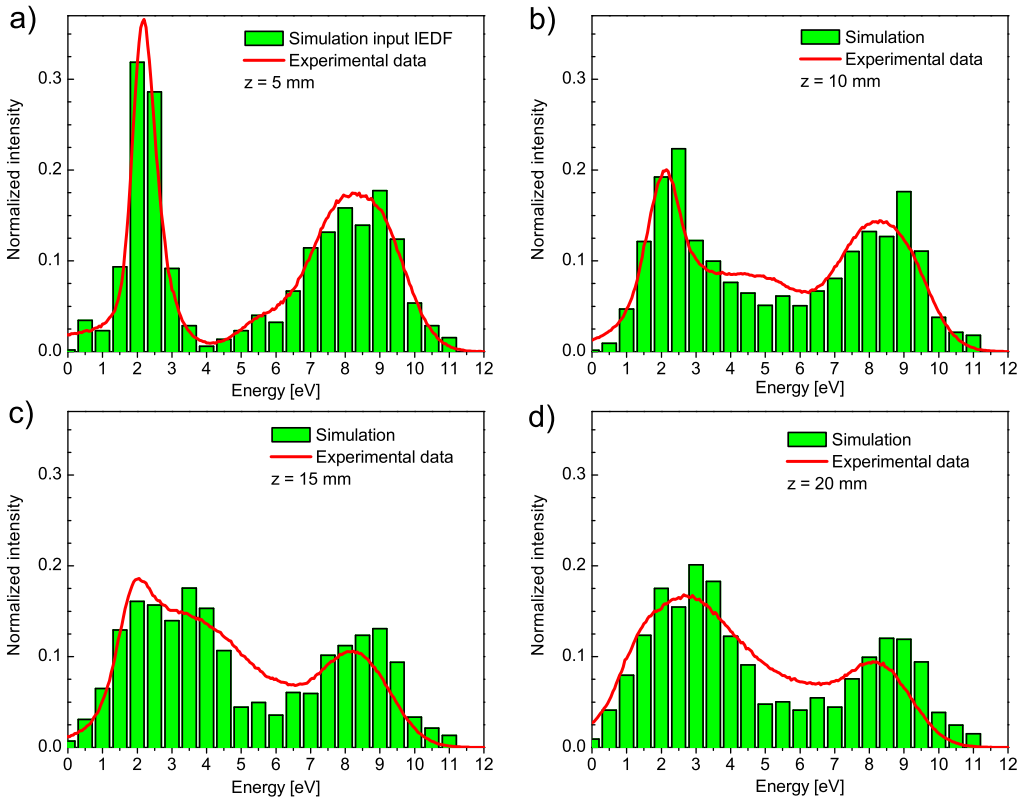


Figure 5.9: Probability distribution functions (IEDF) for $Ar^+$ vs energy [eV] for different positions $z$ obtained according to the model described in Sect. 5.3.3, by simulating the dynamics of about 1000 $Ar^+$ from $z = 5$ mm to $z = 20$ mm. The continuous lines represent the experimental results (see also Fig. 5.6). The results shown in (a) represent the initial distribution function for $Ar^+$ used to start off the simulations obtained in (b-d).

The total energy of an ion at $z = 5$ mm is randomly generated according to the experimental distribution function (Fig. 5.9a). Since we assume the presence of a constant potential along the jet, $V_{\rm jet} \simeq 2$ eV (obtained from the average position of the low energy peak of the experimental IEDFs shown in Fig. 5.6), we have that the total ion energy at $z = 5$ mm is $E_{\rm total} = E_{\rm k} + V_{\rm jet}$, from which we obtain the kinetic energy $E_{\rm k}$ and therefore its initial speed along $z$. Figures 5.9(b-d) show the simulations results (green columns) compared to the experimentally measured IEDFs (red lines).

In order to take into account the fact that the QMS actually measures the ion flux, rather than the ion density [94], we have transformed each single counting event (arrival of an ion at $z$) into an arriving rate, simply by dividing it by the total traveling time elapsed up to the measuring distance $z$. Thus, the simulation results represent the ions per second arriving at the three different positions considered along $z$.

Another feature of the present model to be discussed is how ions are treated when they slow down to kinetic energies $E_{\rm k} < 0.5$ eV. In such cases, ions are assumed to

move at 'thermal' speeds, displaying a dynamics comparable to that of the neutral species. However, as we mentioned in Sect. 5.3.3, we do not treat the dynamics of neutral species unless they undergo a collision with an ion, otherwise the computation of the equations of motion of the whole system would become unmanageable. Therefore, once an ion reaches this lower 'thermal' limit, we stop the simulation, and its contribution to the IEDF is treated separately. Their total number is counted providing a relative weight to a Gaussian distribution function centered around $V_{\text{jet}}$. Their number as a function of $z$ was checked to be consistent with the density expected for neutral species inside the supersonic jet [80], according to Eq. 5.3.
Let us consider first the case $z = 10$ mm as shown in Fig. 5.9b. The simulated IEDF displays an increased population of ions at intermediate energies between 2 and 8 eV in very good agreement with the measured distribution function. Secondly, at larger $z$ values (Fig. 5.9c-d) the model predicts a rather conspicuous change in the shape of the distribution displaying a further increase of ion population between 2 and 4 eV, in good agreement with the experimental results.

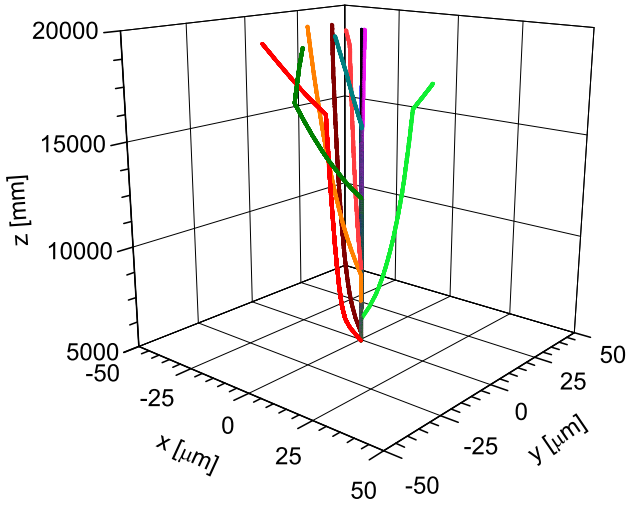


Figure 5.10: Full trajectory over macroscopic lengths (15 mm) simulated for $Ar^+$ in a supersonic jet. The $x$ and $y$ axes are ranging from $-50$ $\mu$m to $+50$ $\mu$m, which is the sampling orifice diameter of the QMS.

Few typical ion trajectories are shown in Fig. 5.10. In what follows, we discuss quantitatively the collision events predicted by the model.

### 5.4.3 Analysis of scattering processes

The IEDFs shown in Fig. 5.9 underline the importance of collisional phenomena inside the plasma jet. In our analysis, a collisional event takes place when there is a energy transfer between an ion and a neutral atom of at least 1 meV. This energy cutoff does not have a physical meaning, but it is just dictated by the need to have a reasonable lower bound for applying the statistical procedure. A collisional event

can be either a simple elastic scattering or a scattering with charge transfer, the latter occurring with a probability described by Eq. 5.6. Both elastic scattering and charge transfer collisions are responsible for the formation of the two-peak IEDFs. We find that for all the ion trajectories simulated, almost every ion experiences a momentum transfer collision, which results in a charge transfer with a probability very close to 50%. About 40% of the ions, at least once, undergoes a charge transfer reaction.

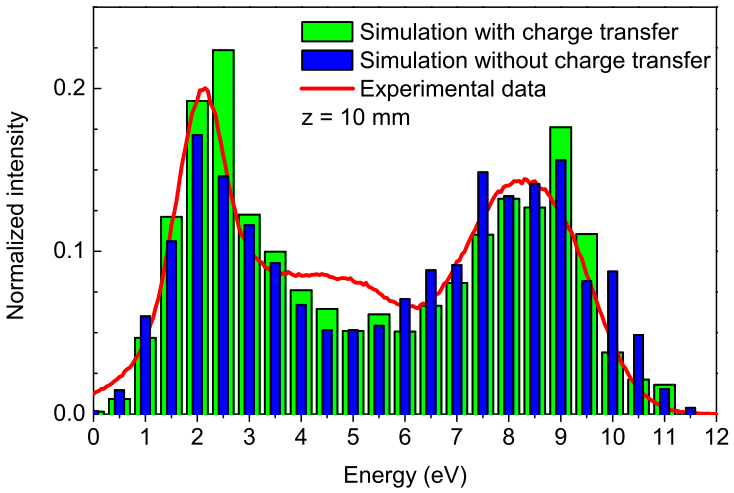


Figure 5.11: Probability distribution function (IEDF) for $Ar^+$ vs energy [eV] at $z = 10$ mm obtained including a charge transfer probability in the model (green vertical bars) and without charge transfer (blue vertical bars). The continuous line represents the experimental results (see also Fig. 5.6).

In order to analyze the global effect of charge transfer, we also performed a simulation of the dynamics of about 1000 ions, from $z = 5$ mm to $z = 10$ mm, setting the probability $P_{CT}$ to zero, thus considering only elastic collisions. The results are shown in Fig. 5.11, where it is possible to compare them with the simulations including charge exchange phenomena. The energy distribution simulated without charge transfer becomes slightly larger than its charge-transfer counterpart for large energies, $E > 6$ eV, while it becomes slightly smaller for low energies, $E < 5$ eV. As it is apparent from Fig. 5.11, charge transfer events seem to provide a better agreement with the experimental data, suggesting that indeed it is important to take them into account.

It is possible to consider also the ion energy loss after each collision, defined as the difference between the final ion (or newly produced ion) energy and the initial ion energy. Ion-neutral collisions clearly result in the formation of a high-energy neutral particles population [112]. The latter can exhibit a wide energy spectra, depending on the ion collisional processes. Considering the simulation results shown in Fig. 5.9, we distinguish between charge transfer and simple elastic scattering

events to evaluate the energy loss along the ions trajectories. This energy loss also corresponds to the energy which is acquired by a single neutral particle and it is shown as a normalized histogram in Fig. 5.12, for both elastic scattering without and with charge exchange reactions.

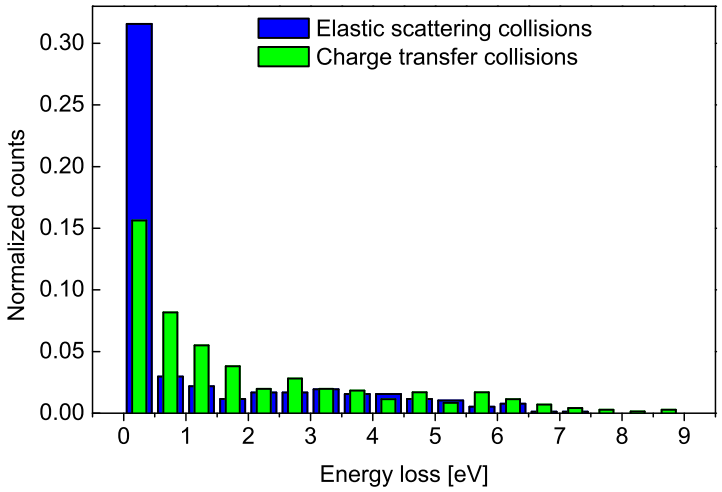


Figure 5.12: Energy loss due to elastic scattering without charge transfer (blue columns), and scattering events when charge transfer occurs (light green columns), in a supersonic jet. These energy distributions can be associated with the energy acquired from the neutral atoms involved in collisions with $Ar^+$.

In general, the energy loss is mostly limited between 0 and 2 eV, however, the two types of collisions are very different. Let us consider first scattering events without charge transfer. As one can see from Fig. 5.12, there occurs a prominent peak at energies $E < 0.5$ eV, suggesting that the majority of elastic scattering events, the impinging ion does not lose much kinetic energy. For charge transfer events, however, this low energy peak decreases substantially, while increasing the probability of higher energy loss events. Interestingly, these low energy events correspond to high energy ions which have lost a large fraction of their kinetic energy and simultaneously have transferred the electron to the newly created ion, carrying a large energy amount. As a result, the difference between the energy of the newly created ion is comparable to the energy of the initial ion.
Another quantity of interest is the mean free path $\lambda$ of ions in the supersonic jet, which can be eventually measured experimentally. In our model, we determine $\lambda$ numerically by evaluating the distance between two collisions along a given ion trajectory. This calculation was performed dividing the space into three adjacent sectors: The first, ranging from $z = 5$ mm to $z = 10$ mm, the second from $z = 10$ mm to $z = 15$ mm and the last one from $z = 15$ mm to $z = 20$ mm. The mean free path was then evaluated in each sector for: Every momentum transfer event (considering both elastic scattering and charge exchange) and for charge transfer collisions only,

for ion energies $E > 0.5$ eV due to the thermalization feature discussed above. In Fig. 5.13 the two different mean free paths are shown as a function of the sector coordinate $z$.

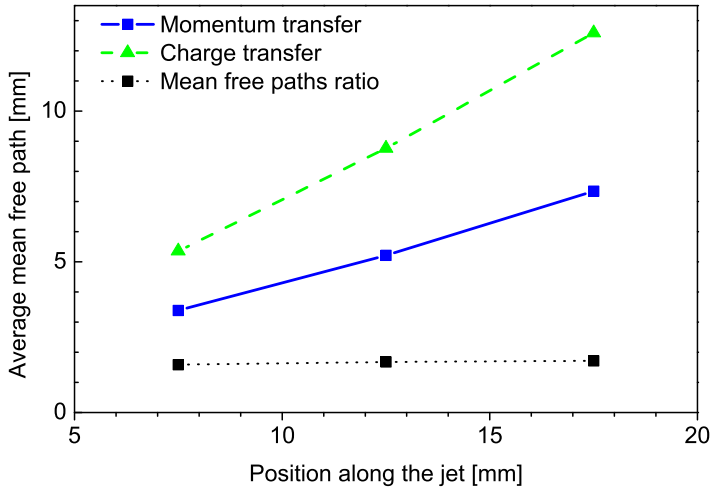


Figure 5.13: $Ar^+$ mean free path between scattering events, $\lambda_s$ (blue straight line), and between scattering events in which there is a charge transfer, $\lambda_c$ (green dashed line). Their ratios, $\lambda_c/\lambda_s \simeq 1.66$, are also shown (black dotted line). The mean free paths are increasing with the distance from the nozzle, as the neutral gas density decreases.

The 25 mm long supersonic jet can be considered nearly collision-less for the neutral atoms at the densities considered in this Chapter, since their mean free paths are of the order of tens of millimeter ($\lambda \in 20, 50$ mm). In contrast, we find that the ion species undergoes collisions in the jet due to the relatively long-range interactions with the neutral species. These results are shown in Fig. 5.13, showing that $\lambda$ increases with $z$, in correspondence with the fact that the target density (Ar neutral atoms) decreases, as one can see from Eq. (5.3). We find that the charge exchange mean free path is about two times larger than that associated with momentum transfer events.
In order to obtain a more general result, the mean free path can be expressed as [66],

$$\lambda = \frac{1}{\sigma n} \tag{5.7}$$

where $\sigma$ represents the cross section [$m^2$] and $n$ the targets number density [$m^{-3}$]. From this well-known relation, we can evaluate a cross section for both momentum and charge transfer phenomena in a supersonic jet. Using the known density for the argon gas, Eq. (5.3), we obtain nearly constant cross section values as a function of $z$, $\sigma_s \simeq (8.3, 9.1, 9.5)\ 10^{-19}$ $m^2$ for the momentum transfer events, and $\sigma_c \simeq (5.3, 5.4, 5.6)\ 10^{-19}$ $m^2$ for charge transfer events. The latter can be averaged yielding mean cross sections values $< \sigma_s > \simeq 9\ 10^{-19}$ $m^2$ and $< \sigma_c > \simeq 5.4\ 10^{-19}$ $m^2$,

respectively.
These cross sections are in very good agreement with the values reported in the literature from beam crossing and drift tube experiments (see e.g. [79],[43]). The values thus obtained for the energy loss (Fig. 5.12) and the cross sections for $Ar^+$-neutral species collisions in a supersonic jet could be employed for estimating $Ar^+$ energy distributions using Monte-Carlo simulations on larger systems. The present results can therefore be very useful in a number of technological applications, such as plasma-assisted supersonic jet deposition processes.

## 5.5 Summary and conclusions

An experimental characterization of ion energy distribution functions was carried out along a low-pressure argon supersonic plasma jet by directly measuring the ion fluxes at different energies with a QMS. The energies observed were distributed up to typically 10 eV and exhibit different distribution functions along the jet expansion axis. In particular, as the gas expands supersonically two peaks are distinguishable around 2 and 8 eV, while outside of the supersonic region (i.e. after about 25 mm from the initial expansion point) the low-energy peak is shifted down to thermal energies ($\simeq 0.1$ eV). These results suggest that the ions energy evolves in a supersonic jet as in a long pre-sheath region. Starting from the plasma at a potential of about 8 eV, each ion can collide inside the jet reducing its energy before being detected by the spectrometer. Along the expanding jet there is a pre-sheath plasma at a nearly constant potential $V_{\rm jet} = 2$ eV. Among different collisional phenomena elastic scattering and charge transfer events are the dominant processes.
Starting from this experimental evidence, we develop and implement a model for the simulation of the ion energy distribution function in a supersonic plasma jet. It is possible to simulate the exact dynamics of one ion at a time, exploiting their very low density, moving along the supersonic jet by integrating the equations of motion from first principles at small time-steps (10 ps). We consider only $Ar^+$-Ar collisions which are described by a 12-4 Lennard-Jones potential, thus including the charge-induced dipole interactions represented by the $r^{-4}$ term. In the proposed model, each momentum transfer collision can result either in a simple elastic scattering process or in a charge transfer event with a well defined probability (close to 1/2 for interaction distances smaller than a cutoff distance, $\sim 0.4$ nm). The dynamics of about 1000 ions was simulated from $z = 5$ mm up to $z = 20$ mm, covering most of the spatial range of the expanding jet.
The agreement between the simulations and the experimental results is very good, thus validating the model assumptions and approximations used. In addition to these features, the phenomenology of the scattering events was further studied by analyzing the energy loss in each collision and calculating the ionic mean free paths also in the presence of charge transfer events. In this way, we can distinguish pro-

cesses in which there is a charge transfer or not. We find that charge transfer collisions occur in nearly 50% of the total number of scattering events. The global effect of charge transfer mechanism on the final distribution functions is found to be quite significant. Indeed, simulations performed without charge exchange reproduce the observed IEDFs only partially, while the inclusion of charge transfers favors medium-low ionic energies in better agreement with experiments. In addition to this, the mean free paths relative to general collision events and those displaying charge transfers can be calculated separately, thus allowing to estimate their respective cross sections, 9 $10^{-19}$ $m^2$ and 5.4 $10^{-19}$ $m^2$, respectively, in very good agreement with estimates known in the literature.

CHAPTER

# 6

# CHARACTERIZATION OF THE SEEDED JET

## 6.1 Introduction

Thin films with a particular surface morphology, structure and grain size exhibit very different electronic, mechanical and optical properties if compared with bulk materials having similar chemical composition. The physical properties of many materials can be greatly enhanced by optimizing the nanoscale assembly process: by modeling the nanoparticles which create and assemble a film it is possible to tailor its properties. To obtain an efficient control on the nanoparticles formation and assembly during the film growth it is required a complex deposition technique based on a bottom-up approach. Few deposition techniques are capable of producing thin films with a desired morphology, although this comes at the price of sacrificing the deposition process versatility and efficiency in terms of surface area, deposition rate and up-scalability.

Plasma have emerged as a very reliable processing medium for synthesis of nanoparticles [113, 114, 115, 116]. The latter are known as the building blocks of nanotechnology. Plasma aided nanosynthesis techniques may be summarized as it follows. The reactants, either as gaseous, liquid or solid, are introduced into the plasma where they are decomposed to their atomic components, which then react chemically to form condensable species as they cool-down while moving downstream. The condensable vapor experiences large supersaturation as the temperature drops rapidly at the edge of the plasma or because of a more rapid but controlled cooling

arranged externally. Fine particles are created in the gas phase by homogeneous nucleation driven by the super-saturation of the vapor. This allows the production of nanoparticles over a wide size distribution, from few nanometers to few hundreds of nanometers. Carrying the plasma and the precursors through a nozzle into a low-pressure environment, it is possible to obtain a specific temperature profile ensuring homogeneous condensation of particles with a narrower size distribution. Supersonic molecular beams have been put to ever-increasing use as a tool of atomic and molecular physics. In particular we have already seen how the supersonic expansion, already described and studied in the previous Chapters, provides a means of preparing a molecular beam with a well-defined kinetic energy. In addition to this, the nearly-total conversion of enthalpy to directed mass flow leads to the extremely low internal temperatures. This allowed in the past years detailed studies of molecular emission spectra which would have been otherwise impossible to investigate and the formation and nucleation of molecules and clusters.

Plasma assisted supersonic jet deposition combines these two technologies for the production of nanoparticles: a reactive plasma and a supersonic jet. An argon-oxygen inductively coupled plasma is employed to create a reactive environment where a titanium metalorganic precursor (titanium isopropoxide) is dissociated and oxidized. The gas is then left to expand from a small orifice into a lower pressure vacuum chamber forming a supersonic jet, where the $TiO_2$ nanoparticles are accelerated onto a substrate by the gas carrier mixture. This deposition technique has proven useful for the deposition of nanostructured thin films having different morphologies at competitive deposition rates [11].

In order to achieve an effective control on the synthesis process, it is fundamental to characterize the expanding plasma jet physics and chemistry and to relate its properties to the films nanostructure and stoichiometry. To fully understand the physical processes involved, it is important to study the nanoparticles, which are the building blocks of the thin films. The aim of this Chapter is to study and analyze the deposition process from the oxidation of the precursor in the plasma chamber to the formation of nanoparticles. By using a quadrupole mass spectrometer (QMS), which was moved along the axis of the supersonic jet where the deposition are performed, we measured neutral and ion species and their energies. Inside the first chamber the plasma and the precursor flow were monitored using optical emission spectroscopy to detect the plasma radiation from a quartz window.

## 6.2 Experimental setup and diagnostics

Figure 6.1 shows a schematic view of the experimental set-up which was used for the measurements in the presence of titanium precursor. The left lid of the plasma chamber also hosts the connection for the gas flow, the precursor and a quartz window inclined at an angle of 16 degrees to the perpendicular.

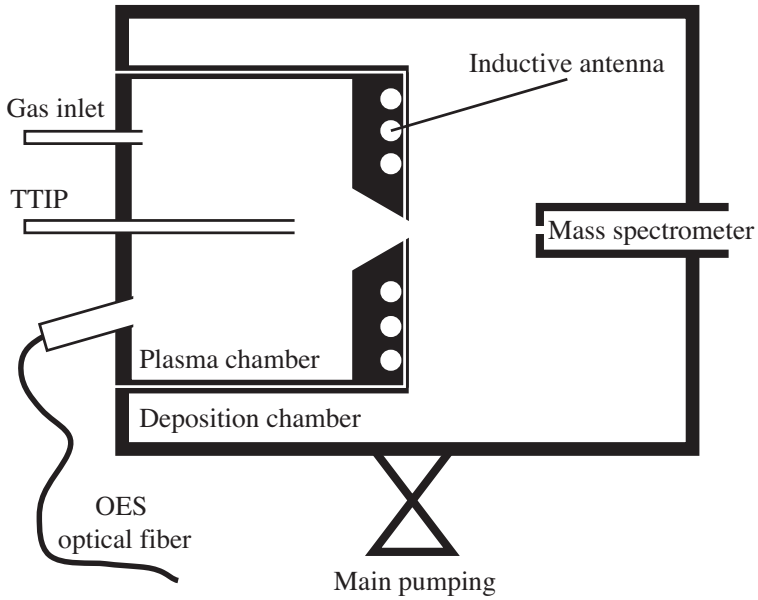


Figure 6.1: Schematic view of the experimental setup. The mass spectrometer sampling orifice can be moved horizontally inside the deposition chamber. OES were acquired from the oblique window (16° to the perpendicular) facing the plasma chamber.

$TiO_2$ films can be obtained from different organic precursors, titanium alkoxide are preferable such as $Ti(OPri)_4$, which already display the $TiO_4$ tetrahedral motif of titanium dioxide lattice in their chemical structure. In this work we chose titanium (IV) Tetraisopropoxide $Ti(OCH(CH_3)_2)_4$ also referred as TTIP, which is liquid at room temperature and it was heated by a power transformer to reach the vapor phase.

Under vacuum conditions its evaporation and diffusion is favored, in particular for temperatures above 38°C its vapor pressure is higher than the gas pressure in the plasma chamber. The conductance between the precursor tank and the chamber can be varied by throttling a micrometer valve. A thermocouple can be inserted in contact with the precursor tank to measure its temperature. Titanium isopropoxide then flows inside a short copper tube, which releases the precursor inside the plasma chamber at 70 mm of distance from the left lid and approximately 25 mm from the nozzle connecting the two chamber. Titanium precursor was injected inside the first chamber when the plasma discharge was sustained at a sufficiently high power level. The temperature was monitored with a thermocouple over the precursor tank and varied to obtain different precursor flows (from 0.25 to 0.75 grams per hour). Operating at temperatures between 40 and 50°C the vapor pressure of TTIP is sufficiently high to create a stable and continuous flow inside the plasma chamber. As the precursor enters the plasma chamber, the plasma becomes bright white, as its emission spectrum becomes more populated. Thus the injection is well distinguishable and also denoted by a small increase of the pressure, which usually rises by 1

Pa.
Optical emission spectroscopy (OES) is a well know non-intrusive diagnostics which has already been applied in many plasma discharges. Revealing the light emitted from atoms, molecules and ions which are excited from free electrons in the discharge, it is possible to understand the main reaction processes in the plasma. The intensity of emission lines can identify chemical species and allows to gain insight about their abundances. From the quartz window facing the plasma chamber optical emission spectra (OES) were acquired using two different low resolution spectrometers, as already described previously, to monitor the entrance and the dissociation of the precursor.
Quadruple mass spectrometers represent an in situ, real time sensing diagnostic used to perform residual gas analysis of gas and reactive plasma. A QMS (Hiden EQP-1000 Analyzer), movable across a vacuum flange, was used here to acquire mass spectra along the axis of symmetry of the main vacuum vessel (300 mm scan from outside the right lid to the nozzle connecting the two chambers) detecting the $TiO_x$ seeds.

## 6.3 Nanoparticles phenomenology

### 6.3.1 Precursor dissociation

The precursor monomer is injected inside the plasma chamber through a copper tube. Here, before entering the supersonic jet in the deposition chamber, it is dissociated by three main phenomena:

- Thermal decomposition
- Electron impact
- Oxidation and other chemical reactions

From the average flow rate evaluated for the TTIP, it follows that it is injected at a flow velocity which can be estimated about 0.05 m/s. This velocity is smaller than the diffusion time which can be evaluated for an organic monomer (of the order a 0.5 m/s), thus the precursor is free to diffuse inside the plasma chamber and be dissociated. However it is reasonable that a significant part of the precursor flowing into the plasma chamber may directly enter the converging nozzle after moving straight from the tube for 25 mm and thus being only partly dissociated.

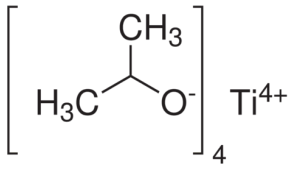


Figure 6.2: Chemical formula of the Titanium Isopropoxide, the metalorganic precursor used for $TiO_2$ depositions.

The thermal dissociation of titanium isopropoxide takes place after 350°C, which is well above the temperatures which were measured inside the plasma chamber (180°C at 450 W RF-power). Thus this process can be considered mostly negligible in dissociating the precursor.
Electron impact is a relevant phenomena inside the plasma. Energetic electrons can dissociate the precursor molecules, contributing to the cleavage of chemical bounds. In particular the $CH_x$ groups of the precursor are efficiently removed by the electrons. During optical emission spectroscopy measurements of a pure Ar plasma (thus in the absence of oxidation reactions) it was observed a remarkable presence of emitting $CH_x$ molecules. It is difficult to estimate the effect of electron impact collisions for this complex case, however previously the collision rates were estimated to be of the order of $10^{-16}$ $m^3/s$. Oxidation is the most important reaction process for the precursor dissociation. This is evident from the analysis of depositions and the QMS measurements: the more oxygen radical produced, the higher will be the film purity and the precursor dissociation, otherwise many C and CH groups can be found in high concentrations on the thin film and along the expanding jet.

### 6.3.2 Supersonic seeded jets

The addition of a small mole fraction of a second species to the gas producing a supersonic expansion, results in the formation of a seeded molecular beam, whose physics is nearly the same as that for a pure expanding gas jet, with molecular weight and heath capacity taken as the weighted average of the gas making up the mixture [57]. Ideally both component gases reach the same flow velocity and temperature. For a gas mixture consisting of a low concentration of a heavy seed gas in a light carrier gas, the limiting flow velocity is dominated by the more abundant lighter gas, thus it becomes possible to accelerate the seed gas to high kinetic energies. The latter are very well defined, thanks to the narrowing of the velocity distribution.
At low to intermediate source densities, the heavier gas molecules tend to lag behind the lighter gas carrier particles. During the expansion process, the heavier molecules are repetitively bombarded by the lighter gas molecules and are slowly accelerated to the full beam velocity. If the total source pressure is too low, however, less than a complete acceleration is achieved, leading to velocity slip phenomena. This particular situation has been extensively investigated both experimentally [117, 118]

and theoretically and applies to our experimental conditions. A simple model of seeded supersonic beams has been presented, which provides useful expression for the terminal temperatures, velocity slip, enrichment factor [119]. In particular the axial enrichment expected for the heavy species, is expected to be much higher than what was previously seen for the argon and oxygen gas mixtures, as it scales with the root square of the masses [120]. Multiple collisions with the lighter carrier gas during the supersonic expansion tend to accelerated the component of velocity along the jet axis, but are less effective in modifying the perpendicular component of velocity. As a result, the initial trajectories of the heavy particles are bent toward the jet axis, leading to an increase in concentration of these heavier species in the axis centerline. A theoretical analysis of this phenomenon has been proposed and confirmed experimentally [121, 122].

The primary advantages of seeded beams are that they allow the seed gas to be accelerated to the beam velocity of the carrier gas, and also allow the internal degrees of freedom of the seed gas to be cooled substantially. In this environment, molecules may nucleate forming weakly-bound clusters species. The production of clusters in a supersonic expansion allows a simplified study of the initial steps in nucleation since the collisional processes in the jet are well understood.

In a supersonic jet, the condensation of monomers to form clusters requires three-body collisions, in which the third body carries off the energy. However if the monomers are well diluted in a higher dense light gas carrier, also two-body collisions may contribute followed by a collision with the gas carrier. This process takes place in 2-step:

$$A + A \rightarrow A_2^*$$

first an excited dimer is formed

$$A_2^* + B \rightarrow A_2 + B^*$$

then its energy is given to the third monomer. In a supersonic expansion the total number of binary collision is proportional to $p_0 d_n$, where $p_0$ is pressure of the gas in the reservoir chamber (monomers in the plasma chamber) and $d_n$ the nozzle diameter. The total number of three-body collisions instead is proportional to $p_0^2 d_n$, however the mass throughput through the nozzle is scaling with $p_0 d_n^2$. This implies that the nucleation can be favored, also maintaining a given gas throughput, by increasing the reservoir pressure and slightly reducing the nozzle diameter. For this reason three-body collisions become more frequent using a slit nozzle geometry. Using this kind of nozzle the density drops linearly with increasing distance from the source, thus greatly enhancing three body collisions and the formation of clusters.

Starting from dimers, bigger clusters can be formed as the temperature of the supersonic jet decreases. Several models can be designed for the prediction of the nucleation and aggregation of clusters, however the variables are numerous and for

the purposes of this study it is sufficient to underline the main influencing parameters [123]. The classical condensation theory can still be very useful to describe the formation of clusters. It offers the advantage of including very few parameters, derived from basic concepts, however it has certain limitations. Classical theory assumes that the properties of a cluster (assumed to be a liquid) can be derived by extrapolating those of the corresponding bulk liquid, independently of the number of atoms n that it may contain: the calculation of the minimum work of formation of a cluster from a metastable phase yields the partition of the free energy. This theory is based on the growth mechanism of monomer addition which assumes a very small density of clusters and an infinite supply of monomers.

$$A + A_n \leftrightarrows A_{n+1}$$

This reaction is valid in both directions, due to the effects of molecular evaporation from the cluster, which arise at increasing cluster dimensions. A more effective generalization of the theory to more complicated growth processes can be made, when agglomeration between clusters is allowed.
This classical theory cannot be applied efficiently to supersonic seeded jets because of variation of density and temperature. Thus classical nucleation models are inadequate to describe clustering in free-jet expansions. Anyway it is still possible to determine some relations which take into account the changes in the kinetic conditions for the cluster formation, as a function of $p_0$, $T_0$, and $d_n$ [124, 125]. From the development of these aspects one can obtain an insight into clustering in a supersonic expansion with quite realistic predictions of the characteristics of the beam.
Weiel proposed a model for seeded beams with highly diluted vapors, which can be adopted to describe the evolution of clusters inside a supersonic expansion [126]. This model allows the calculation of an upper limit to the cluster size achievable at given source conditions and for a given vapor. Some simple assumptions are to be made: every collision (between monomers, monomers and the cluster and between two clusters) is effective in forming a new cluster, the heat of condensation released by the cluster growth is efficiently carried away by the collisions with the carrier gas (very high dilution). From the calculation of the collision rate in an isentropic expansion and considering a monatomic carrier gas, Weiel obtained the following relationship model to evaluate the nucleation rate of cluster along the axis of symmetry of an expanding supersonic jet:

$$\frac{dN}{dz^*} = 4 \cdot d_1^2 \cdot ln(2) \cdot n_1 0 \left(\frac{2\pi m_{gas}}{5m_1}\right)^{1/2} \cdot \left(1 + \frac{M^2(z^*)}{3}\right)^{-3/2} \cdot \frac{N^{1/6}(z^*)}{M(z^*)} \qquad (6.1)$$

where $z^*$ is the ratio between the axial position and the nozzle diameter, $d_1$ is the monomer diameter, $n_1(z^*)$ the monomer number density at the position $z^*$ along the expansion axis, $m_1$ the monomer molar mass and $M(z^*)$ the Mach number along

the centerline of the expansion.
If one assumes that at the nozzle throat there is no condensation $N(0) = 1$ (only monomers are present at the beginning of the expansion), 6.1 may be easily solved numerically, by using the relation for the Mach number along the centerline of the supersonic expansion:

$$M(z^*) = A\,(z^* - z_1)^{\gamma-1} - \frac{1}{2}\left(\frac{\gamma+1}{\gamma-1}\right) / \left(A\,(z^* - z_1)^{\gamma-1}\right) + C\,(z^* - z_1)^{-3(\gamma-1)} \quad (6.2)$$

Figure 6.3 displays the results of the numerical calculation of the $TiO_2$ maximum cluster dimension, using the model proposed by Weiel.

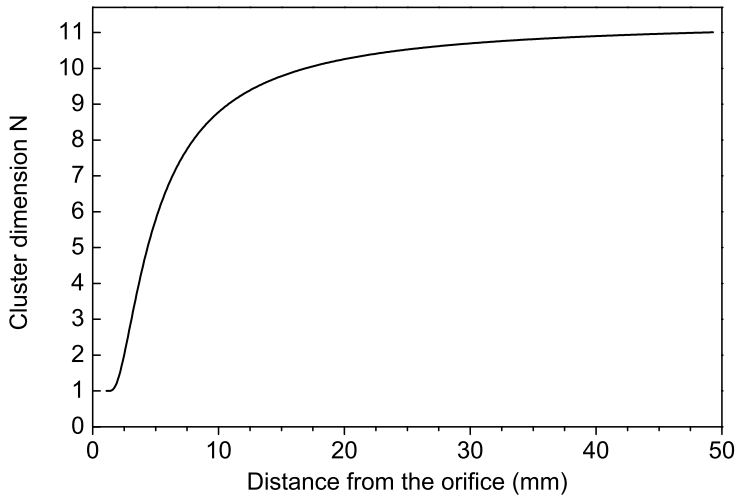


Figure 6.3: Maximum cluster dimension along the supersonic expansion plotted against the distance from the orifice $z$. As the Mach number (inversely proportional to the gas temperature) increases, the nucleation is favored. Contrary to this effect, the density decreases along the expanding jet, thus a maximum cluster dimension is quickly reached between 10 and 20 mm from the nozzle.

This calculation was performed considering a $TiO_2$ effective molecular radius of 0.8 nm (obtained as the cube root $M/\rho$, $M$ being the atomic mass, $\rho$ the bulk density). The precursor density was estimated from the analyses of the precursor consumption during each deposition, the pressure increase during its injection and a relative estimation from the QMS data. From the evaluation shown in Fig. 6.3, one can estimate an average size of 9-10 molecules per cluster if the depositions are made between 10 and 20 mm of distance from the orifice. The Mach number is inversely proportional to the gas temperature (perpendicular temperature), thus its increase along the supersonic expansion results in a decrease of the temperature, favoring the nucleation and growth of clusters. On the other side, as the jet expands its density decreases and the law provided by Weiel show an asymptotic behavior after a short distance from the nozzle (about 10 mm). What is more important for our purposes, is that this model implies that the size of the clusters is influenced by the density of

the precursor and the square root of the mass ratio of the gas carrier and the seeds, but only slightly by the position along the axis after 10 mm.
An issue of this model, is that it does not take into account the presence of the plasma. When the plasma is generated, the temperature in the reservoir chamber rises. The effect of a plasma can limit the particles aggregation also by reducing the number of collisions because of the repulsive electrostatic force. The bigger is a cluster, the more electrons and ions it collects as it becomes charged. Its surface (floating) potential is determined from the balance of collected ion and electron fluxes. Since electrons are much more mobile than ions, the surface potential is negative and roughly equal to the electron temperature. This ensures that most of the electrons are unable to overcome the potential barrier between the particle surface and surrounding plasma, and hence, ion and electron fluxes can balance each other. However the plasma along the jet is hardly collisional and in a particular pre-sheath state: the presence of a plasma indeed may limit the particles nucleation, but not as effectively as in the main plasma region, allowing a weak nucleation. In addition to this the presence of energetic ions favors the condensation of clusters, creating centers of nucleation.

## 6.4 Precursor injection and dissociation

Heating the precursor injection system at temperatures about 45 °C we obtained stable TTIP fluxes of approximately 0.48 g per hour inside the plasma chamber. Inside the argon-oxygen plasma, TTIP (m/z = 284) is dissociated and can be analyzed by OES.

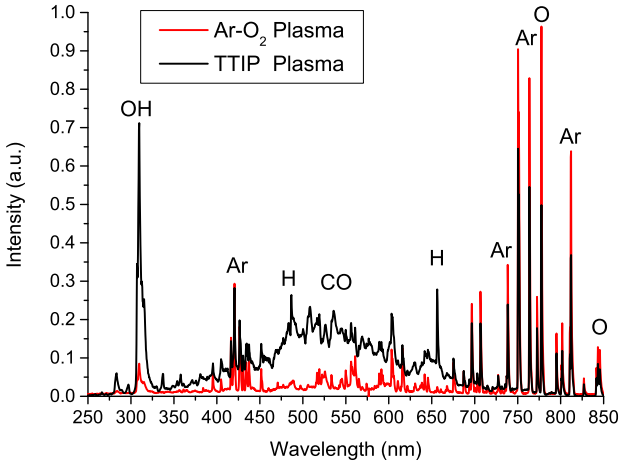


Figure 6.4: Two successively optical emission spectra measured first in a simple argon-oxygen plasma discharge (red line) and then injecting the TTIP precursor (black line).

Typical optical emission spectroscopy results are shown in Fig. 6.4. Different emission lines of excited atoms and molecules were identified and their intensity was measured during each plasma deposition. Optical spectra measured before the TTIP precursor injection are dominated by emission lines of neutral atoms of argon and oxygen. When the titanium precursor is vaporized and injected inside the plasma reactor, new lines appear in the spectra emitted from hydrogen, carbon monoxide and hydroxyl radical at emission lines respectively 487 and 565 nm, from 500 to 600 nm, 309 nm. Varying the temperature used to vaporize the TTIP we can control the precursor flow inside the plasma chamber. Using actinometry it is possible to monitor the concentration of the radical species related to the TTIP dissociation and oxidation reactions. The radical oxygen reduction is clearly visible from the emission spectra.

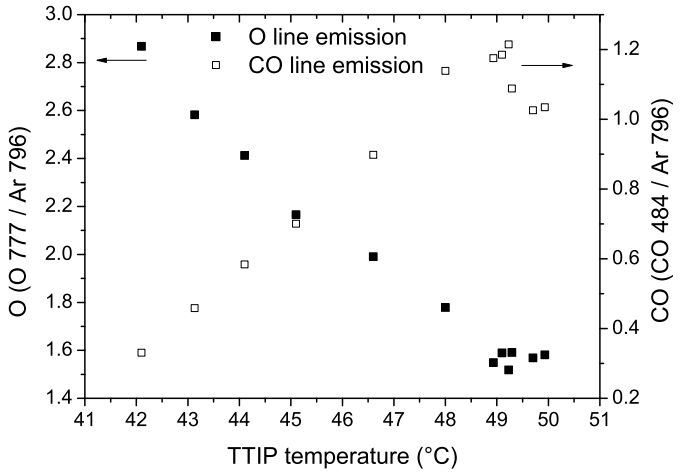


Figure 6.5: Emission lines of atomic oxygen at 777 nm (black squares) and of carbon monoxide at 484 nm (white squares) as a function of the TTIP precursor temperature in the vaporizer. Both the intensities were normalized to Ar lines in order to evaluate a value proportional to the density of the species considered.

In Fig. 6.5 concentration of O and CO is plotted as a function of the precursor temperature measured in the vaporizer. The two intensity values, dark subtracted and normalized to the optical spectrometer $\lambda$-dependent function, were divided by the intensity of argon line 796 to obtain an intensity proportional to the density of the species. In this way we can monitor the abundance of the precursor inside the plasma chamber and control the deposition rate. As the temperature increases more precursor molecules are injected into the reactor. This relation seems linear and is observable an increase of CO and other dissociation products while the radical oxygen concentration greatly decreases during the oxidation process.
A similar experiment was repeated measuring with a mass spectrometer the signal for different precursor products at a fixed position.

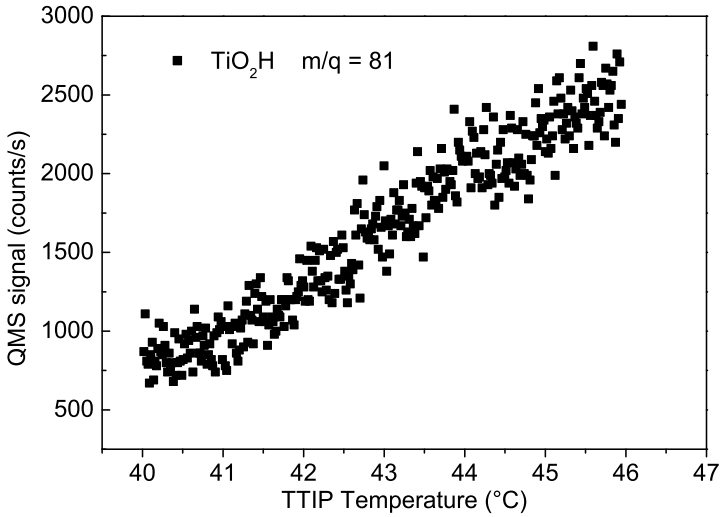


Figure 6.6: Quadrupole mass spectrometry signal measured for neutral $TiO_2H$ as a function of the precursor temperature. These data were acquired during a plasma discharge at 450 W while gradually increasing the precursor temperature and flux. The spectrometer was placed along the supersonic jet at 10 mm from the nozzle orifice.

In Fig. 6.6, for example, it is shown the trend of the mass peak corresponding to $TiO_2H$ (m=81 amu). Again the dependency is linearly, as the precursor flux increases in the first chamber, also along the jet more TTIP products can be measured. A more complete spectrum of the precursor dissociation was easily measured with the QMS and it is reported in Fig. 6.7, while in table 6.1 the identified species are shown (determined from both literature and looking at the titanium isotope ratios).

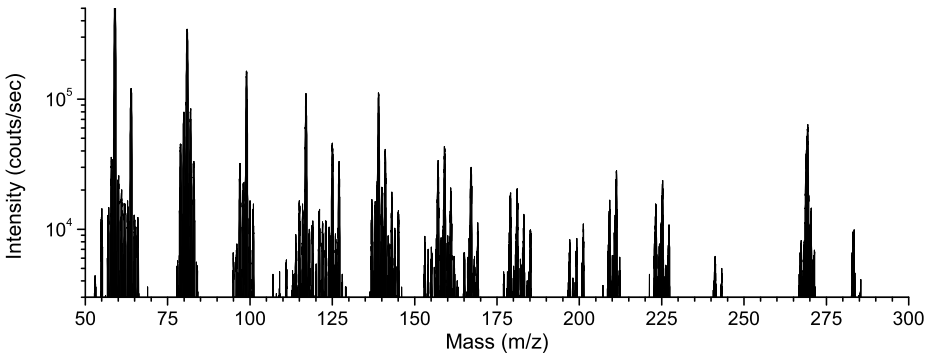


Figure 6.7: Mass spectra measured at 5 mm of distance from the nozzle during a plasma discharge with TTIP. Electron impact ionization at 70 eV creates different fragments which alter the real chemical composition detected. Most of these peaks have also been measured as ions, so they are originated outside of the QMS and present in the jet, but their sensitivity can not be fully trusted due to the mass dependent transmission function of the spectrometer.

In the mass range from 300 to 1000 amu/q no evidence of other species or nanopar-

Table 6.1: Main products of the TTIP (m/z=284,$Ti(OCH(CH_3)_2)_4$) dissociation measured during experiments.

| m/z | Ion | m/z | Ion |
|---|---|---|---|
| 15 | $CH_3$ | 139 | $TiO_2(OCH(CH_3)_2)$ |
| 43 | $CH(CH_3)_2$ | 167 | $Ti(OCH(CH_3)_2)_2H$ |
| 59 | $OCH(CH_3)_2$ | 181 | $TiO(OCH(CH_3)_2)_2$-H |
| 64 | TiO | 211 | $Ti(OCH(CH_3)_2)_3H$-$CH_3$ |
| 81 | $TiO_2H$ | 225 | $Ti(OCH(CH_3)_2)_3$ |
| 99 | $TiO_3H_3$ | 243 | $Ti(OCH(CH_3)_2)_4$-$CH(CH_3)_2$ |
| 125 | $TiO(OCH(CH_3)_2)$ | 269 | $Ti(OCH(CH_3)_2)_4$-$CH_3$ |

ticles was found with this set-up. Only two small peaks could be observed at 321, 323 which could be associated to $(TiO_2)_4$ aggregates, as shown in Fig. 6.8.

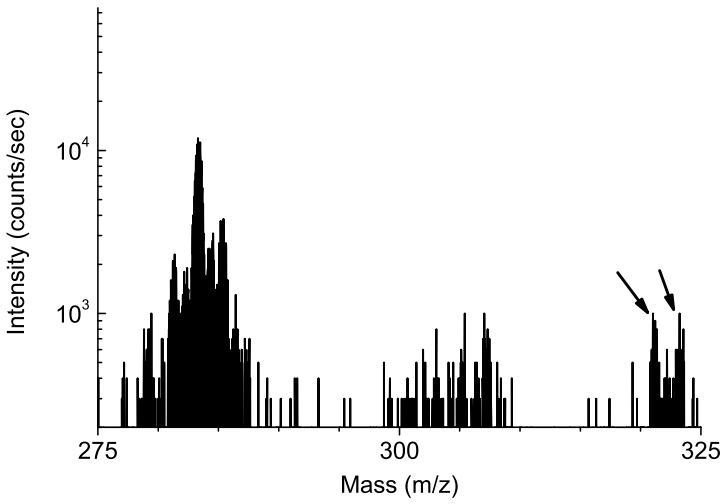


Figure 6.8: Detail of a mass spectra measured at 5 mm of distance from the nozzle during a plasma discharge with TTIP. Here it is possible to spot two peaks about 320 amu, above the precursor monomer molecular weight (284 amu). These peaks may be related to the presence of titanium oxides clusters.

The 70 eV electron energy of the source is too high to preserve most of these nanoparticles. Moreover the analysis of mass spectra on a wide mass range is somewhat complicated by the mass dependent instrument transmission function. Different works in literature reports a transmission function proportional to $M^{-x}$, with $1 < x < 2$, depending on the instrument internal configuration of the transmission optics. This implies that the signal measured for high mass species can be highly reduced from the instrument. However the mass peak at M=269 amu/q is well distinguishable, meaning that the precursor is reasonably not fully dissociated. Making a great approximation, the ratio between the mass peaks 269, corresponding to the unreacted

precursor, and 81, corresponding to the correctly dissociated precursor is near to 1 to 10. Considering a mass transmission function where $x = 1$, this ratio could become close to 1 to 4, suggesting that 4/5 of the titanium isopropoxide monomers are well dissociated. This can be used as a relative parameter to confront different experimental condition.

## 6.5 QMS profiles of the supersonic jet

### 6.5.1 Supersonic jet profiles along the centerline

The supersonic jet profiles ware studied in the presence of TTIP. The plasma was generated with a discharge power of 450 W, and the precursor generally introduced with a stable mass flow of 0.48 g/h at constant temperature. The QMS was moved along the jet axis of symmetry acquiring ion and neutral mass spectra separately. Also IEDFs were acquired to first study the different ion energy distribution functions. The total area of these distributions can be calculated to obtain an effective total ion flux. Again for the measurement of ion mass spectra, a single ion energy was chosen. Ion mass spectra were taken at a fixed energy (8 eV) corresponding to the most energetic ions. This analysis was then repeated observing the jet out of its axis. This was possible by replacing the nozzle ending orifice with a similar orifice (still circular having 6.9 mm of diameter) in which the center was slightly shifted by 5 mm respect to the other. This allowed an analysis of the side region of the jet, which is relevant when is to be performed a thin film deposition over sufficiently high area.

Inside the supersonic jet, the heavy TTIP products are accelerated from the argon-oxygen mixture at velocities comparable to a fraction of the light gas flow velocity, as a function of their mass and diameter. First we studied the distribution of neutral species. The values for argon and oxygen nicely resemble the results obtained for the simple plasma discussed above.

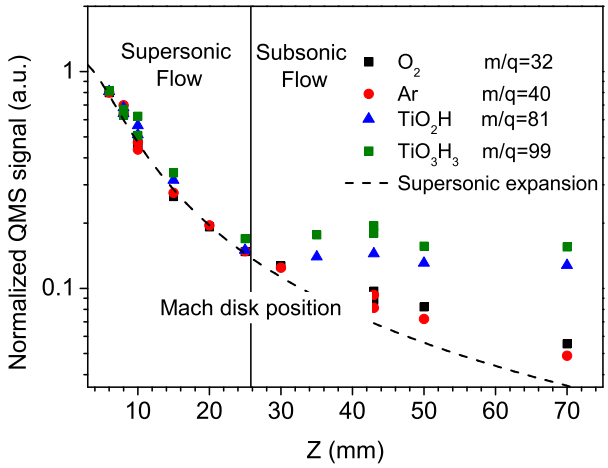


Figure 6.9: QMS data acquired along the supersonic jet axis for neutrals species from TTIP reactive plasma. Data for argon, molecular oxygen and two typical light $TiO_x$ seeds are shown. Data have been normalized to reproduce the density variation expected during the supersonic expansion (dashed curve). The Mach disk position $z_M$ determines the shock inside the chamber and is indicated with a vertical bar.

Figure 6.9 shows the peak area of some gas species calculated from mass spectra acquired at different positions. In particular argon (M=40), molecular oxygen (M=32), $TiO_2H$ (M=81) and $TiO_3H_3$ (M=99) are shown. Also the precursor seeds follow the theoretical isentropic expansion law, but, differently from the light gas carrier, after the Mach disk location the behavior different: there is not a decrease of the measured signal. The peak area for the products of the precursor dissociation is constant after the mach disk. This phenomenon is due to the long mean free path related to the low pressure in the deposition chamber and to the heavier mass. Thanks to their inertia, $TiO_x$ seeds do not expands further after the mach disk. In particular different accelerations due to drag forces and slip-factors can cause particles separation along the jet and the retention of heavier species along its centerline. The analysis of the jet profiles was repeated measuring also ion mass spectra. The results for some selected peaks are shown in Fig.s 6.10 and 6.11, alongside the profiles of the relative neutral species measured.

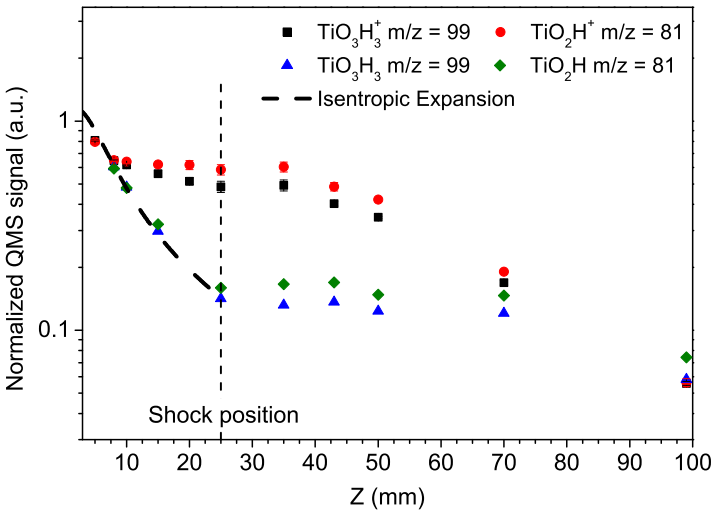


Figure 6.10: QMS data acquired along the supersonic jet axis for neutrals species from TTIP reactive plasma. Data for $TiO_2H$ (M=81), $TiO_3H_3$ (M=99) and the relative ions are shown. The peaks areas have been normalized to reproduce the density variation expected during the supersonic expansion (dashed curve). The Mach disk position $z_M$ determines the shock inside the chamber and is indicated with a vertical bar.

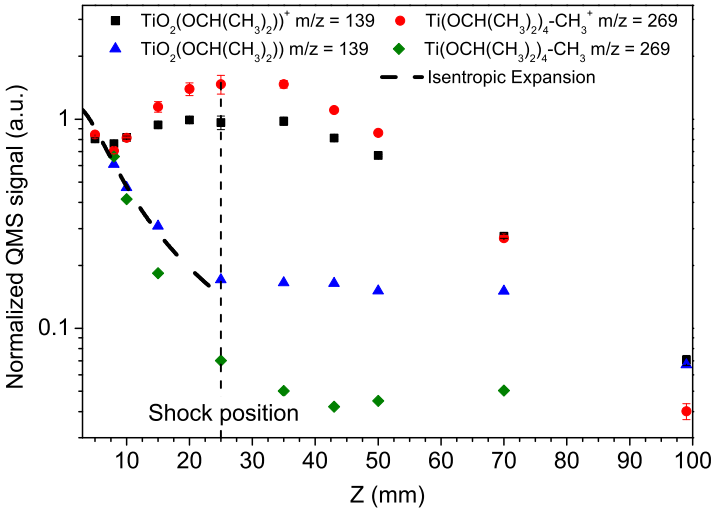


Figure 6.11: QMS data acquired along the supersonic jet axis for neutrals species from TTIP reactive plasma. Data for $TiO_2(OCH(CH_3)_2)$ (M=139), $Ti(OCH(CH_3)_2)_4$-$CH_3$ (M=269) and the relative ions are shown. The peaks areas have been normalized to reproduce the density variation expected during the supersonic expansion (dashed curve). The Mach disk position $z_M$ determines the shock inside the chamber and is indicated with a vertical bar.

The ion species measured at 8 eV for the precursor molecules shown a much greater effect of the ion flux enhancement previously observed for the argon-oxygen plasma. Moreover this enhancement is higher for $Ti(OCH(CH_3)_2)_4$-$CH_3$ (the heaviest of the

masses observed) and the flux measured over the Mach disk for this ion is twice larger than what was measured in the first millimeters of the expansion. The study of the ion energy distribution functions can help in the understanding of this particular behavior. Again IEDFs were measured along the axis, for the gas carrier and some selected $TiO_x$ seeds.

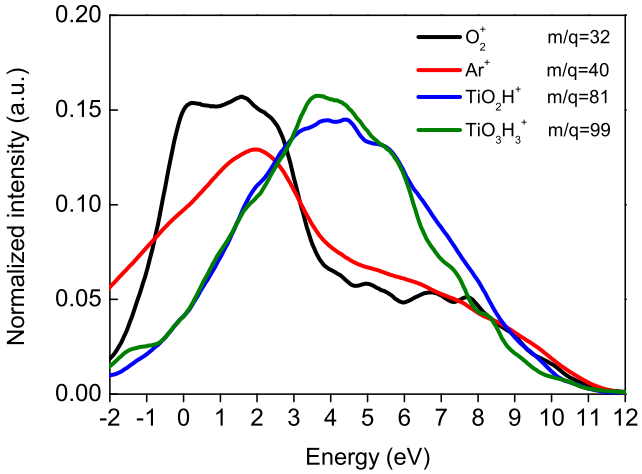


Figure 6.12: Ion energy distribution functions for argon, molecular oxygen, $TiO_2H$ and $TiO_3H_3$ measured inside the supersonic expansion (at 15 mm of distance from the orifice) along the supersonic jet axis. Plasma discharge was maintained at 450 W and the precursor injected constantly at 41°C. The IEDFs were normalized to reproduce the same area.

In Fig. 6.12 the ion energy distribution functions for argon, molecular oxygen, $TiO_2H$ and $TiO_3H_3$ are shown, at a single position inside the supersonic jet expansion. Energies for argon and oxygen resemble those already measured for the argon-oxygen plasma without the precursor. Argon and oxygen ions are distributed over a wide range of energies and exhibit different peaks, among which it is dominant the low energy one due to the effect of collisions. Conversely the energy distributions for the $TiO_x$ seeds are peaked over moderately-high energies (about 5 eV). However these distributions are not exactly mono-energetic even if they indicates a single peak. The energy distributions of the titanium ions are wide. These results suggest that new titanium ions are not formed along the jet and that when they undergo a collisions they may lose their charge or dissociate. Such a spread in the energy distribution may arise if we assume that these ions are not likely to undergo charge transfer reactions. This is reasonable since charge exchange is much favored between molecules of similar weight and the argon and oxygen particles have the biggest densities along the jet. Titanium oxide ions are more likely to lose part of their energy through elastic scattering reactions. The ion energy distribution functions measured were then integrated over the whole energy spectra to give a total ion flux, which is displayed in Figs. 6.13.

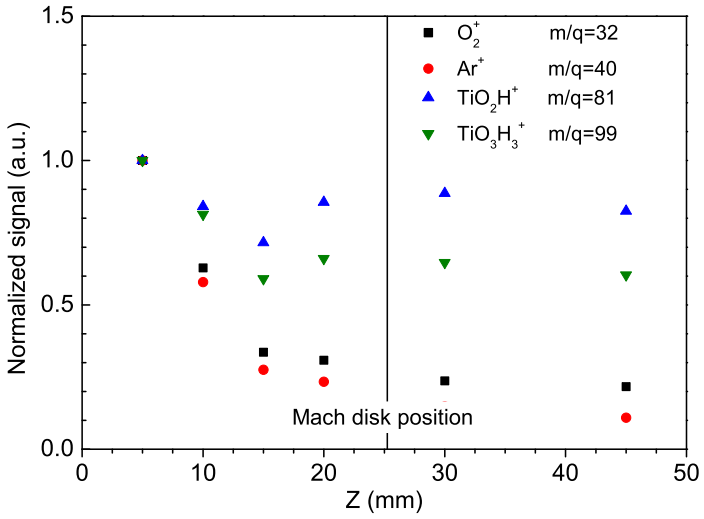


Figure 6.13: QMS data acquired along the supersonic jet axis for ions from a TTIP reactive plasma. Data for argon, molecular oxygen and two typical light $TiO_x$ seeds are shown. Data have been normalized to reproduce the density variation expected during the supersonic expansion (dashed curve). The Mach disk position $z_M$ determines the shock inside the chamber and is indicated with a vertical bar.

In Figs. 6.13 the axial density profile for argon, molecular oxygen and light $TiO_x$ seeds ($TiO_2H$ and $TiO_3H_3$, respectively m=81 amu and m=99 amu) are shown for the total ion flux, considering contribution also from collisional ions. The experimental data seem in fair agreement with the isentropic expansion law displayed with a dashed curve until the shock position (even if we do not expect the density and the flux to correspond). The behavior of $TiO_2H$ and $TiO_3H_3$ show now a more pronounced flux enhancement after the Mach disk. The difference between the gas carrier and the titanium ions could be ascribed to the different shape of their ion energy distribution functions. The energy of $TiO_x$ ions shown no trace of low energetic ions and is peaked over a single energy.

### 6.5.2 Supersonic jet profiles off-axis

Similar measurements were conducted shifting the orifice off axis by 5 mm. In this way the supersonic jet resulted shifted respect to the quadrupole mass spectrometer. This was done to study the profile of the supersonic expansion far from the jet axis, but still in a region which is involved in the thin film deposition, whose area should be as wide as possible. It is important to evaluate the approximate aperture of our jet, to understand whether our spectrometer is sampling the supersonic jet or the background. The angle of aperture of the jet from the axis centerline can be estimated using:

$$\theta_M = 5.3 \left( \frac{P_p}{P_d} \right)^{0.6} \tag{6.3}$$

where $P_p$ and $P_d$ are respectively the pressures in the plasma and the deposition chambers. At the considered experimental conditions (in which the pressure ratio is near to 28) we have $\theta_M = 40°$. It is thus possible to estimate a critical position $z_{crit}$ which represent a distance from the orifice below which the instrument sampling orifice is mainly sampling gas from the background gas rather than from the supersonic jet.

$$z_{crit} = h \cdot tan(90 - \theta_M) \tag{6.4}$$

Where $h$ is the distance between the axis where the spectrometer is moved and the axis of symmetry of the supersonic jet, here equal to 5 mm, then $z_{crit} = 6$ mm. This ensures that our measurements are within the supersonic jet expansion cone, at least when performed over $z = 6$ mm. It is important to remember that the following measurements are no longer performed on a streamline of the supersonic jet.

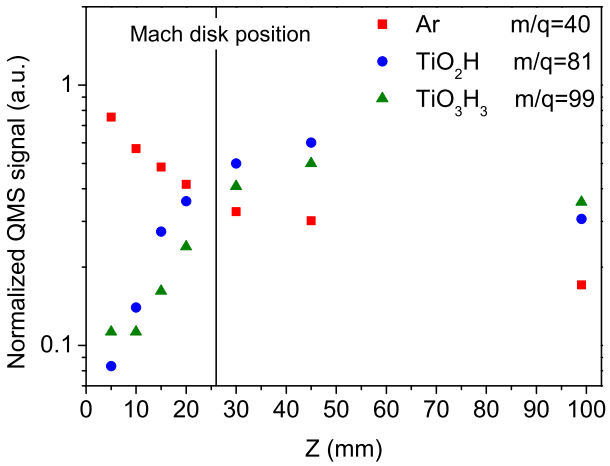


Figure 6.14: QMS data acquired along the supersonic jet, off-axis for neutrals species from TTIP reactive plasma. Data for argon and two typical light $TiO_x$ seeds are shown. Data have been normalized to reproduce the density variation expected during the supersonic expansion (dashed curve). The Mach disk position $z_M$ determines the shock inside the chamber and is indicated with a vertical bar.

In Fig. 6.14 the off axis profiles for Ar and two typical $TiO_x$ seeds are shown for the neutral particles. Neutral profiles displayed in Fig. 6.14 show a very different trend for Ar and the titanium particles: while Ar signal still decreases at 5 mm from the axis center, the titanium seeds increase in counts with increasing distance from the nozzle. This different behavior is due to the slip factors and perpendicular drag forces which increase with the mass difference between the particles and the gas carrier mixture. Heavier particles are retained inside the center of the jet. They begin to spread laterally only later as the gas further expands, significantly increasing the signal measured from the mass spectrometer.
Also ion energy distribution functions were measured and then integrated over each

energy to obtain an integrated ion flux. A typical spectra for each one of the species considered is shown in Fig. 6.15. Ions detected in these off-axis positions are far from the main axis, thus mostly scattered ions can be found here. This explains the low energy detected for Ar and $O_2$ off-axis.

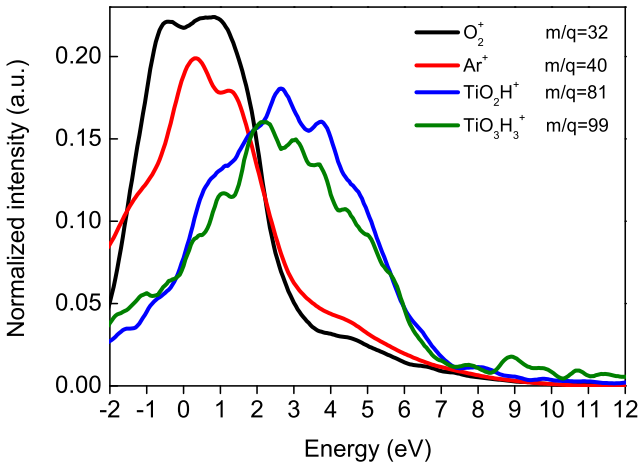


Figure 6.15: Ion energy distribution functions for argon, molecular oxygen, $TiO_2H$ and $TiO_3H_3$ measured inside the supersonic expansion (at 15 mm of distance from the orifice) out of the supersonic expansion axis. Plasma discharge was maintained at 450 W and the precursor injected constantly at 41°C. The IEDFs were normalized to reproduce the same area.

The ion energy distribution shown in Fig. 6.15 reports ions which are detected at 15 mm from the orifice and 5 mm off its axis, far enough from $z_{crit}$. These are indeed the least energetic ions. The signal appears noisy due to the low intensity.

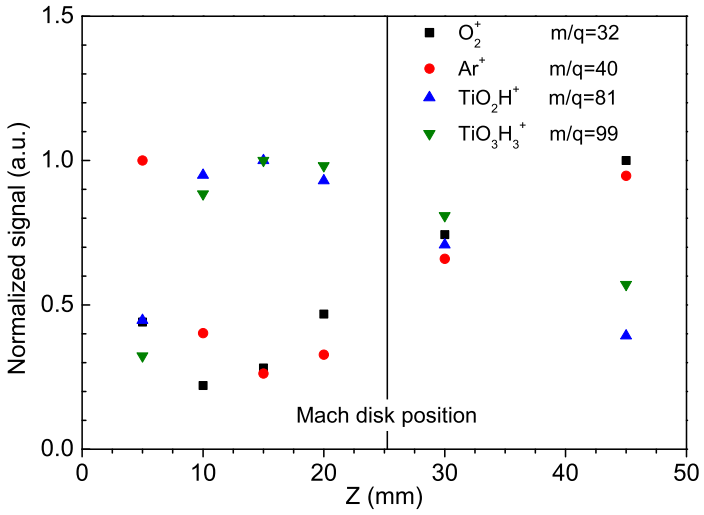


Figure 6.16: QMS data acquired along the supersonic jet, off-axis for ions from a TTIP reactive plasma. Data for argon, molecular oxygen and two typical light $TiO_x$ seeds are shown. Data have been normalized to reproduce the density variation expected during the supersonic expansion (dashed curve). The Mach disk position $z_M$ determines the shock inside the chamber and is indicated with a vertical bar.

The ion flux signal displayed in Fig.6.16 represents the total ion flux, integrated over the whole energy spectra measured at different positions along the supersonic jet, off axis. Again there is an evident difference between the gas carrier mixture and the titanium seeds. The profiles for titanium ions resemble their neutral off-axis trends. This can be again ascribed to the retention of heavier masses over the center. The profiles for argon and molecular oxygen ions instead differs from their neutral counterparts and from their ion profiles on the axis centerlines. The total flux of the ions of gas mixture decreases along the jet and increase after the mach disk location, showing a strong flux enhancement which can be due to the spread of the jet after the Mach disk.

## 6.6 Summary and Conclusions

Optical emission spectroscopy was employed during each measurement to control the mass flow of the precursor. From the optical spectra, when the precursor is injected, it is possible to identify different products of the titanium isopropoxide dissociation and oxidation. As the temperature of the precursor tank is raised, the mass flow of the precursor linearly increases. A similar trend was confirmed by the QMS measurements observing the titanium products along the jet. Sampling neutral gas species and ions at different distances from the nozzle it was possible to gain an insight on the precursor dissociation and the components also along the supersonic jet. Many molecules of partly dissociated precursor could be observed. The study of the supersonic jet profiles for the $TiO_x$ seeds was then performed. Titanium

nanoparticles follow the isentropic expansion, as the light gas carrier, until the Mach disk location, then they maintain their density also over long distances. This is due to an inertial effect, which maintain the heavier species near the jet centerline. This is a particular interesting feature because it allows to perform thin film deposition also far from the nozzle, where the jet is no longer supersonic. Each $TiO_x$ seed can also be measured as an ion in the jet. The ion energy distribution functions of these species are very particular as they show a wide energy spectrum centered about 5 eV. It is also very intense the ion flux enhancement for heavier seeds after the Mach disk. Similar measurements were also performed shifting the expansion radially by 5 mm from the mass spectrometer orifice. This allowed a study of jet off from its axis, still in a region which is relevant for thin films deposition. The enrichment of heavier species in the more central part of the jet is quite evident, as in the profile for the neutral components the gas carrier still show a expansion whereas the abundance $TiO_x$ seeds studied drops to zero when the spectrometer is close to the nozzle as they are retained over the central part of the jet. A similar effect can also be observed for the ions, which can be found only at lower energies.

CHAPTER

# 7

# THIN FILMS DEPOSITION

Thin films made of titanium dioxide have been widely used for different applications in a great number of research areas: $TiO_2$ is biologically and chemically inert, it combines a high dielectric constant with high refractive index and exhibits a wide-bandgap. These properties make it well suited for microelectronic and semiconductors applications, for the production of sensors, ultraviolet filters and antireflection coating, photocatalysts and photovoltaic [7, 8, 9, 10, 127].
Among these applications, photovotaic is one of the most important for $TiO_2$. One of the key components of a dye sensitized solar cells (DSC) is the photoanode, which is based on a wide band-gap semiconductor thin film coated on a fluorine doped tin oxide (FTO) glass, which is responsible for electron transport and collection following the photosensitizer excitation upon light harvesting. Although a number of metal oxides have been tested as n-type semiconductors, titanium oxide ($TiO_2$), to which the photosensitizer molecules are chemically grafted, has given so far the best results because of its large surface area, good light absorption, and high photo-electrical response as a porous photo-electrode [128].
Unfortunately, the use of a $TiO_2$ photoanode prepared from commonly used methods (colloidal nanoparticles paste) likely hampers the improvement of DSC efficiency because of the presence of numerous grain boundaries, which significantly reduces electron mobility. In addition, the presence of a basically disordered network impedes an optimal loading of the photosensitizer, which is important in order to enhance sunlight absorption [129]. To address these issues different kinds of one-dimensional ordered nanostructures (nanorods, nanowires, and nanotubes) have been recently proposed [130, 131, 132, 133, 134]. Indeed, one-dimensional $TiO_2$ nanostructures

improve the electron mobility, thanks to the higher order of the oxide network, and the surface area for enhancing dye adsorbtion, but in some cases insufficient sites for dye attachment may be present [135]. An ordered architecture offers a more direct charge transport pathway and can reduce charge recombination, giving rise to surface electrical fields which confine the injected electrons in the central zone of the wires [136, 137].
Furthermore, light harvesting is enhanced by a superior light harvesting ability of the nanostructured films. Recently, DSCs based on hierarchically structured $TiO_2$ nanotubes have yielded a remarkable PCE of more than 7% and those based on hierarchical TiO microspheres yielded more than 8–10% [138, 139]. A strategic aspect for the industrial development of the DSC technology is represented by the replacement of the commonly used liquid and corrosive electrolyte based on the iodine–iodide couple by solid hole-transport materials (HTM) for building solid state DSCs (ssDSCs) [140, 141]. This novel kind of solar cell can further increase the overall efficiency of photovoltaic devices, but much of the current is still loss due to the uncontrolled morphology of the $TiO_2$ photonanode. Controlling the nano-morphology of the $TiO_2$ layer can enhance the DSC performances. Indeed, recent studies have demonstrated that a hierarchical assembly of nanocrystalline particles of $TiO_2$ may represent the most efficient morphology for optimized DSC photoanodes [142, 143].
One of the main goal of this thesis is to fully characterize Plasma Assisted Supersonic Jet Deposition (PA-SJD), demonstrating that it is a promising new approach for the controlled growth of thin films. A detailed understanding of the physics involved in this source is fundamental in order of being able to control the growth and the morphology for nanostructured depositions effectively tuning the properties of photovoltaics devices. The analysis of the thin films growth process and their morphology is important to relate the properties of the films to the main plasma and fluid dynamics parameters of PA-SJD.
In this chapter we focus on the deposition procedure and on the analysis of thin films. $TiO_2$ depositions were performed changing the substrate position along the jet and the precursor mass flow rate. Different films were grown both for studying how their properties scales with the deposition parameters and for producing samples for photovoltaics devices. Thin films were at first characterized using a contact profilometer, to measure their height and profiles to evaluate the growth rate and their shape. To observe the film chemistry we used a FT-IR interferometer, detecting the relative concentration of Ti-O and C-O, O-H bounds. The film morphology was then analyzed with an AFM detecting the film surface roughness and was observed by SEM and TEM microscopy for a direct observation of the film structure.

## 7.1 Experimental setup

Figure 7.1 shows a schematic view of the experimental set-up for PA-SJD which was used for the thin films depositions.

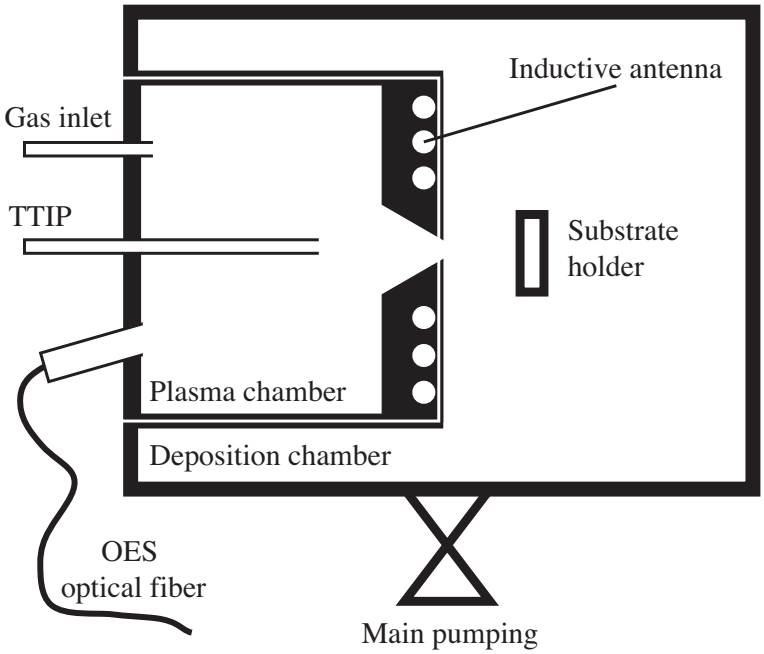


Figure 7.1: Schematic view of the experimental setup. The mass spectrometer sampling orifice can be moved horizontally inside the deposition chamber. OES were acquired from the oblique window (16° to the perpendicular) facing the plasma chamber.

We claim that, over conventional gas phase processes, the proposed technique allows control of the kinetic energy of clusters, hence control on their assembly pattern on the substrate. In particular when molecular cluster deposition is performed under conditions of supersonic jet several advantages could be envisaged including the better collimation and stability and the control of crystallinity. Thin films depositions were performed for different exposure times (ranging from few minutes to one hour of deposition), precursor mass flow rates, substrate positions along the supersonic jet and on two kind of substrate. We used both silicon and fluorine tin-doped oxide glass (FTO glass), in particular the latter was used for making photoanodes for DSSC and ssDSSC. The deposition process by PA-SJD takes place as follows:

- First the argon and oxygen gas mixture is formed inside the plasma chamber, at a defined pressure (8 Pa) and concentration (oxygen to argon respectively 3 to 2)
- The plasma discharge is established at 450 W
- When the plasma is stable the precursor is heated and its valve opened

- The sample (silicon or FTO glass) is set at the desired position along the jet for the established time

During each deposition optical emission spectroscopy (OES) was used to control the discharge parameters, stability and to monitor the precursor flow (ensuring the repeatability of each deposition). Optical emission spectroscopy (OES) is a well know non-intrusive diagnostics which has already been applied in many plasma discharges. Revealing the light emitted from atoms, molecules and ions which are excited from free electrons in the discharge, it is possible to understand the main reaction processes in the plasma. The intensity of emission lines can identify chemical species and allows to gain insight about their abundances. From the quartz window facing the plasma chamber optical emission spectra (OES) were acquired using two different low resolution spectrometers, as already described previously, to monitor the entrance and the dissociation of the precursor.
With PA-SJD it is possible to cover a substrate area of a few $cm^2$. In most of the films deposited in this work we covered each substrate with two different squared mask (5 or 7 mm for side). An important step for achievement of high purity levels of films was the thermal annealing which was performed at 500° for about 1 hour, effectively removing organic impurities and changing the film structure to a anatase crystal. The thickness of the $TiO_2$ films, measured by means of a profilometer, was controlled by varying the exposure time to the plasma jet, the precursor mass flow and the position of the substrate along the expansion. Film stoichiometry was analyzed by infrared interferometry and their structure and morphology studied by means of AFM, TEM and SEM microscopy.

## 7.2 The growth of thin films

In PA-SJD clusters of molecules and nanoparticles are formed in the expanding jet and then deposited on a substrate at different energies depending on the jet parameters. The dimension and energy of these clusters is directly related to the properties and to the structure of the thin films, thus it is important to both study their nucleation and deposition on the substrate. Molecular aggregates evolve spontaneously towards the most stable possible structure. The supersonic jet is the ideal environment for the controlled production of molecular clusters. As the gas expands both temperature and density decrease favoring the control on the condensation conditions and on the collision rates. Here small clusters are at first formed through molecule-molecule or molecule-cluster collisions, then bigger clusters can thus be formed by three body collisions, where the third body retains the excess of collisional energy preventing the cluster breaking. There is not a quantitative theory for the cluster nucleation and film growth in such a complicated environment, however it is possible to develop different models, based on the present theory and the ex-

perimental evidence, to describe how different parameters are involved in thin film growth.
The impact and dynamics of nanoparticles on the substrate have a significant influence on the film formation. More generally all phase transformations, including thin-film formation, involve the processes of nucleation and growth. During the earliest stages of film formation, a sufficient number of vapor atoms or molecules condense and establish a permanent residence on the substrate. Soon after exposure of the substrate to the incident vapor, a uniform distribution of small but highly mobile clusters or islands is observed. In this stage the prior nuclei incorporate impinging atoms and subcritical clusters and grow in size while the island density rapidly saturates. The next stage involves merging of the islands by a coalescence phenomenon that is liquid-like in character especially at high substrate temperatures. Coalescence decreases the island density, resulting in local denuding of the substrate where further nucleation can then occur. Crystallographic facets and orientations are frequently preserved on islands and at interfaces between initially disoriented, coalesced particles. Coalescence continues until a connected network with unfilled channels in between develops. With further deposition, the channels fill in and shrink, leaving isolated voids behind. Finally, even the voids fill in completely, and the film is said to be continuous.
The energy of an impinging nanoparticle determines different mechanisms on the film when it lies on its surface:

- Adsorption, when the particle establishes a binding with the atoms present in the film
- Diffusion, when part of the particle energy is retained, which can move on the surface.
- Nucleation, when the particle energy is sufficiently high to create new aggregates.
- Desorption, when a very energetic particle has enough energy to leave the film.

Considering these phenomena, during the first phase of the formation of a thin film small aggregates or bigger islands can be generated and evolve into different structures. The many observations of film formation have pointed to three basic growth modes: island (or Volmer-Weber), layer (or Frank-van der Merwe), and Stranski-Krastanov, which are represented in Fig. 7.2 [13, 12].

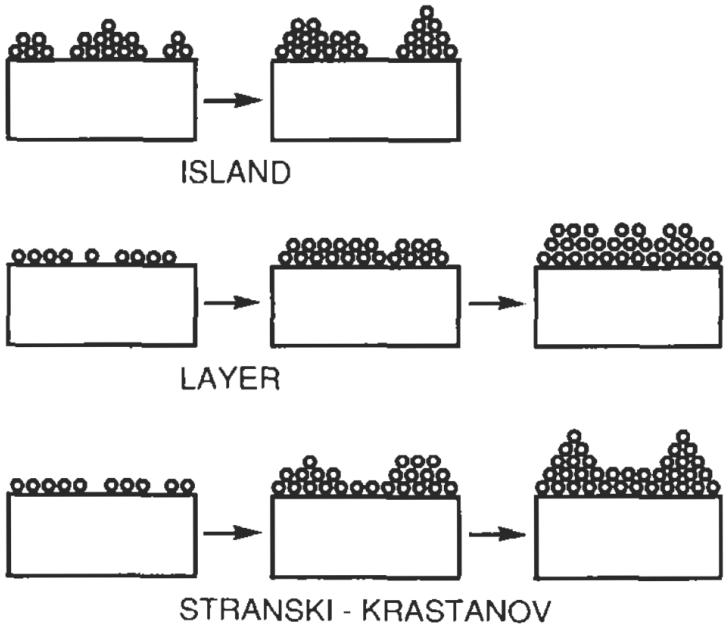


Figure 7.2: Sketches of the main three growth modes: island (or Volmer-Weber), layer (or Frank-van der Merwe), and Stranski-Krastanov.

Island growth occurs when the smallest stable clusters nucleate on the substrate and grow in three dimensions to form islands. This happens when atoms or molecules in the deposit are more strongly bound to each other than to the substrate. Many systems of metals on insulators, alkali halide crystals, graphite, and mica substrates display this mode of growth. The opposite characteristics are displayed during layer growth. Here the extension of the smallest stable nucleus occurs overwhelmingly in two dimensions resulting in the formation of planar sheets. In this growth mode the atoms are more strongly bound to the substrate than to each other. The first complete monolayer is then covered with a somewhat less tightly bound second layer. Providing the decrease in bonding energy is continuous toward the bulk crystal value, the layer growth mode is sustained. The most important example of this growth mode involves single-crystal epitaxial growth of semiconductor films. The layer plus island or Stranski-Krastanov (S.K.) growth mechanism is an intermediate combination of the aforementioned modes. In this case, after forming one or more monolayers, subsequent layer growth becomes unfavorable and islands form. The transition from two- to three-dimensional growth is not completely understood, but any factor that disturbs the monotonic decrease in binding energy characteristic of layer growth may be the cause. For example, due to film-substrate lattice mismatch, strain energy accumulates in the growing film. When released, the high energy at the deposit-intermediate- layer interface may trigger island formation. This growth mode is fairly common and has been observed in metal-metal and metal-semiconductor systems. At an extreme far removed from early film formation phenomena is a regime of structural effects related to the actual grain morphology of

polycrystalline films and coatings. This external grain structure together with the internal defect, void, or porosity distributions frequently determines many of the engineering properties of films. For example, columnar structures, which interestingly develop in amorphous as well as polycrystalline films, have a profound effect on magnetic, optical, electrical, and mechanical properties. Different grain and deposit morphologies can be obtained as a function of deposition variables. Modification of the film structure through ion bombardment or laser processing both during and after deposition can result in additional structures.

Another important process to be considered is the shadowing effect. This phenomenon depends on the geometry and the dynamics of impinging nanoparticles or on the substrate roughness. To help understanding the effects of diffusion, desorption and shadowing on the film growth, it is possible to consider a more detailed zone model developed by Thornton, where different film morphologies are related to the combination of shadowing and diffusion processes (see Fig. 7.3) [2, 144].

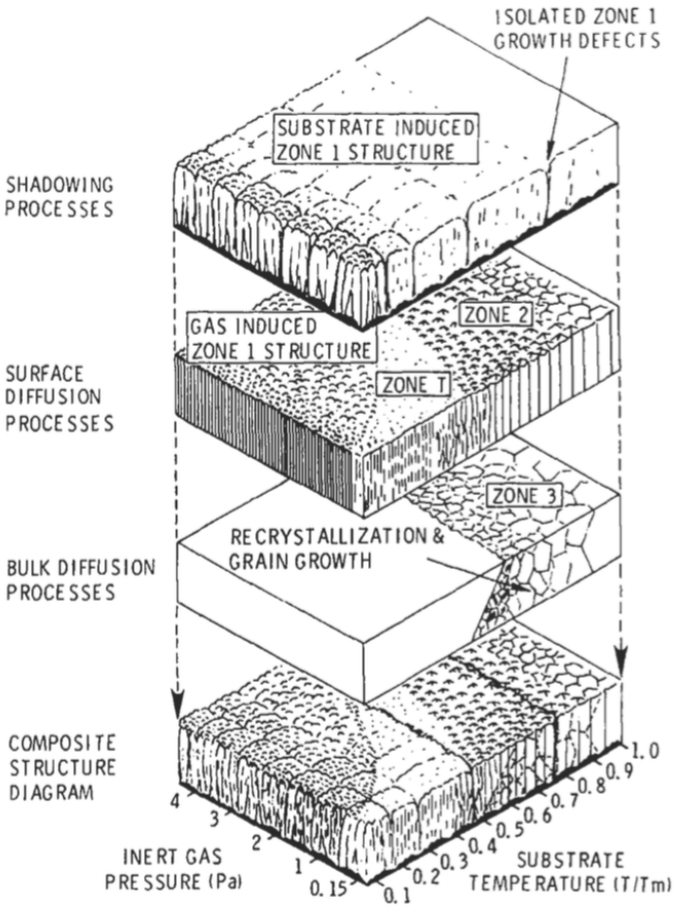


Figure 7.3: Schematic representation showing the superposition of physical processes which establish structural zones.

The energy (and thus kinetic temperature) of the nanoparticles in the jet and the gas pressure along the expansion locate PA-SJD depositions between zone 1 and zone

T, where the temperature is generally low and the pressure can range, depending on the jet properties, forming fine columnar structures.
Columnar structures arise when the mobility of atoms is limited, such as in our case. This implies that the film morphology can be ideally reproduced by an hit and stick model. The geometry thus plays a very important role, since the jet is ideally axis-symmetrical, while the main thermodynamical parameters vary on the radial coordinate. V-Shaped and tree-like columnar structures can be easily produced by PA-SJD [11, 6].
Naturally, considerable interest has developed in studying evolving growth morphologies at various length and time scales under nonequilibrium conditions over the last three decades. In an effort to understand the fundamental nature of the growth processes, their universal aspects, as well as detail short length scale structures of the evolving morphologies, various simulation models have been developed. Random deposition (RD) and ballistic deposition (BD) models, the diffusion limited aggregation (DLA) model [145], the Eden model, and the random sequential adsorption (SRA) model [146], to name a few, were inspired by and designed to model specific phenomena. The BD model is one of the simplest models among those mentioned above. It was independently introduced by Vold [147] and Sutherland [148] originally to study the sedimentation phenomena of colloidal particles. But in recent years the interest in studying the BD model has shifted to understand the growth of thin films [149]. In the regular BD model the sticking probability $p_s$ (the probability to create a bound upon touching the surface) is considered to be unity. Robledo et al. [150] generalized the rules for random deposition by varying the sticking probability to be less than unity. This generalization was extended even further where one assigns a different probability at the base surface from where the pattern begins to grow. The basics of this model are shown in Fig. 7.4.


Figure 7.4: Schematic of the slippery ballistic model. As the nanoparticle (empty blue square) approaches the film, it has the possibility to stick on an occupied state (grey squares) with a given probability. In this case it continues to its final landing site.

These generalizations resulted in patterns whose local structures and universal aspects are worthy of investigation and very similar to the deposition obtained through PA-SJD. Inspired from the SBD model, a Matalb code was developed for the simu-

lation of the film growth by PA-SJD. The deposition can be performed on an (x,y)-substrate of different sizes, assuming a lattice constant equal to 3 nm. We model $TiO_2$ nanoparticles creating solid spherical objects with a fixed diameter (from TEM and AFM measurements we chose 12 nm) made up of several lattice elements. These nanoparticles fall vertically from the top of the system independently of each other. Each particles can execute a transversal motion according to their lateral speeds. A nanoparticle falls until it either touches the substrate, or gets stuck on another previously deposited particle. Different parameters, describing the sticking probabilities and the probability for lateral motion, are varied in order to reproduce the deposited film morphologies observed in the experiments. Ideal settings for lateral and vertical sticking probability are respectively 0.1 and 1. The formation of the film was simulated on two different kind of substrates: flat silicon and FTO glass (with a specific roughness calculated by AFM and reproduced on the simulation surface).

## 7.3 Film growth rate

The first analysis performed on a deposited film was the study of its height using a profilometer. For each application it is fundamental to work in a well reproducible regime, where a deposition can be easily repeated working in the same experimental conditions. With PA-SJD this regime could be easily obtained working with the operating procedure described in the experimental section of this Chapter. However it should be noted that sometimes working at the same precursor temperature could not imply having the same mass flow for titanium isopropoxide inside the plasma chamber. The deposition rate can decrease after a set of successively depositions because of the residual precursor which can choke the chopper tube of the injector. The repeatability is ensured when after one or two hours of operation the precursor injection system is refilled and cleaned up. From the analysis of the film profiles a first difference was noted for thin films grown at different position along the axis. Two typical profiles are shown in Fig.s 7.5 and 7.6.

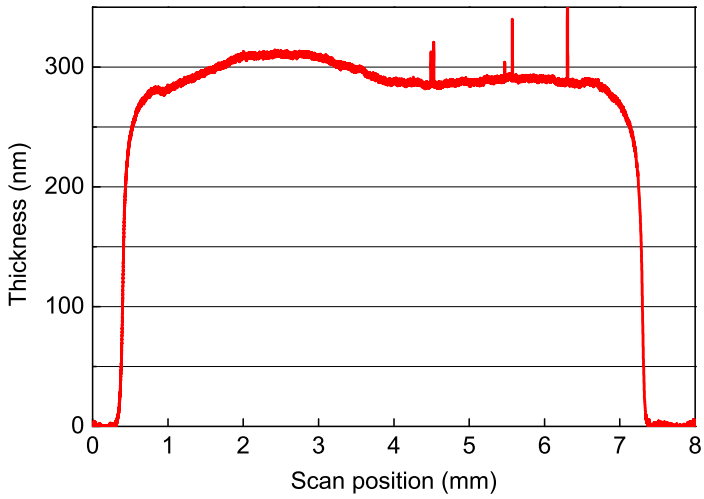


Figure 7.5: Typical profile measured with the profilometer for a $TiO_2$ thin film. The thin film was deposited at low deposition rate (about 10 nm) at 14 mm from the orifice for a rather long exposure time (about 30 min).

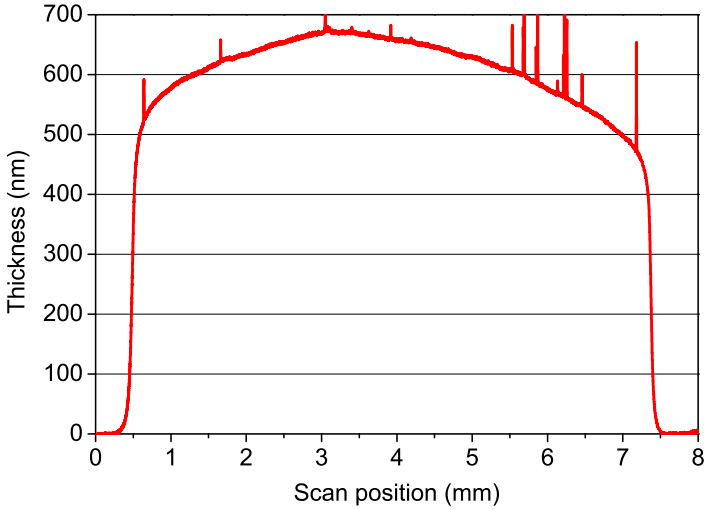


Figure 7.6: Typical profile measured with the profilometer for a $TiO_2$ thin film. The thin film was deposited at high deposition rate (200 nm) at 7 mm from the orifice for a small exposure time (about 3 min).

When a deposition is performed at a sufficiently high distance from the orifice (see e.g. Fig. 7.5), the growth rate is reduced and the profile appears flat and regular. Thin films deposited close to the orifice (see e.g. Fig. 7.6), the growth rate increases but profiles can become more rounded and non planar. This is due to the combination of different effects. First of all, when the deposition rate is low, a film may be grown with a more compact structure, due to longer diffusion lengths allowed. In addition to this, the energy of the nanoparticles (which can be range from 0.1 to 0.5 eV) is slowly increasing with the distance from the nozzle, as they are accelerated by

the drag forces of the supersonic gas carrier. More energetic particles arriving on the film have more possibilities to diffuse on the film surface. Moreover the geometry of the supersonic jet expansion has a particular radial profile which becomes more flat at increasing distances. This profile is described by [68]:

$$n(r,x) = n(0,x)\, cos^2(\theta)\, cos^2\left(\frac{\pi\theta}{2\phi}\right) \tag{7.1}$$

with $n$ gas numerical density, $r$ distance from the point where the measure is taken to the point of incidence of the flow axis, $x$ distance between the nozzle and the substrate, $\phi$ constant equal to about 1.5 for the considered gas mixture, and $\theta$ angle given by:

$$\theta = arctan\left(\frac{r}{x - x_0}\right) \tag{7.2}$$

where $x_0$ is the distance between the nozzle and the point from which the flux lines would originate if it was a point source (see Fig. 7.7).

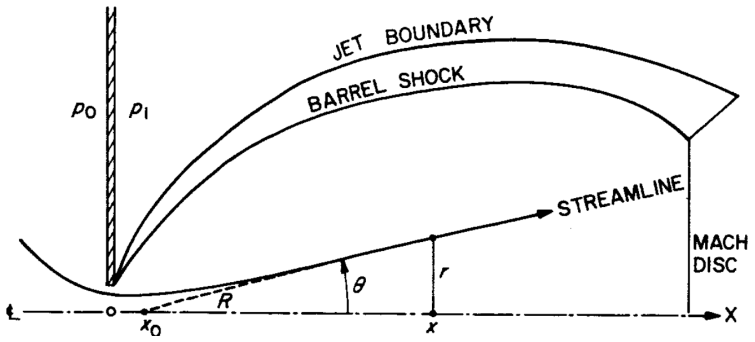


Figure 7.7: Sketch of the flow geometry from [68].

The growth rate was measured using the average height of the film divided the film exposure time. Different growth rates were observed performing depositions at different positions along the jet. Figure 7.8 shows the average deposition rates obtained at 14, 9 and 7 mm of distance from the nozzle orifice at constant precursor temperature of 44°C.

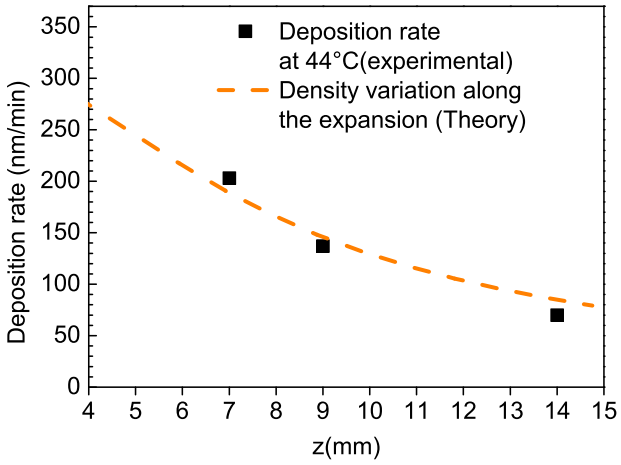


Figure 7.8: Average deposition rate at three different positions along the jet axis at constant precursor mass flow (obtained using the same precursor tank temperature of 44°C). The experimental data can be fitted by the isentropic jet expansion law which was fitting well the $TiO_2$ seeds density along the expansion, multiplied by a single fit parameter.

The growth rate is both linearly dependent from the precursor mass flow (within the temperature range from 40 to 50 °C) and related to the isentropic density distribution along the axis centerline, as shown in Fig. 7.8. The predicted isentropic density, displayed as an orange dashed line in the graph, is well fitting the film growth rate. Depositions rates of the order of hundreds nm/min are highly competitive and can be further increased by raising the precursor temperature.
Another important aspect of the film growth by PA-SJD, is how the structure can be affected from non parallel gas streamlines. The deposition angle $\theta$ displayed in Fig. 7.7 influences the growth of the film. Since the energies involved in our depositions can be considered rather low, incoming nanoparticles tend to stick where they arrive on the surface of the film. This give rise to very important shadowing effects, especially for thin films deposited very close to the nozzle and over wide areas. In particular far from the film center (more than 10 mm distance) the effect of the jet streamlines orientation becomes significant and the film morphology is no longer expected to be structured in vertical columns, but there is a growth angle $\beta$ which is related to the deposition angle $\alpha$ as shown in Fig. 7.9.

$$tan(\alpha) = 2tan(\beta) \tag{7.3}$$

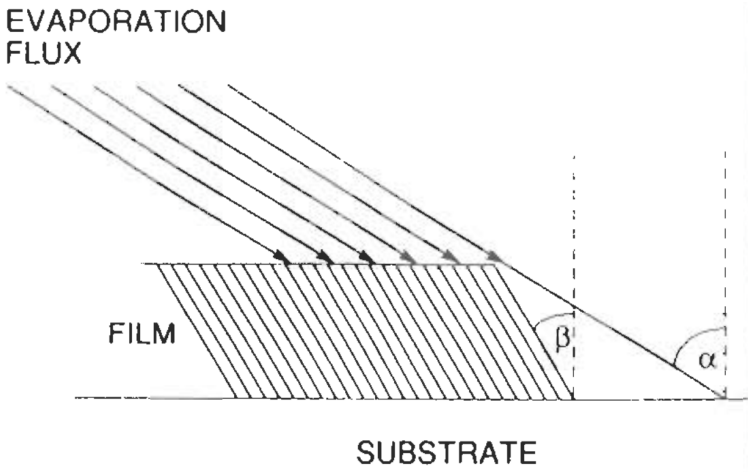


Figure 7.9: Deposition geometry describing film growth at an angle $\alpha$, situation which takes place in PD-SJD for the region of the deposit far from the center, where the streamlines of the supersonic expansion can not be considered straight. The results is the formation of columnar structures with an angle $\beta$.

The deposition over wide areas seems an actual limitation of PA-SJD. In Chapter 7 the side effects of the supersonic jet were studied at 5 mm from the centerline, showing a highly different radial distribution for the light gas carrier and the heavier $TiO_x$ products. The retention of high masses within the center of the axis and the angular effects just showed clearly imply that for deposition ares greater than those studied in this work (5×5 mm or 7×7 mm) may exhibit a radial dependency of the thin film chemical structure and morphology.
These limitations can however be overcome in different ways. The up-scaling of the reactor, in all its component, can partly solve some of these issues increasing the jet area or allowing the use of more than one nozzle, covering easily greater areas. In this work some deposition-tests were performed over a great area just gradually moving vertically the substrate by few millimeters (generally 5), at time step of 2-4 minutes. The nozzle ending orifice was replaced by a slit, whose height and width (respectively 20 and 8 mm) were designed to give a conductance similar to the one of the circular orifice. FTO-glass substrates were inserted on a particular holder, fixed to a movable vertical bar as shown in Fig. 7.10.

Figure 7.10: Photography of the $TiO_2$ thin film deposition over a wide area, moving the sample vertically.

This procedure was repeated moving back and forth the substrate a desired amount of times (depending on the desired film thickness) at a distance of 6 mm from the nozzle slit. Figure 7.11 shows the result for a 80×5 mm thin film, which was exposed to the seeded jet for few minutes at 41°C, with a small precursor flow.

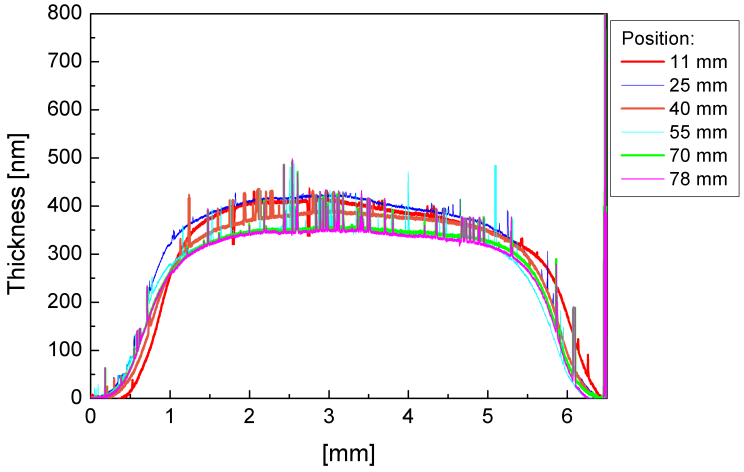


Figure 7.11: Profilometer scans performed at different position of a 80× 5 mm area of $TiO_2$ thin film. The thin film was deposited at low deposition rate at 6 mm from the nozzle slit, moving the substrate vertically by 5 mm every 2 minutes back and forth.

The whole area was successfully covered with a nearly uniform $TiO_2$ nanostructured deposition having an average height of 350 nm. Increasing the precursor flow using temperatures of 50°C it was possible to boost the deposition rate, this was done

depositing over a smaller area of 40×5 mm, obtaining a thin film with a thickness of the order of few $\mu$m.

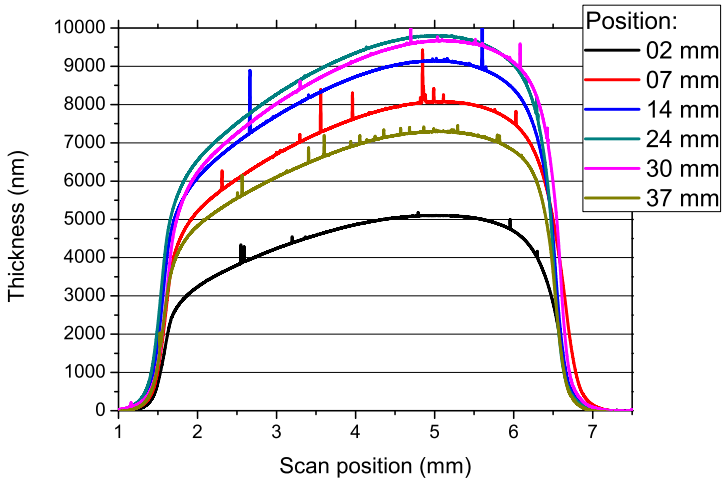


Figure 7.12: Profilometer scans performed at different position of a 40× 5 mm area of $TiO_2$ thin film. The thin film was deposited at high deposition rate at 6 mm of distance from the nozzle slit, moving the substrate vertically back and forth twice.

Figure 7.12 shows the profiles of the high deposition rate film. The area is fully covered, even if the substrate was not perfectly perpendicular to the jet. The deposited area is not well uniform, especially over the top and bottom borders, however the results are very promising and denote the possibility to cover great areas with high deposition rates.

## 7.4 FTIR analysis

From the measurement of the mass spectra along the seeded supersonic plasma jet, it was noted both that the precursor was often not fully dissociated and that organic impurities were present and attached to titanium seeds. However working with $TiO_2$ nanostructured films it may be convenient not to fully dissociate the precursor, which has the tetrahedral motif of a $TiO_4$ structure. In addition to this, during each deposition oxygen emission lines are well observable from the optical emission spectra, even if reduced. This suggests that radical oxygen decreases injecting the precursor at the considered flow rates but is not fully depleted. Further increasing the radical oxygen density might not result directly in a stronger dissociation of the titanium isopropoxide inside the plasma chamber. A detailed analysis of the chemical composition of the films was possible thanks to FTIR spectroscopy. Figure 7.13 shows the FTIR spectra for the titanium isopropoxide precursor.

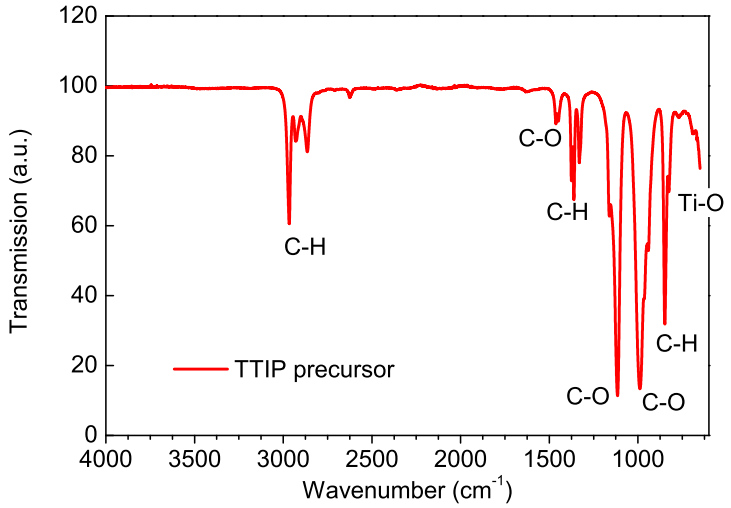


Figure 7.13: FTIR spectra (650-4000 $cm^{-1}$) of titanium isopropoxide liquid precursor.

This spectra contains traces of the different chemical bounds present in the TTIP monomer ($Ti(OCH(CH_3)_2)_4$). C–H stretching are well distinguishable at 2960, 2924 and 2864 $cm^{-1}$. Also $CH_3$ bending can be identified at 1366, 1318 $cm^{-1}$, while $CH_3$ rock at 844 $cm^{-1}$. The peak located at 1450 $cm^{-1}$ is typical of C–O vibrations. C-O stretching are also observable at 1114 and 982 $cm^{-1}$ Ti-O stretching can be spotted over 635 $cm^{-1}$ (it is reported in literature at 626 $cm^{-1}$). The spectra measured for the depositions were usually very similar to each other, a typical spectrum measured to a $TiO_2$ thin film, as deposited, is shown in Fig. 7.14.

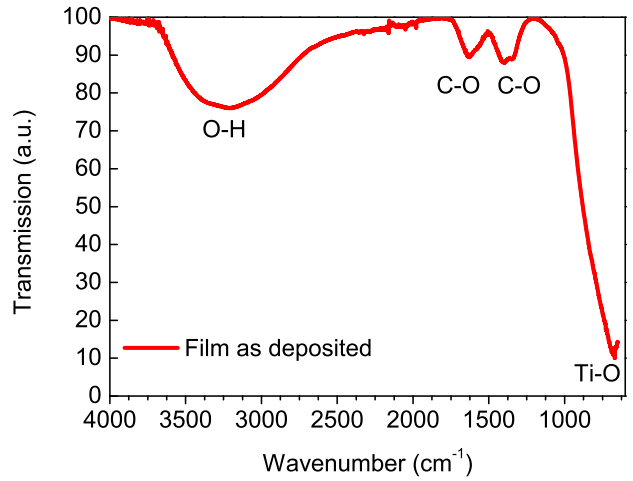


Figure 7.14: FTIR spectra (650-4000 $cm^{-1}$) of a typical $TiO_2$ film as deposited by PA-SJD.

This spectrum has many differences from the TTIP precursor. In particular there is a very broad band in the spectral ranges between 3000 and 3500 $cm^{-1}$ where the

OH stretching vibrations of OH groups are present. Here the CH stretching are missing, as the precursor has been successfully dissociated and oxidized. Two wide peaks appears at 1637 and near 1380 $cm^{-1}$ which are characteristic for conjugated C–O vibrations to a transition metal. The other peak which can be observed is the Ti-O stretching which is shifted to 700 $cm^{-1}$, as happens when organic groups are attached to the Ti-O molecule. From this analysis it seems that this spectrum is free of CH groups but still many organic groups (C-O and O-H) are present.

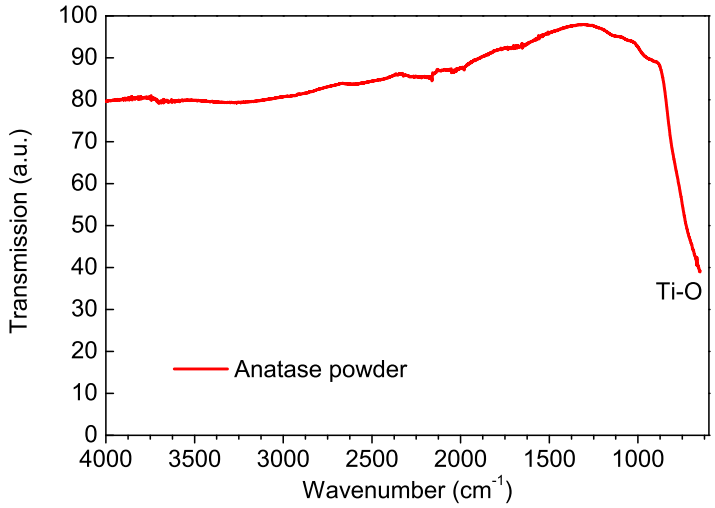


Figure 7.15: FTIR spectra (650-4000 $cm^{-1}$) of $TiO_2$ anatase powder.

Figure 7.15 shows a FTIR spectrum measured for a pure $TiO_2$ anatase powder. Here the only peak distinguishable is the Ti-O stretching below 650 $cm^{-1}$. A very similar results is obtained for each film after the thermal annealing at 500°C, as it can be observed in Fig. 7.16.

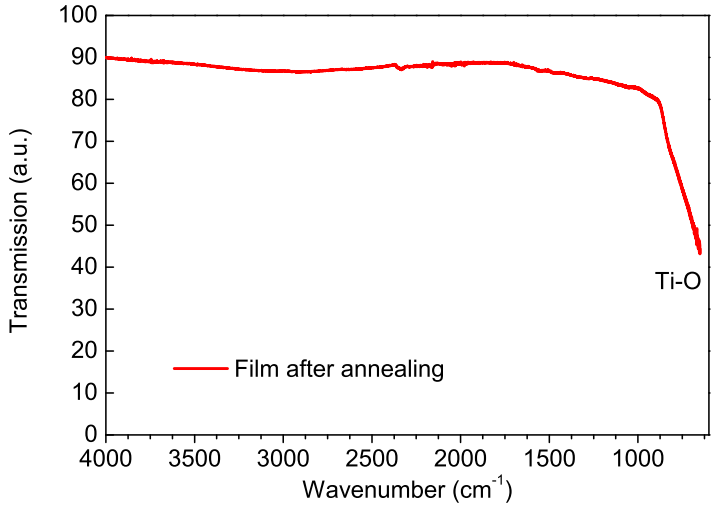


Figure 7.16: FTIR spectra (650-4000 $cm^{-1}$) of a typical $TiO_2$ film by PA-SJD after annealing at 500°C.

After the annealing, the FTIR spectra display only the Ti-O peak below 650 $cm^{-1}$, as for the pure anatase powder. The thermal treatment can help to obtain pure $TiO_2$ films, fully removing the organic groups. The annealing is also fundamental for modifying the crystalline structure of titanium dioxide. Figure 7.17 shows the result of a raman spectroscopy experiment performed on a PA-SJD deposition.

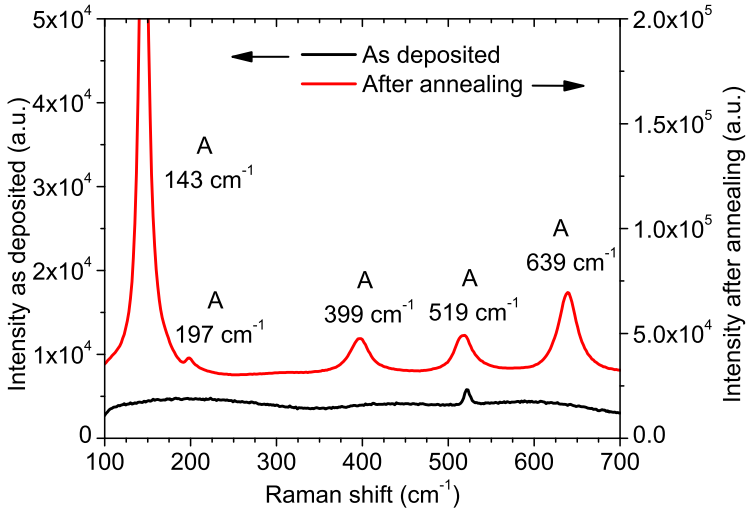


Figure 7.17: Raman spectrum of a typical $TiO_2$ film before (black line) and after (red line) annealing at 500°C (band range between 100 and 700 $cm^{-1}$). Anatase characteristic peaks are labeled with letter A.

Different peaks can be observed and related to an anatase structure, which is the most desirable for photovoltaics applications due to the higher electron mobility which can normally be achieved.

## 7.5 Film morphology

$TiO_2$ thin films were characterized by means of atomic force microscopy for a quick evaluation of their morphological surface properties. Figures 7.18 and 7.19 show two AFM scans over an area of 2000×2000 nm on different films deposited at the same experimental conditions after the annealing.

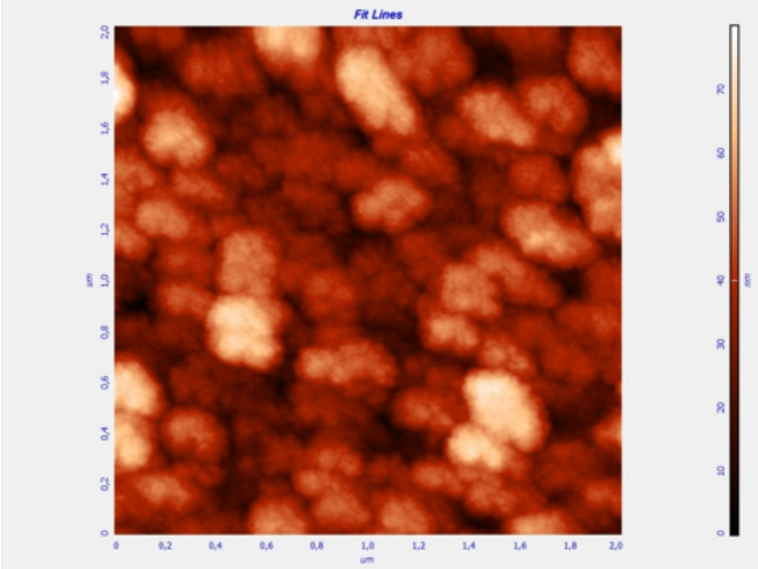


Figure 7.18: A 2000×2000 nm AFM image of a $TiO_2$ thin film deposited on a FTO glass substrate. The effect of shadowing due to surface roughness is observable.

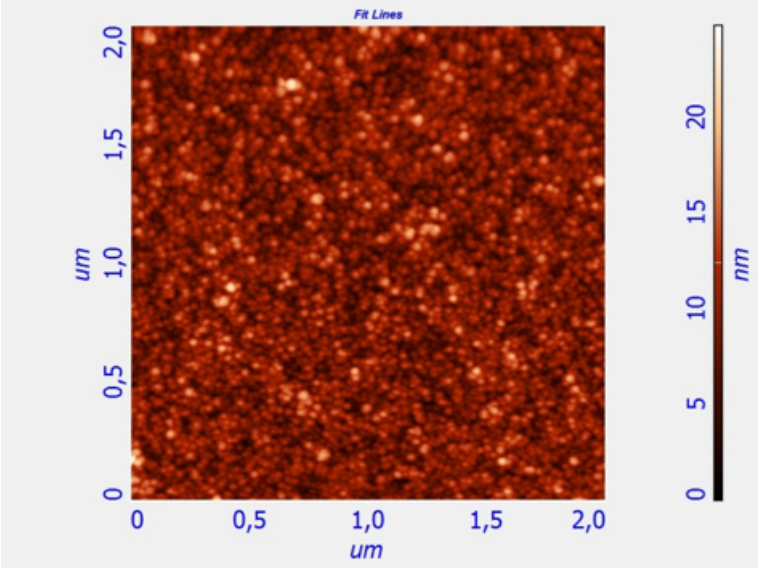


Figure 7.19: A 2000×2000 nm AFM image of a $TiO_2$ thin film deposited on a Silicon. The film looks more compact and flat.

The sample analyzed in Fig. 7.18 was deposited on the FTO glass substrate, while the one shown in Fig. 7.19 on a silicon substrate. The different surfaces reflect different films structures: the FTO glass has a roughness very high if compared to the silicon, which is almost flat. This results in a different growth of the films, in the first case shadowing effects are important and the film surface maintain a rms roughness of about 10 nm, which does not seem to depend on the film thickness. Thin films deposited on silicon exhibit a rms roughness between 2 and 3 nm.
Figure 7.20 shows an AFM scan performed over an area of 500×500 nm on the $TiO_2$

film deposited on silicon shown above.

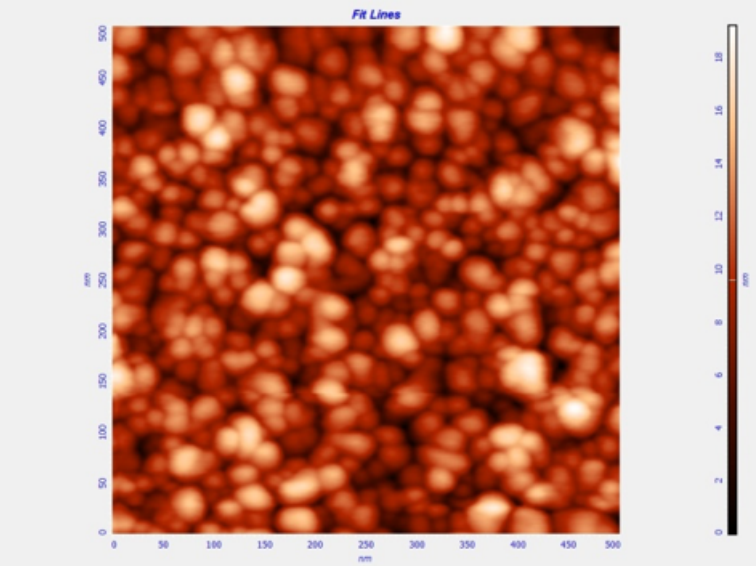


Figure 7.20: A 500×500 nm AFM image of a $TiO_2$ thin film deposited on a Silicon. The nanoparticles grains can be measured and a particle diameter can be extracted.

In this scale it is possible to evaluate the grain size, using the relation previously given in the experimental chapter:

$$r = \frac{(r_c/2)^2}{R} \tag{7.4}$$

where $r$ is the radius of a spherical object, $R$ is the curvature radius of the probe tip (10 nm) and $r_c$ the radius measured by AFM of the spherical object. From the evaluation of the different spheres observed in Fig. 7.20 it is possible to evaluate for example a particle diameter of 12.1 ± 5.

This analysis was repeated in the other AFM scans observing particle diameters between 12 and 15 nm both on silicon and FTO-glass substrates. No evident difference or trend could be observed for depositions performed at 7, 9 or 14 mm of distance from the orifice. This is also a consequence of the effect previously estimated from the Weiel model of nucleation in the previous chapter. As the gas expands supersonically, both temperature and density decreases. The decrease of temperature favor the nucleation of clusters, while the decrease of density clearly reduces the probability of aggregation. Thus as the distance from the nozzle increases these two phenomena cancel each other out, providing a constant maximum cluster dimension, which is mainly a function of the precursor density.

Selected samples were also analyzed by a scanning electron microscope. Figures 7.21 and 7.22 shows SEM (Scanning Electron Microscopy) images of PA-SJD titanium dioxide thin film section after annealing. This deposition was performed on a silicon substrate.

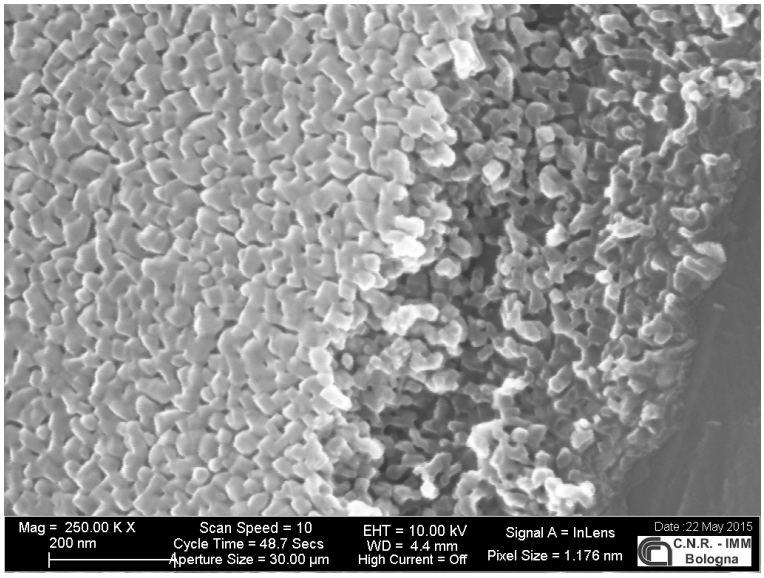


Figure 7.21: SEM image of a thin film section deposited on a silicon substrate.

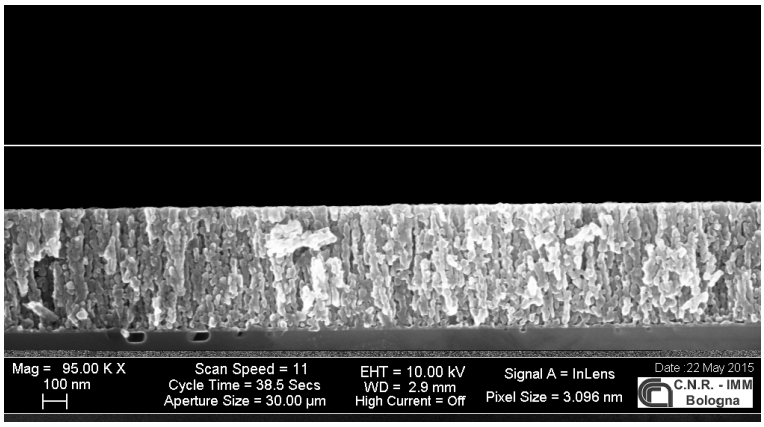


Figure 7.22: SEM image of a thin film section deposited on a silicon substrate.

Stable hierarchical nanostructures appear forming vertical columns with fine grains. A certain film porosity can also be envisaged by looking at the film section. Both these properties are ideal for the production of nanostructured photoanodes: the film porosity is vital for the absorption of the chemical dye molecules which are to be inserted in the film. The vertical structure sets a preferred direction for the electrical current when flowing across the solar cell.

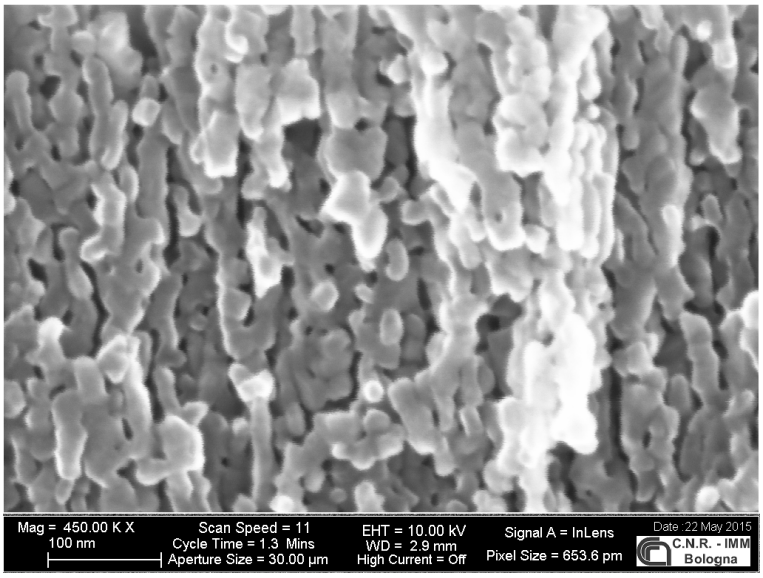


Figure 7.23: SEM image of a thin film section deposited on a silicon substrate.

Figure 7.23 shows a high resolution section of the thin film, from which it was possible to accurately estimate an average particles diameter. In this sample the average diameter was $15 \pm 4$, in agreement with those measured by AFM. Few TEM images were also obtained for some samples deposited on FTO-glass substrates, a typical image is shown in Fig. 7.24, however the film grain is not fully appreciable due to the low resolution of the instrument.

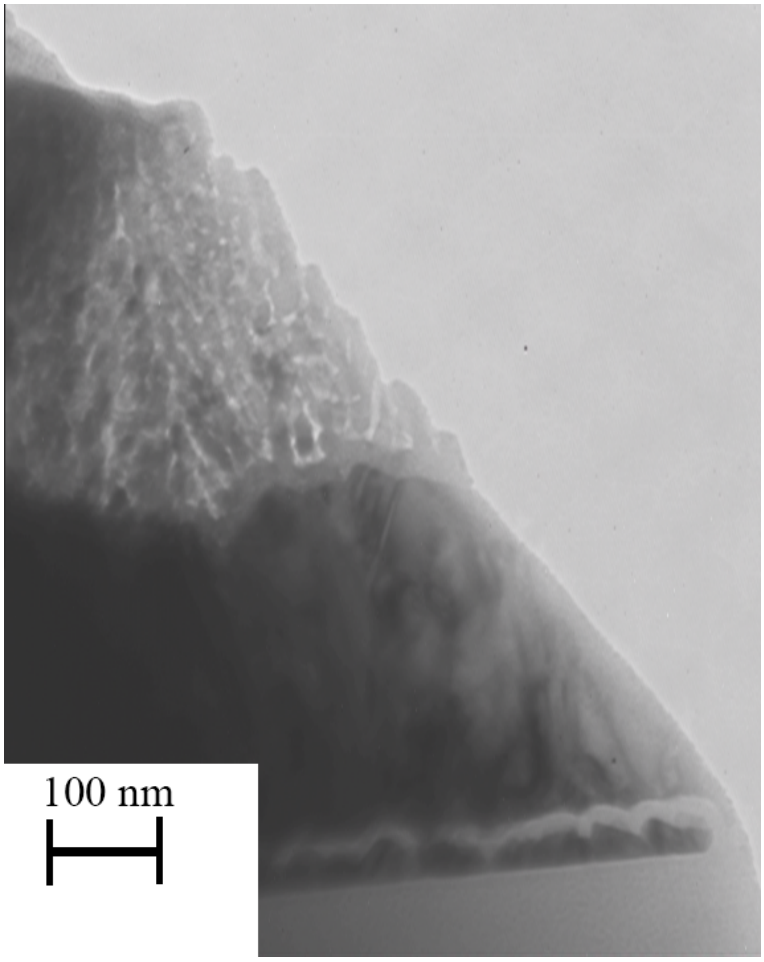


Figure 7.24: TEM image of a thin film section deposited on FTO-glass substrate.

Looking at the substrate in Fig. 7.24 it can be well understood how its roughness can influence the growth of thin films. All these information were employed to develop and set a simulation code for the growth of thin films by PA-SJD. In Fig.s 7.25 and 7.26 a section of two different simulations is shown where the influence of the substrate roughness can be understood.

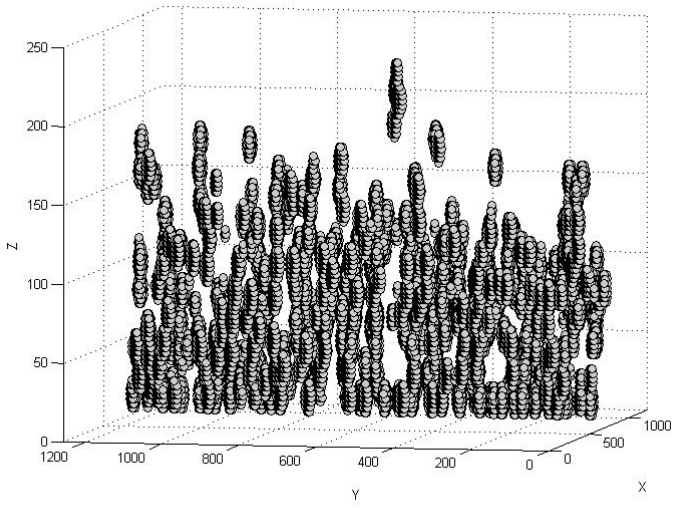


Figure 7.25: Cross section displaying a detail of a film growth simulation performed on a flat substrate (silicon). The spheres represent titanium nanoparticles assembled and forming a thin film.

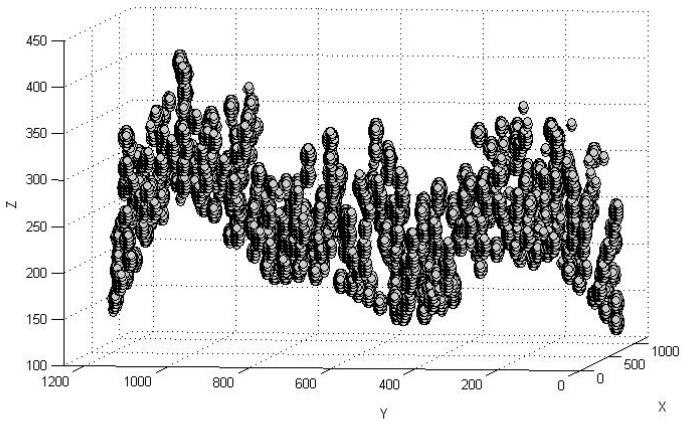


Figure 7.26: Cross section displaying a detail of a film growth simulation performed on a flat substrate with a given roughness (we used the roughness measured by AFM on FTO glass). The spheres represent titanium nanoparticles assembled and forming a thin film.

The film deposited on silicon (Fig. 7.25) exhibits a more compact and columnar structure, while the film deposited onto rough surface appears more irregular as the growth is influenced by shadowing effects. Film of about few microns can be simulated depositing about $10^6$ nanoparticles, an example is shown in Fig. 7.27, where a 200 nm thin film was simulated in a 500×500 nm area.

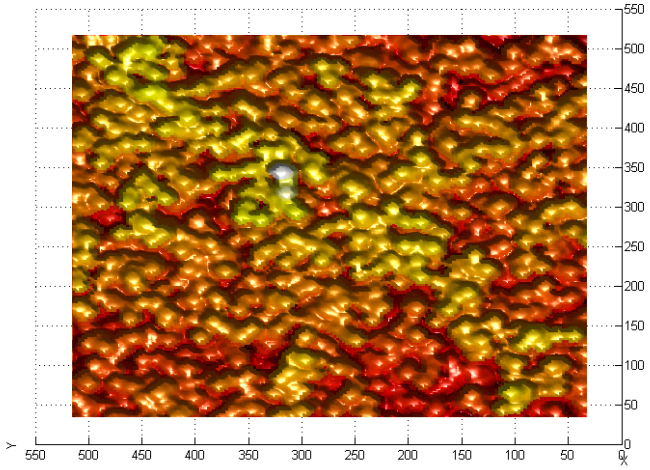


Figure 7.27: Simulation of a $TiO_2$ deposition on silicon on a 500×500 nm area.

From these simulations it was possible to estimate a rms roughness (taking into account the relation between the grain radius and the radius measured by AFM) which was compared with the experimental results obtained by AFM. The film rms roughness for a simulation on a flat substrate is near to 2-3 nm, while it is between 10 and 12 nm for deposition on a FTO glass substrate. This results are highly encouraging and set the steps for a controlled production of thin films. Using the predictions of such simulations it is possible to design the nanostructure of our thin films.

## 7.6 Summary and conclusions

$TiO_2$ nanostructured thin films were deposited by PA-SJD and characterized. Films can be grown at different deposition rates, depending on the precursor mass flow or on the distance of the substrate from the nozzle. The growth rate ranges from few nanometers per minute to few hundreds. The growth rate along the supersonic expansion scales with the isentropic density relation for the supersonic jet. Depositions were also performed over wide areas using a movable substrate.

FTIR spectroscopy was used to study the chemistry of the films. The typical films deposited by PA-SJD exhibit also absorption lines which can be related to C-O and O-H bounds. A thermal annealing performed at 500°C can successfully remove any organic impurity also setting the crystalline structure of the $TiO_2$ to anatase, which is the most desirable for most applications.

The morphology of the thin films was characterized by AFM, SEM and TEM imaging. The AFM was employed to characterize the film surface, defining its rms roughness and the typical dimension of the grains. A great difference could be observed for films grown on different substrates. When the substrate is flat (silicon) the film

structure is more compact and the roughness limited (2-3 nm), otherwise when the substrate has a high roughness (FTO glass) the thin films will be subject to shadowing effects and exhibit a similar roughness (10-13 nm). Despite these differences, for almost every sample studied the average nanoparticle diameter was evaluated between 12 and 15 nm.

SEM and TEM images of some selected samples confirmed a vertical nanostructure with grains diameter about 15 nm. A certain porosity could also be observed in thin films which were studied after the annealing process. A simulation code was developed to perform simulations of the film growth, using a slippery ballistic model. The typical rms roughness which can be calculated from simulation performed on flat substrate and on a substrate with the roughness of the FTO glass used were found in excellent agreement with the values measured experimentally.

CHAPTER

# 8

# CONCLUSIONS

Plasma assisted supersonic jet deposition was presented as a deposition technique and a characterization of different features of the deposition process were studied. The analyses reported in this Ph.D. thesis give a detailed theory and understanding of the physics involved in this reactor. The results presented set the next step for further improvements of this techniques to achieve a greater control on the thin film growth also allowing the possibility to develop films for new applications.
In Chapter 3, the physics of the supersonic jet is described and studied in the absence of plasma, for the argon-oxygen gas binary mixture at the transitional flow regime. The results for the neutral gas case are in good agreement with the viscous isentropic model. However no shock compression can be spotted over the Mach disk, as it is commonly observed in higher pressure jets; instead we observed a smooth transition to a subsonic regime, in which the background density values are reached within about 3 gas mean free path lengths from the Mach disk location. The transition is denoted by the detachment from the predicted isentropic expansion equation and its location was in fair agreement with the predicted position of the Mach disk in an extended range of pressure ratios. This smooth transition observed for the neutral species is highly desirable for thin film deposition applications since it can prevent the sudden stop of nanoparticles over the Mach disk and reflected shocks over the sample which can affect the film growth. Gas separation phenomena have been observed along the jet. With the QMS it was possible to measure the Ar enrichment over the supersonic jet axis. A maximum excess of about 5% was obtained for argon respect to oxygen. In the case of the plasma we observed a supersonic jet containing both neutral and positively charged particles.

In Chapter 4 the analysis is focused on the plasma inside the first chamber and in the supersonic jet.The measurements of time series for voltage and current across the plasma antenna clearly set the E-H mode transition for the considered gas mixture at 175 W and ensure a more efficient power transmission after this power value. Rms voltages of 800 V and currents about 2 A can be observed at 450 W, the RF power level which was chosen for performing PA-SJD deposition.
Optical emission spectroscopy was used to reveal the radiation emitted from the plasma at different pressure values, argon-oxygen concentrations and RF power level. The use of this diagnostic allowed the identification of the main emitting species (Ar and O in this case) from the plasma and denoted a significant increase in charge density after the E-H mode transition. At increasing oxygen in the plasma chamber, this transition is delayed to higher power level, making more complex the establishment of a fully inductive regime. However it was shown that an high production of radical oxygen, required for an effective precursor dissociation, can be achieved also raising the argon pressure in the discharge. A collisional-radiative model for the argon emission lines was successfully employed to estimate the plasma temperature as a function of the RF-power input. The temperature decreases from 1.25 to 1.03 eV as the RF-power is raised from 75 to 450 W in a common argon-oxygen discharge at 8 Pa of total pressure (being oxygen to argon concentrations 3 to 2).
A RF compensated Langmuir probe was introduced inside the plasma chamber to measure the main plasma parameters. Unfortunately the RF-noise on the probe was too high, especially in the H-mode. The measurements of the characteristic Langmuir curve was thus highly perturbed for positive probe potential values. However the ion saturation current could have been extracted from negative part of the Langmuir curve. This value was converted in an approximate density using the electron temperature estimated by OES, giving charge densities increasing from 1 $10^{15}$ to 1 $10^{16}$ $m^{-3}$, as the RF-power was raised from 45 to 450 W.
The characterization of the jet profiles was performed using a quadrupole mass spectrometer. During each plasma measurement also ion fluxes and their energy distribution functions were measured. We observed a supersonic jet containing both neutral and positively charged particles. The neutral gas even in the presence of a plasma exhibits a very similar behavior to the gas case. Neutral Ar and $O_2$ expand following the isentropic model without ending shock compression. This proves that the isentropic model is still valid and the expansion is still adiabatic for neutrals even in the presence of a plasma. Supersonic jet ion spectra are dominated by molecular oxygen ions and argon ions. However different peaks can be related to small impurities concentrations. Ion mass and energy spectra gave an insight on the ion fluxes along the jet. Ions along the expansion can be measured with energies ranging from 0 up to 12 eV. The energy spectra of the impurities were observed at a mono-energetic energy distribution peaked about 8 eV. Argon and molecular oxygen ions instead show different energies, due to a more pronounced collisional nature and

to charge transfer reactions. Inside the supersonic jet, a very intense low energy peak (about 1 eV for $Ar^+$, 2 eV for $O_2^+$) can be observed in the spectra, along with a moderate high energy section. After the nozzle, inside the supersonic jet, there is an expansion also for the ions, which resemble the isentropic expansion of the neutrals. Across the Mach disk position, the ion energy distribution changes greatly: while the low energy peak reduces itself and shift to 0 eV, the high energetic peak increases. An increase of ion flux could be ascribed to the higher diffusivity of electrons respect to ion species. A positive charge space region could arise in correspondence with the Mach disk. This phenomenon denotes the formation of a space charge region just after the end of the supersonic jet which could originate a potential difference, responsible of enhancing the ion fluxes. This occurs for the highest part of the ion energy spectrum. The presence of high energy fluxes has interesting consequences on ion bombardment processes during the thin film formation and growth. IEDFs were also measured at a fixed position for different pressure ratios, showing the effect of collisions on their energy. The energy distribution functions do not seem to exhibit particular variation in their shape at different RF-powers.

In Chapter 5 the IEDFs are further studied by developing a simulation code to reproduce them, from first principle calculations. An experimental characterization of ion energy distribution functions was carried out along a low-pressure argon supersonic plasma jet by directly measuring the ion fluxes at different energies with a QMS. The energies observed were distributed up to typically 10 eV and exhibit different distribution functions along the jet expansion axis. In particular, as the gas expands supersonically two peaks are distinguishable around 2 and 8 eV, while outside of the supersonic region (i.e. after about 25 mm from the initial expansion point) the low-energy peak is shifted down to thermal energies ($\simeq$ 0.1 eV). These results suggest that the ions energy evolves in a supersonic jet as in a long pre-sheath region. Starting from the plasma at a potential of about 8 eV, each ion can collide inside the jet reducing its energy before being detected by the spectrometer. Along the expanding jet there is a pre-sheath plasma at a nearly constant potential $V_{\text{jet}} = 2$ eV. Among different collisional phenomena elastic scattering and charge transfer events are the dominant processes.

Starting from this experimental evidence, a model for the simulation of the ion energy distribution function in a supersonic plasma jet was developed. It is possible to simulate the exact dynamics of one ion at a time, exploiting their very low density, moving along the supersonic jet by integrating the equations of motion from first principles at small time-steps (10 ps). We consider only $Ar^+$-Ar collisions which are described by a 12-4 Lennard-Jones potential, thus including the charge-induced dipole interactions represented by the $r^{-4}$ term. In the proposed model, each momentum transfer collision can result either in a simple elastic scattering process or in a charge transfer event with a well defined probability (close to 1/2 for interaction distances smaller than a cutoff distance, $\sim$ 0.4 nm). The dynamics of about 1000

ions was simulated from $z = 5$ mm up to $z = 20$ mm, covering most of the spatial range of the expanding jet.

The agreement between the simulations and the experimental results is very good, thus validating the model assumptions and approximations used. In addition to these features, the phenomenology of the scattering events was further studied by analyzing the energy loss in each collision and calculating the ionic mean free paths also in the presence of charge transfer events. In this way, we can distinguish processes in which there is a charge transfer or not. We find that charge transfer collisions occur in nearly 50% of the total number of scattering events. The global effect of charge transfer mechanism on the final distribution functions is found to be quite significant. Indeed, simulations performed without charge exchange reproduce the observed IEDFs only partially, while the inclusion of charge transfers favors medium-low ionic energies in better agreement with experiments. In addition to this, the mean free paths relative to general collision events and those displaying charge transfers can be calculated separately, thus allowing to estimate their respective cross sections, 9 $10^{-19}$ m$^2$ and 5.4 $10^{-19}$ m$^2$, respectively, in very good agreement with estimates known in the literature.

In Chapter 6 the plasma inside the first chamber and the supersonic jet is studied when creating the titanium seeded jet. Optical emission spectroscopy was employed during each measurement to control the mass flow of the precursor. From the optical spectra, when the precursor is injected, it is possible to identify different products of the titanium isopropoxide dissociation and oxidation. As the temperature of the precursor tank is raised, the mass flow of the precursor linearly increases. A similar trend was confirmed by the QMS measurements observing the titanium products along the jet. Sampling neutral gas species and ions at different distances from the nozzle it was possible to gain an insight on the precursor dissociation and the components also along the supersonic jet. Many molecules of partly dissociated precursor could be observed. The study of the supersonic jet profiles for the $TiO_x$ seeds was then performed. Titanium nanoparticles follow the isentropic expansion, as the light gas carrier, until the Mach disk location, then they maintain their density also over long distances. This is due to an inertial effect, which maintain the heavier species near the jet centerline. This is a particular interesting feature because it allows to perform thin film deposition also far from the nozzle, where the jet is no longer supersonic. Each $TiO_x$ seed can also be measured as an ion in the jet. The ion energy distribution functions of these species are very particular as they show a wide energy spectrum centered about 5 eV. It is also very intense the ion flux enhancement for heavier seeds after the Mach disk. Similar measurements were also performed shifting the expansion radially by 5 mm from the mass spectrometer orifice. This allowed a study of jet off from its axis, still in a region which is relevant for thin films deposition. The enrichment of heavier species in the more central part of the jet is quite evident, as in the profile for the neutral components the gas carrier

still show a expansion whereas the abundance $TiO_x$ seeds studied drops to zero when the spectrometer is close to the nozzle as they are retained over the central part of the jet. A similar effect can also be observed for the ions, which can be found only at lower energies.

Finally in Chapter 7 $TiO_2$ nanostructured thin films deposited by PA-SJD are characterized. Films can be grown at different deposition rates, depending on the precursor mass flow or on the distance of the substrate from the nozzle. The growth rate ranges from few nanometers per minute to few hundreds. The growth rate along the supersonic expansion scales with the isentropic density relation for the supersonic jet. Depositions were also performed over wide areas using a movable substrate.

FTIR spectroscopy was used to study the chemistry of the films. The typical films deposited by PA-SJD exhibit also absorption lines which can be related to C-O and O-H bounds. A thermal annealing performed at 500°C can successfully remove any organic impurity also setting the crystalline structure of the $TiO_2$ to anatase, which is the most desirable for most applications.

The morphology of the thin films was characterized by AFM, SEM and TEM imaging. The AFM was employed to characterize the film surface, defining its rms roughness and the typical dimension of the grains. A great difference could be observed for films grown on different substrates. When the substrate is flat (silicon) the film structure is more compact and the roughness limited (2-3 nm), otherwise when the substrate has a high roughness (FTO glass) the thin films will be subject to shadowing effects and exhibit a similar roughness (10-13 nm). Despite these differences, for almost every sample studied the average nanoparticle diameter was evaluated between 12 and 15 nm.

SEM and TEM images of some selected samples confirmed a vertical nanostructure with grains diameter about 15 nm. A certain porosity could also be observed in thin films which were studied after the annealing process. A simulation code was developed to perform simulations of the film growth, using a slippery ballistic model. The typical rms roughness which can be calculated from simulation performed on flat substrate and on a substrate with the roughness of the FTO glass used were found in excellent agreement with the values measured experimentally.

# COURSES, CONFERENCES AND PUBLICATIONS

**Courses attended:**

- Experimental methods for the investigation of systems at the nanoscale, Scuola di dottorato in fisica Astrofisica e fisica applicata dell'Università degli studi di Milano, Prof. Alberto Vailati (6 cfu-30 hours). Exam on 15 July 2013.
- Connecting with English (66 hours), J. Weekes. February – December, 2013.
- Corso di dottorato su informatica e computazione, dott. Andrea Biancini e dott. Luca Prete, Scuola di dottorato in fisica e astronomia dell'Università degli studi di Milano-bicocca, (3 cfu-20 hours). Exam on 12 September 2014.
- Metodi Bayesiani (3 cfu-16 hours), E. Milotti, Scuola di dottorato in fisica e astronomia dell'Università degli studi di Milano-bicocca, 3-6 June 2014. Exam on 14 December 2014.

**Schools:**

- Nanoindentation: from theory to practice, 13 May - 14 May 2013, Università degli Studi Roma Tre, prof. George M. Pharr, 12h.
- 11th Carolus Magnus Summer School on Plasma and fusion energy physics, August 26 - September 6 2013, Physikzentrum, Bad Honnef, Germany. A seminar about this school was given on 26 September 2013.

**Conferences:**

- 13th High-Tech Plasma Processes Conference, 22–27 June 2014, Toulouse, France. With poster and oral contribution.

**Scientific publications on peer-reviewed journals:**

- Fattorini L, Barni R, Caldirola S, Riccardi C 2014 "Coherent Structures of Plasma Density in a Simply Magnetized Torus", IEEE Transactions on Plasma Science, Volume:PP, Issue: 99.

- Caldirola, S., Barni, R.,& Riccardi, C. (2014). Characterization of a low pressure supersonic plasma jet. JOURNAL OF PHYSICS. CONFERENCE SERIES, 550, 012042.

- Caldirola, S., Roman, H.,& Riccardi, C. (2014). Ion energy distribution functions in a supersonic plasma jet. JOURNAL OF PHYSICS. CONFERENCE SERIES, 550, 012043.

- Caldirola, S., Barni R., Roman H. E.& Riccardi C. (2015) "Mass spectrometry measurements of a low pressure expanding plasma jet", J. Vac. Sci. Technol. A 33, 061306.

- S. Caldirola, H.E. Roman, C. Riccardi, "Ion Dynamics in a Supersonic Jet: Experiments and Simulations" submitted to Physical Review E.

- R. Barni, S. Caldirola and C. Riccardi ,"Note: Emission Spectroscopy Tomography as a Diagnostics for Magnetized Plasma Column Profiles" submitted to Review of Scientific Instruments.

- Dell'Orto, E. C., Caldirola, S., Roman, H. E.,& Riccardi, C. (2015). "Nanostructured TiO2 Film Deposition by Supersonic Plasma Jet Source for Energetic Application", 2nd International Congress on Energy Efficiency and Energy Related Materials (ENEFM2014) (pp. 349-355). Springer International Publishing.

# BIBLIOGRAPHY


[1] D.P. Macwan, PragneshN. Dave, and Shalini Chaturvedi. A review on nano-tio2 sol–gel type syntheses and its applications. *Journal of Materials Science*, 46(11):3669–3686, 2011.

[2] R. Messier, A. P. Giri, and R. A. Roy. Revised structure zone model for thin film physical structure. *Journal of Vacuum Science Technology A*, 2(2):500–503, 1984.

[3] Ana Borrás, José Cotrino, and Agustín R. González-Elipe. Type of plasmas and microstructures of tio2 thin films prepared by plasma enhanced chemical vapor deposition. *Journal of The Electrochemical Society*, 154(12):P152–P157, 2007.

[4] Neeraj Dwivedi, Sushil Kumar, and Hitendra K. Malik. Nanostructured titanium/diamond-like carbon multilayer films: Deposition, characterization, and applications. *ACS Applied Materials & Interfaces*, 3(11):4268–4278, 2011. PMID: 21942626.

[5] B. Dick, M. J. Brett, and T. Smy. Investigation of substrate rotation at glancing incidence on thin-film morphology. *Journal of Vacuum Science Technology B*, 21(6):2569–2575, 2003.

[6] Ilaria Biganzoli, Francesco Fumagalli, Fabio Di Fonzo, Ruggero Barni, and Claudia Riccardi. A Supersonic Plasma Jet Source for Controlled and Efficient Thin Film Deposition. *Journal of Modern Physics*, 03(10):1626–1638, 2012.

[7] F. A. GRANT. Properties of rutile (titanium dioxide). *Rev. Mod. Phys.*, 31:646–674, Jul 1959.

[8] K.S. Yeung and Y.W. Lam. A simple chemical vapour deposition method for depositing thin tio2 films. *Thin Solid Films*, 109(2):169 – 178, 1983.

[9] Sarah R. Kurtz and Roy G. Gordon. Chemical vapor deposition of doped tio2 thin films. *Thin Solid Films*, 147(2):167 – 176, 1987.

[10] Andrew Mills and Stephen Le Hunte. An overview of semiconductor photocatalysis. *Journal of Photochemistry and Photobiology A: Chemistry*, 108(1):1 – 35, 1997.

[11] Vanira Trifiletti, Riccardo Ruffo, Christian Turrini, Dario Tassetti, Rosaria Brescia, Fabio Di Fonzo, Claudia Riccardi, and Alessandro Abbotto. Dye-sensitized solar cells containing plasma jet deposited hierarchically nanostructured TiO2 thin photoanodes. *Journal of Materials Chemistry A*, 1(38):11665, 2013.

[12] Hari Singh Nalwa. Preface. In Hari Singh Nalwa, editor, *Handbook of Thin Films*, pages vii – ix. Academic Press, Burlington, 2002.

[13] M. Ohring. *Materials Science of Thin Films*. Elsevier Science, 2001.

[14] Michael Gratzel. Sol-gel processed tio2 films for photovoltaic applications. *Journal of Sol-Gel Science and Technology*, 22(1-2):7–13, 2001.

[15] M. Langlet, S. Permpoon, D. Riassetto, G. Berthomé, E. Pernot, and J.C. Joud. Photocatalytic activity and photo-induced superhydrophilicity of sol–gel derived tio2 films. *Journal of Photochemistry and Photobiology A: Chemistry*, 181(2–3):203 – 214, 2006.

[16] J. Aguado-Serrano and M.L. Rojas-Cervantes. Titania aerogels: Influence of synthesis parameters on textural, crystalline, and surface acid properties. *Microporous and Mesoporous Materials*, 88(1-3):205 – 213, 2006.

[17] Jiaguo Yu, Wen Liu, and Huogen Yu. A one-pot approach to hierarchically nanoporous titania hollow microspheres with high photocatalytic activity. *Crystal Growth & Design*, 8(3):930–934, 2008.

[18] JG Yu, YR Su, and Bei Cheng. Template-free fabrication and enhanced photocatalytic activity of hierarchical macro-/mesoporous titania. *Advanced Functional Materials*, 17(12):1984–1990, 2007.

[19] † Huogen Yu, † Jiaguo Yu, *, † Shengwei Liu, , and ‡ Stephen Mann*. Template-free hydrothermal synthesis of cuo/cu2o composite hollow microspheres. *Chemistry of Materials*, 19(17):4327–4334, 2007.

[20] Fang Lu, Weiping Cai, and Yugang Zhang. Zno hierarchical micro/nanoarchitectures: solvothermal synthesis and structurally enhanced photocatalytic performance. *Advanced Functional Materials*, 18(7):1047–1056, 2008.

[21] Sebastian M Waita, Bernard O Aduda, Julius M Mwabora, Claes G Granqvist, Sten-Eric Lindquist, Gunnar A Niklasson, Anders Hagfeldt, and Gerrit Boschloo. Electron transport and recombination in dye sensitized solar cells fabricated from obliquely sputter deposited and thermally annealed tio 2 films. *Journal of Electroanalytical Chemistry*, 605(2):151–156, 2007.

[22] Sang-Chul Jung, Byung-Hoon Kim, Sun-Jae Kim, Nobuyuki Imaishi, and Yong-Ick Cho. Characterization of a tio 2 photocatalyst film deposited by cvd and its photocatalytic activity. *Chemical Vapor Deposition*, 11(3):137–141, 2005.

[23] J Rodriguez, M Gomez, J Lu, Eva Olsson, and C-G Granqvist. Reactively sputter-deposited titanium oxide coatings with parallel penniform microstructure. *Advanced Materials*, 12(5):341–343, 2000.

[24] Motofumi Suzuki, Tadayoshi Ito, and Yasunori Taga. Photocatalysis of sculptured thin films of tio2. *Applied Physics Letters*, 78(25):3968–3970, 2001.

[25] Jia Long Yang, Sung Jin An, Won Il Park, G-C Yi, and Wonyong Choi. Photocatalysis using zno thin films and nanoneedles grown by metal–organic chemical vapor deposition. *Advanced materials*, 16(18):1661–1664, 2004.

[26] Albert Goossens, Edward-Louis Maloney, and Joop Schoonman. Gas-phase synthesis of nanostructured anatase tio2. *Chemical Vapor Deposition*, 4(3):109–114, 1998.

[27] P Milani, P Piseri, E Barborini, A Podesta, and C Lenardi. Cluster beam synthesis of nanostructured thin films. *Journal of Vacuum Science & Technology A: Vacuum, Surfaces, and Films*, 19(4):2025, 2001.

[28] Flavio Della Foglia, Tonia Losco, Paolo Piseri, Paolo Milani, and Elena Selli. Photocatalytic activity of nanostructured tio2 films produced by supersonic cluster beam deposition. *Journal of nanoparticle research*, 11(6):1339–1348, 2009.

[29] F Di Fonzo, CS Casari, V Russo, MF Brunella, A Li Bassi, and CE Bottani. Hierarchically organized nanostructured tio2 for photocatalysis applications. *Nanotechnology*, 20(1):015604, 2009.

[30] F Di Fonzo, A Bailini, V Russo, A Baserga, D Cattaneo, MG Beghi, PM Ossi, CS Casari, A Li Bassi, and CE Bottani. Synthesis and characterization of

tungsten and tungsten oxide nanostructured films. *Catalysis Today*, 116(1):69–73, 2006.

[31] L Mangolini, E Thimsen, and U Kortshagen. High-yield plasma synthesis of luminescent silicon nanocrystals. *Nano letters*, 5(4):655–659, 2005.

[32] C Riccardi, R Barni, F. de Colle, and M Fontanesi. Modeling and diagnostic of an SF/sub 6/ RF plasma at low pressure. *IEEE Transactions on Plasma Science*, 28(1):278–287, 2000.

[33] C. Riccardi, R. Barni, E. Sindoni, M. Fontanesi, and P. Tosi. Gaseous precursors of diamond-like carbon films: chemical composition of CH4/Ar plasmas. *Vacuum*, 61(2-4):211–215, May 2001.

[34] P J Chantry. A simple formula for diffusion calculations involving wall reflection and low density. *Journal of Applied Physics*, 62(4):1141, 1987.

[35] R B Piejak, V A Godyak, and B M Alexandrovich. A simple analysis of an inductive RF discharge. *Plasma Sources Science and Technology*, 1(3):179–186, August 1992.

[36] U R Kortshagen, U V Bhandarkar, M T Swihart, and Steven L. Girshick. Generation and growth of nanoparticles in low-pressure plasmas. *Pure and Applied Chemistry*, 71(10):1871–1877, January 1999.

[37] U Kortshagen and M Zethoff. Ion energy distribution functions in a planar inductively coupled RF discharge. *Plasma Sources Science and Technology*, 4(4):541–550, November 1995.

[38] F Croccolo, R Barni, S Zanini, A Palvarini, and C Riccardi. Material surface modifications with an inductive plasma. *Journal of Physics: Conference Series*, 100(6):062023, 2008.

[39] H. Nizard, M.L. Kosinova, N.I. Fainer, Yu. M. Rumyantsev, B.M. Ayupov, and Yu. V. Shubin. Deposition of titanium dioxide from {TTIP} by plasma enhanced and remote plasma enhanced chemical vapor deposition. *Surface and Coatings Technology*, 202(17):4076 – 4085, 2008.

[40] S Caldirola, H E Roman, and C Riccardi. Ion energy distribution functions in a supersonic plasma jet. *Journal of Physics: Conference Series*, 550:012043, November 2014.

[41] S Caldirola, R Barni, and C Riccardi. Characterization of a low pressure supersonic plasma jet. *Journal of Physics: Conference Series*, 550:012042, November 2014.

[42] Stefano Caldirola, Ruggero Barni, H Eduardo Roman, and Claudia Riccardi. Mass spectrometry measurements of a low pressure expanding plasma jet. *Journal of Vacuum Science & Technology A: Vacuum, Surfaces, and Films*, 33(6):061306, November 2015.

[43] M. R. Alexander, F. R. Jones, and R. D. Short. Mass Spectral Investigation of the Radio-Frequency Plasma Deposition of Hexamethyldisiloxane. *The Journal of Physical Chemistry B*, 101(18):3614–3619, May 1997.

[44] J Benedikt, A Hecimovic, D Ellerweg, and A von Keudell. Quadrupole mass spectrometry of reactive plasmas. *Journal of Physics D: Applied Physics*, 45(40):403001, October 2012.

[45] D. O'Connell, R Zorat, A R Ellingboe, and M M Turner. Comparison of measurements and particle-in-cell simulations of ion energy distribution functions in a capacitively coupled radio-frequency discharge. *Physics of Plasmas*, 14(10):103510, 2007.

[46] E.a.G. Hamers, W.G.J.H.M. van Sark, J. Bezemer, W.J. Goedheer, and W.F. van der Weg. On the transmission function of an ion-energy and mass spectrometer. *International Journal of Mass Spectrometry and Ion Processes*, 173(1-2):91–98, January 1998.

[47] R Barni, P Esena, and C Riccardi. Chemical kinetics simulation for atmospheric pressure air plasmas in a streamer regime. *Journal of Applied Physics*, 97(7):073301, 2005.

[48] R. Barni, S. Zanini, and C. Riccardi. Diagnostics of reactive RF plasmas. *Vacuum*, 82(2):217–219, October 2007.

[49] B M Annaratone, M W Allen, and J E Allen. Ion currents to cylindrical Langmuir probes in RF plasmas. *Journal of Physics D: Applied Physics*, 25(3):417–424, mar 1992.

[50] Francis F Chen. Low Temperature Plasma Technology Laboratory. 2000.

[51] Francis F Chen. Langmuir probes in RF plasma: surprising validity of OML theory. *Plasma Sources Science and Technology*, 18(3):035012, aug 2009.

[52] H. Timko, P. S. Crozier, M. M. Hopkins, K. Matyash, and R. Schneider. Why Perform Code-to-Code Comparisons: A Vacuum Arc Discharge Simulation Case Study. *Contributions to Plasma Physics*, 52(4):295–308, may 2012.

[53] Francis F. Chen, John D. Evans, and Donald Arnush. A floating potential method for measuring ion density. *Physics of Plasmas*, 9(4):1449, 2002.

[54] V A Godyak, R B Piejak, and B M Alexandrovich. Measurement of electron energy distribution in low-pressure rf discharges. *Plasma Sources Science and Technology*, 1(1):36, 1992.

[55] Isaac D Sudit and Francis F Chen. Rf compensated probes for high-density discharges. *Plasma Sources Science and Technology*, 3(2):162, 1994.

[56] C Riccardi, R Barni, and M Fontanesi. Experimental study and simulations of electronegative discharges at low pressure. *Journal of Applied Physics*, 90(8):3735–3742, 2001.

[57] J B Anderson and J B Fenn. Velocity Distributions in Molecular Beams from Nozzle Sources. *Physics of Fluids*, 8(5):780, 1965.

[58] Arthur Kantrowitz and Jerry Grey. A High Intensity Source for the Molecular Beam. Part I. Theoretical. *Review of Scientific Instruments*, 22(5):328, 1951.

[59] J Deckers and J B Fenn. High Intensity Molecular Beam Apparatus. *Review of Scientific Instruments*, 34(1):96, 1963.

[60] R. Campargue. Progress in overexpanded supersonic jets and skimmed molecular beams in free-jet zones of silence. *The Journal of Physical Chemistry*, 88(20):4466–4474, September 1984.

[61] J. Fernandez de la Mora. Surface impact of seeded jets at relatively large background densities. *The Journal of Chemical Physics*, 82(7):3453, 1985.

[62] Paul C Engelking. Spectroscopy of jet-cooled ions and radicals. *Chemical Reviews*, 91(3):399–414, May 1991.

[63] P Piseri, T Mazza, G Bongiorno, C Lenardi, L Ravagnan, F Della Foglia, F Di-Fonzo, M Coreno, M DeSimone, KC Prince, et al. Core level spectroscopy of free titanium clusters in supersonic beams. *New Journal of Physics*, 8(8):136, 2006.

[64] Erwin W Becker, K Bier, W Bier, R Schütte, and D Seidel. Separation of the isotopes of uranium by the separation nozzle process. *Angewandte Chemie International Edition in English*, 6(6):507–518, 1967.

[65] E.W. Becker and K. Bier. Die erzeugung eines intensiven, teilweise monochromatisierten wasserstoff-molekularstrahles mit einer laval-duse. *Zeitschrift fur Naturforschung - Section A Journal of Physical Sciences*, 9(11):975–986, 1954. cited By 31.

[66] G. Sanna and G. Tomassetti. *Introduction to Molecular Beams Gas Dynamics*. Imperial College Press, 2005.

[67] John B. Fenn. Mass spectrometric implications of high-pressure ion sources. *International Journal of Mass Spectrometry*, 200(1-3):459–478, December 2000.

[68] Harry Ashkenas and Frederick S. Sherman. The Structure and Utilization of Supersonic Free Jets in Low Density Wind Tunnels. In *Rarefied Gas Dynamics - Volume 2. Proceedings of the Fourth International Symposium held at the Institute for Aerospace Studies, Toronto, 1964*, pages 84–105. Academic, 1966.

[69] A. L. ADDY. Effects of axisymmetric sonic nozzle geometry on Mach disk characteristics. *AIAA Journal*, 19(1):121–122, January 1981.

[70] Omid Abouali, Saeideh Saadabadi, and Homayoon Emdad. Numerical investigation of the flow field and cut-off characteristics of supersonic/hypersonic impactors. *Journal of Aerosol Science*, 42(2):65–77, February 2011.

[71] Irina A Graur, Alexey Ph Polikarpov, and Felix Sharipov. Numerical modelling of rarefied gas flow through a slit at arbitrary pressure ratio based on the kinetic equation. *Zeitschrift für angewandte Mathematik und Physik*, 63(3):503–520, June 2011.

[72] David M. Lubman, Charles T. Rettner, and Richard N Zare. How isolated are molecules in a molecular beam? *The Journal of Physical Chemistry*, 86(7):1129–1135, April 1982.

[73] J. Fernandez de la Mora, S.V. Hering, N. Rao, and P.H. McMurry. Hypersonic impaction of ultrafine particles. *Journal of Aerosol Science*, 21(2):169–187, January 1990.

[74] Roger Campargue. Aerodynamic Separation Effect on Gas and Isotope Mixtures Induced by Invasion of the Free Jet Shock Wave Structure. *The Journal of Chemical Physics*, 52(4):1795, 1970.

[75] Victor H Reis and John B Fenn. Separation of Gas Mixtures in Supersonic Jets. *The Journal of Chemical Physics*, 39(12):3240, 1963.

[76] P. C. Waterman and S. Alexander Stern. Separation of Gas Mixtures in a Supersonic Jet. *The Journal of Chemical Physics*, 31(2):405, 1959.

[77] Eldon L Knuth. Composition distortion in MBMS sampling. *Combustion and Flame*, 103(3):171–180, November 1995.

[78] Michael a Lieberman and Allan J. Lichtenberg. *Principles of Plasma Discharges and Materials Processing*. John Wiley & Sons, Inc., Hoboken, NJ, USA, April 2005.

[79] Av V. Phelps. Cross Sections and Swarm Coefficients for Nitrogen Ions and Neutrals in N2 and Argon Ions and Neutrals in Ar for Energies from 0.1 eV to 10 keV. *Journal of Physical and Chemical Reference Data*, 20(3):557, 1991.

[80] M. C. M. van de Sanden, J. M. de Regt, and D. C. Schram. Recombination of argon in an expanding plasma jet. *Physical Review E*, 47(4):2792–2797, April 1993.

[81] Hyungjoo Shin, Weiye Zhu, Lin Xu, Vincent M Donnelly, and Demetre J Economou. Control of ion energy distributions using a pulsed plasma with synchronous bias on a boundary electrode. *Plasma Sources Science and Technology*, 20(5):055001, 2011.

[82] J B Lee, H Y Chang, and S H Seo. Collisional effect on the time evolution of ion energy distributions outside the sheath during the afterglow of pulsed inductively coupled plasmas. *Plasma Sources Science and Technology*, 22(6):065008, December 2013.

[83] M. C. M. van de Sanden, J. M. de Regt, and D. C. Schram. Recombination of argon in an expanding plasma jet. *Physical Review E*, 47(4):2792–2797, April 1993.

[84] Ruggero Barni, Stefano Zanini, and Claudia Riccardi. Characterization of the Chemical Kinetics in an O2/HMDSO RF Plasma for Material Processing. *Advances in Physical Chemistry*, 2012:1–6, 2012.

[85] K U Riemann. The Bohm criterion and sheath formation. *Journal of Physics D: Applied Physics*, 24(4):493–518, April 1991.

[86] N. Yu. Babaeva, J. K. Lee, J. W. Shon, and E. A. Hudson. Oxygen ion energy distribution: Role of ionization, resonant, and nonresonant charge-exchange collisions. *Journal of Vacuum Science & Technology A: Vacuum, Surfaces, and Films*, 23(4):699, 2005.

[87] Yongjing Lin, Guangbi Yuan, Rui Liu, Sa Zhou, Stafford W. Sheehan, and Dunwei Wang. Semiconductor nanostructure-based photoelectrochemical water splitting: A brief review. *Chemical Physics Letters*, 507(4–6):209 – 215, 2011.

[88] Tianyou Zhai, Xiaosheng Fang, Meiyong Liao, Xijin Xu, Haibo Zeng, Bando Yoshio, and Dmitri Golberg. A Comprehensive Review of One-Dimensional Metal-Oxide Nanostructure Photodetectors. *Sensors*, 9(8):6504–6529, August 2009.

[89] Kostya Ken Ostrikov, Uros Cvelbar, and Anthony B Murphy. Plasma nanoscience: setting directions, tackling grand challenges. *Journal of Physics D: Applied Physics*, 44(17):174001, May 2011.

[90] H. B. Profijt and W M M Kessels. Ion Bombardment during Plasma-Assisted Atomic Layer Deposition. *ECS Transactions*, 50(13):23–34, March 2013.

[91] D. M. Mattox. Particle bombardment effects on thin-film deposition: A review. *Journal of Vacuum Science & Technology A: Vacuum, Surfaces, and Films*, 7(3):1105, May 1989.

[92] I. Petrov, L. Hultman, U. Helmersson, J.-E. Sundgren, and J.E. Greene. Microstructure modification of TiN by ion bombardment during reactive sputter deposition. *Thin Solid Films*, 169(2):299–314, February 1989.

[93] Ruggero Barni, Stefano Zanini, and Claudia Riccardi. Characterization of the Chemical Kinetics in an O2/HMDSO RF Plasma for Material Processing. *Advances in Physical Chemistry*, 2012:1–6, 2012.

[94] Pierre-Alexandre Delattre, Trevor Lafleur, Erik Johnson, and Jean-Paul Booth. Radio-frequency capacitively coupled plasmas excited by tailored voltage waveforms: comparison of experiment and particle-in-cell simulations. *Journal of Physics D: Applied Physics*, 46(23):235201, June 2013.

[95] Michael D. Logue, Hyungjoo Shin, Weiye Zhu, Lin Xu, Vincent M. Donnelly, Demetre J. Economou, and Mark J. Kushner. Ion energy distributions in inductively coupled plasmas having a biased boundary electrode. *Plasma Sources Science and Technology*, 21(6):065009, December 2012.

[96] Hylton R. Murphy and David R. Miller. Effects of nozzle geometry on kinetics in free-jet expansions. *The Journal of Physical Chemistry*, 88(20):4474–4478, September 1984.

[97] O F Hagena and W. Obert. Cluster Formation in Expanding Supersonic Jets: Effect of Pressure, Temperature, Nozzle Size, and Test Gas. *The Journal of Chemical Physics*, 56(5):1793, 1972.

[98] Chong Huang, William T. Nichols, Daniel T. O'Brien, Michael F. Becker, Desiderio Kovar, and John W. Keto. Supersonic jet deposition of silver nanoparticle aerosols: Correlations of impact conditions and film morphologies. *Journal of Applied Physics*, 101(6):064902, 2007.

[99] H H Michels, R H Hobbs, and L a Wright. Electronic structure of the noble gas dimer ions. I. Potential energy curves and spectroscopic constants. *The Journal of Chemical Physics*, 69(11):5151, 1978.

[100] J.M. Soler, J.J. Saenz, N. García, and O. Echt. The effect of ionization on magic numbers of rare-gas clusters. *Chemical Physics Letters*, 109(1):71–75, 1984.

[101] S. a. Maiorov. Ion drift in a gas in an external electric field. *Plasma Physics Reports*, 35(9):802–812, September 2009.

[102] W. L. T. Chen, J. Heberlein, and E. Pfender. Critical analysis of viscosity data of thermal argon plasmas at atmospheric pressure. *Plasma Chemistry and Plasma Processing*, 16(4):635–650, December 1996.

[103] John a White. Lennard-Jones as a model for argon and test of extended renormalization group calculations. *The Journal of Chemical Physics*, 111(20):9352, 1999.

[104] B. H. Bransden and M. R. C. McDowell. *Charge Exchange and the Theory of Ion-atom Collisions*. Clarendon Press, 1992.

[105] Donald Rapp and W. E. Francis. Charge Exchange between Gaseous Ions and Atoms. *The Journal of Chemical Physics*, 37(11):2631, 1962.

[106] Rainer Hippler, Jana Kredl, and Vasile Vartolomei. Ion energy distribution of an inductively coupled radiofrequency discharge in argon and oxygen. *Vacuum*, 83(4):732–737, November 2008.

[107] E Kawamura, V Vahedi, M a Lieberman, and C K Birdsall. Ion energy distributions in rf sheaths; review, analysis and simulation. *Plasma Sources Science and Technology*, 8(3):R45–R64, August 1999.

[108] Scott D. Tanner. Plasma temperature from ion kinetic energies and implications for the source of diatomic oxide ions in inductively coupled plasma mass spectrometry. *Journal of Analytical Atomic Spectrometry*, 8(6):891, 1993.

[109] J. K. Olthoff, R. J. Van Brunt, and S. B. Radovanov. Effect of electrode material on measured ion energy distributions in radio-frequency discharges. *Applied Physics Letters*, 67(4):473, 1995.

[110] M Fivaz, S Brunner, W Schwarzenbach, a a Howling, and C Hollenstein. Reconstruction of the time-averaged sheath potential profile in an argon radiofrequency plasma using the ion energy distribution. *Plasma Sources Science and Technology*, 4(3):373–378, August 1995.

[111] D Barton, J W Bradley, D a Steele, and R D Short. Investigating Radio Frequency Plasmas Used for the Modification of Polymer Surfaces. *The Journal of Physical Chemistry B*, 103(21):4423–4430, May 1999.

[112] T Chevolleau and W Fukarek. Ion flux, ion energy distribution and neutral density in an inductively coupled argon discharge. *Plasma Sources Science and Technology*, 9(4):568–573, November 2000.

[113] Kostya (Ken) Ostrikov, Uros Cvelbar, and Anthony B Murphy. Plasma nanoscience: setting directions, tackling grand challenges. *Journal of Physics D: Applied Physics*, 44(17):174001, 2011.

[114] M Meyyappan. Plasma nanotechnology: past, present and future. *Journal of Physics D: Applied Physics*, 44(17):174002, 2011.

[115] Kostya (Ken) Ostrikov. Control of energy and matter at nanoscales: challenges and opportunities for plasma nanoscience in a sustainability age. *Journal of Physics D: Applied Physics*, 44(17):174003, 2011.

[116] R Hatakeyama, T Kaneko, T Kato, and Y F Li. Plasma-synthesized single-walled carbon nanotubes and their applications. *Journal of Physics D: Applied Physics*, 44(17):174004, 2011.

[117] O Hagena and W Henkes. Untersuchung der thermischen relaxation bei düsenströmungen durch analyse der gaskinetischen geschwindigkeitsverteilung. *Zeitschrift für Naturforschung A*, 15(10):851–858, 1960.

[118] N Abuaf, JB Anderson, RP Andres, JB Fenn, and DGH Marsden. Molecular beams with energies above one electron volt. *Science*, 155(3765):997–999, 1967.

[119] Susan DePaul, David Pullman, and Bretislav Friedrich. A pocket model of seeded supersonic beams. *The Journal of Physical Chemistry*, 97(10):2167–2171, 1993.

[120] James B Anderson. Separation of gas mixtures in free jets. *AIChE Journal*, 13(6):1188–1192, 1967.

[121] Frederick S Sherman. Hydrodynamical theory of diffusive separation of mixtures in a free jet. *Physics of Fluids (1958-1988)*, 8(5):773–779, 1965.

[122] Dietmar E Rothe. Electron beam studies of the diffusive separation of helium-argon mixtures. *Physics of Fluids (1958-1988)*, 9(9):1643–1658, 1966.

[123] Paolo Milani and Salvatore Iannotta. *Cluster beam synthesis of nanostructured materials*. Springer Science & Business Media, 2012.

[124] Otto F Hagena. Scaling laws for condensation in nozzle flows. *Physics of Fluids (1958-1988)*, 17(5):894–896, 1974.

[125] Otto F Hagena. Nucleation and growth of clusters in expanding nozzle flows. *Surface Science*, 106(1):101–116, 1981.

[126] Rolf Weiel. Clustering in expanding nozzle flows. *Zeitschrift für Physik D Atoms, Molecules and Clusters*, 27(1):89–92, 1993.

[127] Y. Ohama and D. Van Gemert. *Application of Titanium Dioxide Photocatalysis to Construction Materials: State-of-the-Art Report of the RILEM Technical Committee 194-TDP*. RILEM State-of-the-Art Reports. Springer Netherlands, 2011.

[128] Brian O'Regan and Michael Gratzel. A low-cost, high-efficiency solar cell based on dye-sensitized colloidal tio2 films. *Nature*, 353(6346):737–740, 10 1991.

[129] Ziqi Sun, Jung Ho Kim, Yue Zhao, Fargol Bijarbooneh, Victor Malgras, and Shi Xue Dou. Improved photovoltaic performance of dye-sensitized solar cells with modified self-assembling highly ordered mesoporous tio2 photoanodes. *J. Mater. Chem.*, 22:11711–11719, 2012.

[130] Bin Liu and Eray S. Aydil. Growth of oriented single-crystalline rutile tio2 nanorods on transparent conducting substrates for dye-sensitized solar cells. *Journal of the American Chemical Society*, 131(11):3985–3990, 2009. PMID: 19245201.

[131] Irene Gonzalez-Valls and Monica Lira-Cantu. Vertically-aligned nanostructures of zno for excitonic solar cells: a review. *Energy & Environmental Science*, 2(1):19–34, 2009.

[132] Fang Shao, Jing Sun, Lian Gao, Songwang Yang, and Jianqiang Luo. Forest-like tio2 hierarchical structures for efficient dye-sensitized solar cells. *J. Mater. Chem.*, 22:6824–6830, 2012.

[133] Jin-Yun Liao, Bing-Xin Lei, Dai-Bin Kuang, and Cheng-Yong Su. Tri-functional hierarchical TiO2 spheres consisting of anatase nanorods and nanoparticles for high efficiency dye-sensitized solar cells. *Energy & Environmental Science*, 4(10):4079, 2011.

[134] Wu-Qiang Wu, Bing-Xin Lei, Hua-Shang Rao, Yang-Fan Xu, Yu-Fen Wang, Cheng-Yong Su, and Dai-Bin Kuang. Hydrothermal fabrication of hierarchically anatase tio2 nanowire arrays on fto glass for dye-sensitized solar cells. *Scientific reports*, 3, 2013.

[135] Elham Ghadiri, Nima Taghavinia, Shaik M Zakeeruddin, Michael Gratzel, and Jacques-E Moser. Enhanced electron collection efficiency in dye-sensitized solar cells based on nanostructured tio2 hollow fibers. *Nano letters*, 10(5):1632–1638, 2010.

[136] Jin-Yun Liao, Jun-Wen He, Huiying Xu, Dai-Bin Kuang, and Cheng-Yong Su. Effect of tio 2 morphology on photovoltaic performance of dye-sensitized solar cells: nanoparticles, nanofibers, hierarchical spheres and ellipsoid spheres. *Journal of Materials Chemistry*, 22(16):7910–7918, 2012.

[137] Ramon Tena-Zaera, Jamil Elias, Claude Lévy-Clément, Chegnui Bekeny, Tobias Voss, Iván Mora-Seró, and Juan Bisquert. Influence of the potassium chloride concentration on the physical properties of electrodeposited zno nanowire arrays. *The Journal of Physical Chemistry C*, 112(42):16318–16323, 2008.

[138] Meidan Ye, Xukai Xin, Changjian Lin, and Zhiqun Lin. High efficiency dye-sensitized solar cells based on hierarchically structured nanotubes. *Nano letters*, 11(8):3214–3220, 2011.

[139] Dapeng Wu, Feng Zhu, Jianming Li, Hui Dong, Qi Li, Kai Jiang, and Dongsheng Xu. Monodisperse tio 2 hierarchical hollow spheres assembled by nanospindles for dye-sensitized solar cells. *Journal of Materials Chemistry*, 22(23):11665–11671, 2012.

[140] Jun-Ho Yum, Peter Chen, Michael Grätzel, and Mohammad K Nazeeruddin. Recent developments in solid-state dye-sensitized solar cells. *ChemSusChem*, 1(8-9):699–707, 2008.

[141] Ning Cai, Soo-Jin Moon, Le Cevey-Ha, Thomas Moehl, Robin Humphry-Baker, Peng Wang, Shaik M Zakeeruddin, and Michael Gratzel. An organic d-$\pi$-a dye for record efficiency solid-state sensitized heterojunction solar cells. *Nano letters*, 11(4):1452–1456, 2011.

[142] Hong-Yan Chen, Dai-Bin Kuang, and Cheng-Yong Su. Hierarchically micro/nanostructured photoanode materials for dye-sensitized solar cells. *Journal of Materials Chemistry*, 22(31):15475–15489, 2012.

[143] Yong Joo Kim, Mi Hyeon Lee, Hark Jin Kim, Gooil Lim, Young Sik Choi, Nam-Gyu Park, Kyungkon Kim, and Wan In Lee. Formation of highly efficient dye-sensitized solar cells by hierarchical pore generation with nanoporous tio2 spheres. *Advanced Materials*, 21(36):3668–3673, 2009.

[144] John A Thornton. The microstructure of sputter-deposited coatings. *Journal of Vacuum Science & Technology A*, 4(6):3059–3065, 1986.

[145] Thomas A Witten and Leonard M Sander. Diffusion-limited aggregation. *Physical Review B*, 27(9):5686, 1983.

[146] Jens Feder. Random sequential adsorption. *Journal of Theoretical Biology*, 87(2):237–254, 1980.

[147] Marjorie J Vold. Computer simulation of floc formation in a colloidal suspension. *Journal of Colloid Science*, 18(7):684–695, 1963.

[148] David N Sutherland. A theoretical model of floc structure. *Journal of Colloid and Interface Science*, 25(3):373–380, 1967.

[149] Paul Meakin. The growth of rough surfaces and interfaces. *Physics Reports*, 235:189 – 289, 1993.

[150] Anthony Robledo, Christopher N Grabill, Stephen M Kuebler, Aniruddha Dutta, Helge Heinrich, and Aniket Bhattacharya. Morphologies from slippery ballistic deposition model: A bottom-up approach for nanofabrication. *Physical Review E*, 83(5):051604, 2011.